Medizinische Fakultät
der
Universität Duisburg-Essen

Aus der Klinik für Partikeltherapie

Monte Carlo estimation of absorbed dose distributions in water and anthropomorphic phantoms obtained from homogeneous and heterogenous ^{106}Ru eye plaques

Inaugural-Dissertation
zur
Erlangung des Doktorgrades
der Naturwissenschaften in der Medizin
(Dr. rer. medic.)
durch die Medizinische Fakultät
der Universität Duisburg-Essen

Vorgelegt von
Francisco José Zaragoza Serrano
aus Badalona (Spanien)
2021

DOI: 10.17185/duepublico/74509
URN: urn:nbn:de:hbz:464-20210826-092938-8

Dekan: Herr Univ.-Prof. Dr. med. J. Buer
1. Gutachter: Herr Prof. Dr. L. Brualla y Barberà
2. Gutachter: Herr Univ.-Prof. Dr. med. D. Lohmann
3. Gutachter: Herr Priv.-Doz. Dr. rer. nat. L. Lüdemann
4. Gutachter: Herr Univ.-Prof. Dr. DI Dietmar Georg

Tag der mündlichen Prüfung: 22. April 2021

Publications

Publications in scientific journals related to this thesis:

- Brualla, L., **Zaragoza, F. J.**, Sempau, J., Wittig, A., and Sauerwein, W. (2012): Electron irradiation of conjunctival lymphoma—Monte Carlo simulation of the minute dose distribution and technique optimization. Int. J. Radiat. Oncol. Biol. Phys. 83, 1330-1337.

- Brualla, L., Sempau, J., **Zaragoza, F. J.**, Wittig, A., and Sauerwein, W. (2013): Accurate estimation of dose distributions inside an eye irradiated with ^{106}Ru plaques. Strahlenther. Onkol. 189, 68-73.

- Brualla, L., **Zaragoza, F. J.**, and Sauerwein, W. (2015): Monte Carlo simulation of the treatment of eye tumors with ^{106}Ru plaques: a study on maximum tumor height and eccentric placement. Ocul. Oncol. Pathol. 1, 2-12.

- **Zaragoza, F. J.**, Eichmann, M., Flühs, D., Sauerwein, W., and Brualla, L. (2017): Monte Carlo estimation of absorbed dose distributions obtained from heterogeneous ^{106}Ru plaques. Ocul. Oncol. Pathol. 3, 204-209.

- **Zaragoza, F. J.**, Eichmann, M., Flühs, D., Wittig, A., Sauerwein, W., and Brualla, L. (2019): Monte Carlo simulation of the treatment of uveal melanoma using measured heterogeneous ^{106}Ru plaques. Ocul. Oncol. Pathol. 5, 276-283.

- **Zaragoza, F. J.**, Eichmann, M., Flühs, D., Timmermann, B., and Brualla, L. (2020): Monte Carlo computation of dose-volume histograms in the structures at risk of an eye irradiated with heterogeneous ^{106}Ru plaques. In press. Ocul. Oncol. Pathol.

Presentations in scientific meetings related to this thesis:

- Brualla, L., **Zaragoza, F. J.**, Sempau, J., Wittig, A., and Sauerwein, W. (2010): Optimisation of the treatment technique used for the conjunctival lymphoma by means of Monte Carlo simulations and dose-volume histograms on high resolution CT images. Strahlenter. Onkol. Suppl 1, 186, 77.

- Brualla, L., **Zaragoza, F. J.**, Sempau, J., Flühs, D., Wittig, A., and Sauerwein, W. (2012): Innovative approach for the accurate absorbed dose at OARs and the dose distribution in the eye from ^{106}Ru plaques. Poster. Radiother. Oncol. Suppl 2, 103, S145-S146.

- Brualla, L., **Zaragoza, F. J.**, Sempau, J., Flühs, D., Lüdemann, L., Zimmermann, B., Wittig, A., and Sauerwein, W. (2012): Innovative Monte Carlo simulations for the accurate

estimation of absorbed dose at organs at risk and the dose distribution in the eye treated with ^{106}Ru plaques. Poster. Strahlenther. Onkol. 188, Suppl 1, 11-11.

- Sauerwein W., **Zaragoza, F. J.**, Eichmann, M., Flühs D., Brualla L. (2015): Absorbed dose distributions obtained from inhomogeneous ^{106}Ru eye plaques: discrepancies with the model used for treatment planning. Poster. Int. Soc. Ocul. Oncol. Paris.

- **Zaragoza, F. J.**, Eichmann, M., Flühs D., Sauerwein, W., and Brualla L. (2017): Monte Carlo estimation of absorbed dose distributions in an anthropomorphic phantom obtained from heterogeneous ^{106}Ru eye plaques. Oral presentation. Strahlenter. Onkol. 193, S11-S12.

Publications and posters during the thesis preparation, but not related to the thesis:

- Duch, M. A., **Zaragoza, F. J.**, Sempau, J., Ginjaume, M., Vaño, E., Sánchez, R., and Fernández, J. M. (2013): Simulación Monte Carlo de campos de radiación dispersa en radiología intervencionista. III Congreso conjunto SEFM-SEPR. Área 14-023 Poster.

Contents

Chapter 1

Introduction

1.1 Background

Uveal melanoma and retinoblastoma are the most common types of eye cancer affecting adults and children, respectively (Nathan et al., 2015). Brachytherapy using ^{106}Ru eye plaques for small and medium melanomas and retinoblastomas yields, in general, good results in terms of tumor control, local recurrences and preserving, to some extent, visual acuity (Brady and Hernández, 1992; Shields et al., 2001; Schueler et al., 2006; Mossböck et al., 2007; Takiar et al., 2014).

Nevertheless, the dose distribution produced by these plaques is still a challenge and further improvements are needed. In the past, the manufacturer of these plaques, Eckert & Ziegler BEBIG GmbH (Berlin, Germany), provided only the absorbed depth dose distribution along the symmetry axis given in the plaque certificate (Kaulich et al., 2004). Although this is the most important dosimetrical information, it is insufficient for an accurate calculation of the dose distribution. Owing to the manufacturing procedure of these plaques, the distribution of the emitter substance is not homogeneous and hot spots might be present in some of them. The heterogeneities in a given plaque will affect the dose distribution subsequently deposited in the eye. Currently, the manufacturer provides a sparse map of the emitter substance that improves the situation respect to the past but it is still insufficient for accurate dose calculations.

This thesis aims at improving the current knowledge on the effects produced on the dose distributions by the aforementioned emitter heterogeneities. Monte Carlo simulations of radiation transport are used to perform this study. First, the dose distribution tallied in water produced by two actual eye plaques, named CCA1364 and CCB1256, for which there is a measured emitter distribution, is simulated. A comparison is performed between the dose distributions in water produced by generic plaque models, CCA and CCB, which consider the radioactive substance homogeneously distributed on its surface, and the actual plaques. Secondly, using a computerized axial tomography of an anonymized patient as a voxelized anthropomorphic phantom, the absorbed dose distributions in the eye are computed. These dose distributions are also obtained from simulations of different placements of the plaques and for different rotations around the symmetry axis of the actual heterogeneous plaques. Finally, uveal tumors are modeled. The absorbed doses in the tumoral volumes are computed.

The results are compared to determine the most effective treatment while minimizing the absorbed dose to the structures at risk as recommended by European and many national laws (Council of the European Union, 2013).

1.2 Objectives

The aim of this thesis is to improve the knowledge on the dosimetry of ^{106}Ru eye plaques and their application to ocular tumors, by means of the general-purpose Monte Carlo radiation transport code PENELOPE. The following partial objectives are defined in order to accomplish this goal:

1. To compute the absorbed dose distributions in a water phantom for the generic CCA and CCB eye plaque models using a source defined as a spherical cap. To compare computed depth dose distributions against experimental data published by other researchers and by the manufacturer.

2. To determine the influence of the measured emitter distribution of two actual plaques on the absorbed dose distribution in a water phantom. To compare simulated depth doses against the experimental data published by other researchers and by the manufacturer. To compare simulated lateral profiles of the generic and actual eye plaques.

3. To compute absorbed dose distributions inside a voxelized anthropomorphic phantom of the eye produced by the generic CCA and CCB plaques and their actual counterparts. To determine the influence of the distribution of the emitter map in the computed absorbed dose.

4. To simulate uveal melanoma treatments of modeled tumors inside an anthropomorphic phantom using the generic CCA and CCB eye plaques and their actual counterparts. To determine the influence of the distribution of the emitter map of the plaques on the structures at risk.

1.3 Ocular tumors

The eye is a quasi-spherical organ that consists of three main layers, three compartments and three fluids (Galloway et al. (2006)). The outer layer is formed by the sclera, the cornea and the lamina cribrosa. The cornea is transparent and allows the light to enter into the eye while the sclera is white and opaque. The middle layer or uvea is mainly a vascular layer and it is formed by the iris, the pupil, the ciliary body and the choroids. The iris, which is a circular disk perforated centrally by the pupil, conforms the anterior part of the uvea. The ciliary body is the intermediate part of the uvea while the choroids is its posterior part. The inner layer or neurosensory layer is formed by the pigment epithelium of the retina, the retinal photoreceptors and the retinal neurons. The space between the cornea and the iris corresponds to

the anterior chamber and contains the aqueous humor, which is a solution of water and electrolytes with a low protein content. The vitreous chamber corresponds to the space between the lens, the ciliary body and the retina. This chamber contains the vitreous humor, which is a transparent gel made of collagen fibres, hyaluronic acid and water. The posterior chamber is the smallest and also contains the aqueous humor and is located between the iris, the anterior part of the lens and the ciliary body. Finally, the last fluid corresponds to the blood whose function is to maintain intraocular pressure and is found mainly in the choroid. The anatomy of a human eye is shown in figure 1.1.

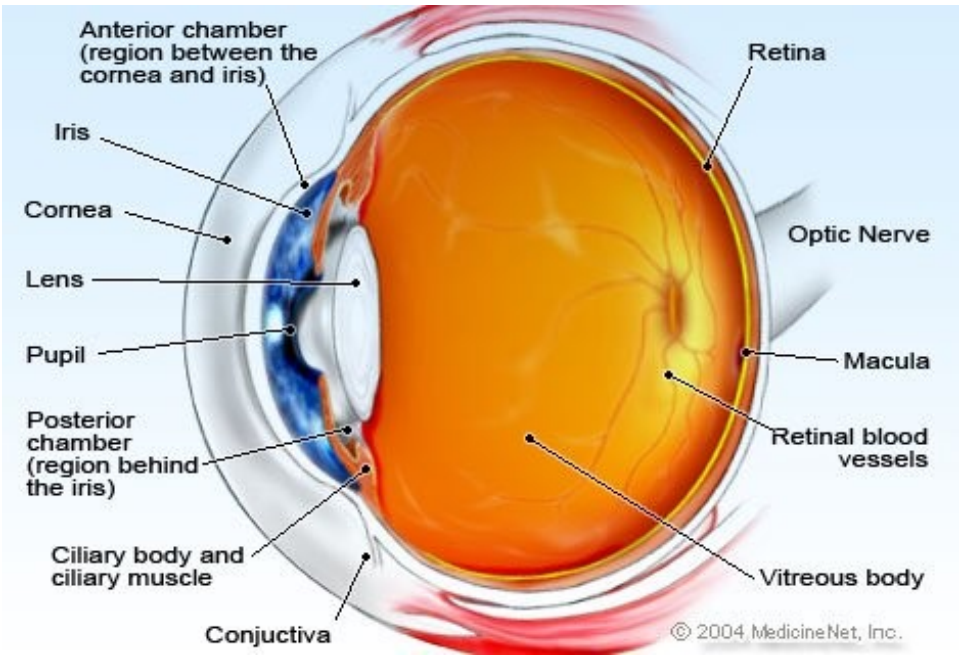

FIGURE 1.1: Anatomy of a human eye. Image published at MedicineNet ©2016, WebMD, LLC. All rights reserved. Reproduced with permission.

Ocular tumours can appear on the eyelids, in the eye (conjunctiva, choroid or retina) and in the orbit (the cavity that houses the eyeball). Apart from the choroidal hemangioma, which is a benign tumour with no risk of metastasis, the most frequent malignant intraocular tumors are uveal melanoma and retinoblastoma. Of the diagnosed intraocular tumors, 75% correspond to uveal melanomas, 20% to retinoblastomas and the remaining 5% to other residual type of tumors.

Uveal melanoma originates in melanocytes, with the most frequent location being the choroids, accounting for 80% of all uveal melanomas, followed by ciliary body with 12% and iris with 8% of incidence (Damato, 2001). The estimated incidence is of 4 to 5 cases per million inhabitants per year in the United States (Singh et al., 2011) and of 5 to 7.4 cases in European studies (Virgili et al., 2007).

Retinoblastoma is a congenital malignancy that affects the retina and in rare cases also the pineal gland (trilateral retinoblastoma). It is the most frequent malignant intraocular tumor in

childhood, of which 30% are bilateral and 40% hereditary. It is the first diagnosis found to be result of a genetic defect of the 13q14 gene. Early diagnostic is crucial for therapeutic success. This ocular tumor is usually diagnosed between the first and third year of life and rarely after 5 years of age (Olch, 2013).

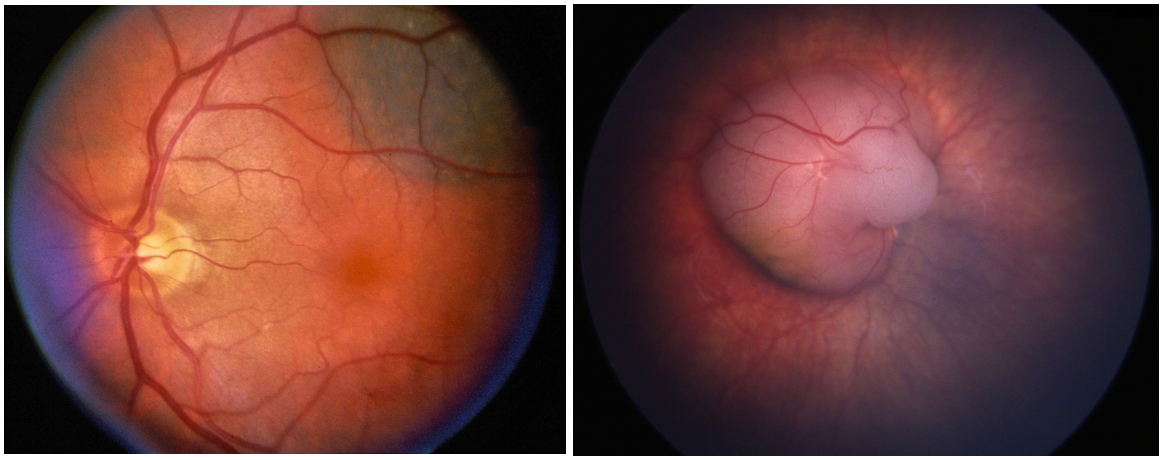

(A) Choroidal melanoma. (B) Retinoblastoma.

FIGURE 1.2: These images were originally published in the Retina Image Bank. Plot (A) corresponds to a choroidal melanoma of a 68-year-old white male. David Callanan, MD. Texas Retina Associates. April 11, 2014; 16419. Plot (B) corresponds to a fundus photograph of an 17-month-old female infant with retinoblastoma over the optic nerve. Giselle DeOliveira, University of Miami, Bascom Palmer Eye Institute. April 30, 2020; 53837. ©The American Society of Retina Specialists. Reproduced with permission.

There are different types of treatments for all these tumors, which can be applied individually or in combination, with the purpose of preventing metastatic spread and preserving useful vision while minimizing the risk of collateral damage to adjacent tissues. The type of treatment chosen depends on the type of tumor, its position, size, type of tissue, as well as the personal conditions of each patient. For uveal melanomas, treatments involving ionizing radiation are brachytherapy and external beam radiotherapy, usually with protons. Laser photocoagulation and transpupillary thermotherapy are other treatments recommended for small and shallow tumors. Other surgical treatments less aggressive than enucleation are endoresection and sclerouvectomy. Chemotherapy is only recommended as a palliative treatment when the metastatic disease occurs. With respect to retinoblastoma, apart from brachytherapy, teletherapy with photons or protons, focal therapies such as transpupillary thermotherapy, cryotherapy and laser photocoagulation, alone or in combination with chemotherapy, may be used.

1.4 Ocular brachytherapy

Surgical treatment with enucleation was the primary prescription applied for uveal melanoma disease for more than 100 years. Nowadays, brachytherapy is the most common form of radiotherapy for malignant intraocular tumors since it is less invasive than enucleation and the absorbed dose into adjacent tissues is lower than the absorbed dose when using external beam radiotherapy (Jager et al., 2011). The first successful treatment for uveal melanoma using brachytherapy was performed by Deutschmann in Hamburg in 1915 (Brewington et al., 2018). In 1929, Moore inserted a radon seed into a melanoma in the eye and, later, in 1948, Stallard studied the retinoblastoma treatment by inserting radon seeds into wax and placing it on the surface of the eye for a later removal (Brewington et al., 2018).

Over time, the following radioisotopes were used for brachytherapy treatments of uveal melanomas and retinoblastomas:

- Radon seeds were used in the late 1960s by Willian Havener at the Ohio State University. Later, in 1970 Davidorf published the first treatment of posterior uveal melanoma using radon gas seeds encapsulated in gold as a radiation source (Davidorf, 1970).
- ^{60}Co radioisotope was used as an evolution of Stallard's technique for the treatment of retinoblastoma (Stallard et al., 1966).
- ^{106}Ru is the most common radioisotope used in Europe. It produces β-radiation and was introduced by Peter Lommatzsch in the 1960s (Lommatzsch and Vollmar, 1966; Pe'er, 2012). It is easily shielded and has a limited depth of penetration.
- ^{125}I produces γ-radiation and is the most common radioisotope used in the United States. The use of this radioisotope is based on the results of the Collaborative Ocular Melanoma Study (COMS) (Hawkins, 2011).
- ^{103}Pd is a low-energy photon emitter also used in the US from 1989 (Taylor, 1989).

This thesis focuses on brachytherapy with ^{106}Ru plaques since it is one of the most effective treatments intended to preserve the globe and to maintain the visual acuity to some extent (Damato et al., 2005b; Simpson et al., 2014; Naseripour et al., 2016). Although there is a vast literature on the adequacy of ^{106}Ru plaques for the treatment of uveal melanomas (Pe'er, 2012) and references therein) most published works base their conclusions on retrospective clinical studies (Damato et al., 2005a; Verschueren et al., 2010). The lack of precise knowledge about the dose distribution in the tumor volume and surrounding structures at risk hinders the possibility to improve the clinical outcome (Astrahan, 2003; Nag et al., 2003; Jager et al., 2011).

1.5 The ^{106}Ru eye plaques

The ^{106}Ru eye plaques studied herein are manufactured by Eckert & Ziegler BEBIG GmbH (Berlin, Germany). All plaques consist of sealed radioactive sources whose encapsulating material is pure silver. Plaques are supplied with certificates and measurement records of the absorbed dose rate in water. The certificates corresponding to the calibration curve of the dose rate were supplied by the ASMW (Amt für Standardisierung, Messwesen und Warenprüfung, GDR) until year 2002 when the manufacturer updated them by certificates with a calibration based on the NIST (National Institute of Standards and Technology, USA) (Kaulich et al., 2004). Measurements with a 95% of confidence level are made with a plastic scintillation detector with a high spatial resolution. For the depth dose rate distribution, the certificate provides 11 measurement points along the symmetry axis of the plaques. The relative dose is given with respect to the nominal absorbed dose obtained at a reference point 2.0 mm from the surface. The certificate also includes 33 points around of the symmetry axis measured at a distance of 1.0 mm from the surface of the plaque that provide information on the heterogeneity of the emitter distribution. Notice that these points around the symmetry axis provided in the certificate are not used in this thesis.

Figure 1.3 shows the existing plaque models together with their therapeutical indication. Eye plaques are produced in various sizes and shapes. In case of a difficult tumour location or to protect relevant eye organs such as the macula, the optic nerve or the iris, special shapes with cut-outs are also produced. In this thesis only the CCA and CCB generic models are analyzed together with the actual CCA1364 and CCB1256 plaques. The CCB1256 eye plaque was measured on June 1, 2005 while the CCA1364 eye plaque was measured on September 21, 2012.

1.6 The ^{106}Ru/^{106}Rh beta decay spectrum

^{106}Ru/^{106}Rh isotopes are pure β^- emitters. For both emitters, the beta particles averaged over many disintegrations have a continuous emission spectrum whose shape can be explained through the Fermi theory of beta decay (see figure 1.4).

Both isotopes are in secular equilibrium (ICRU, 2004). ^{106}Ru is the parent isotope which decays via β^- disintegration to the ground state of ^{106}Rh with a half-life of 376.6 d and Q value of (39.4 ± 0.2) keV. ^{106}Rh is the daughter isotope which also decays via β^- disintegration to the ground state and excited levels of ^{106}Pd. This last disintegration is used for therapeutic purposes and it is characterized by a half-life of 29.8 s with a Q value of (3545.6 ± 5.3) keV. Figure 1.5 shows the β^- decay schemes of ^{106}Ru and ^{106}Rh. There are also contributions of a gamma spectrum and minor contributions resulting from Auger emission and electron capture processes due to the transition from excited levels to the ground level of ^{106}Pd that are not considered in this thesis (De Frenne and Negret, 2008). The gamma component of the dose becomes significant only for doses four orders of magnitude below the maximum dose,

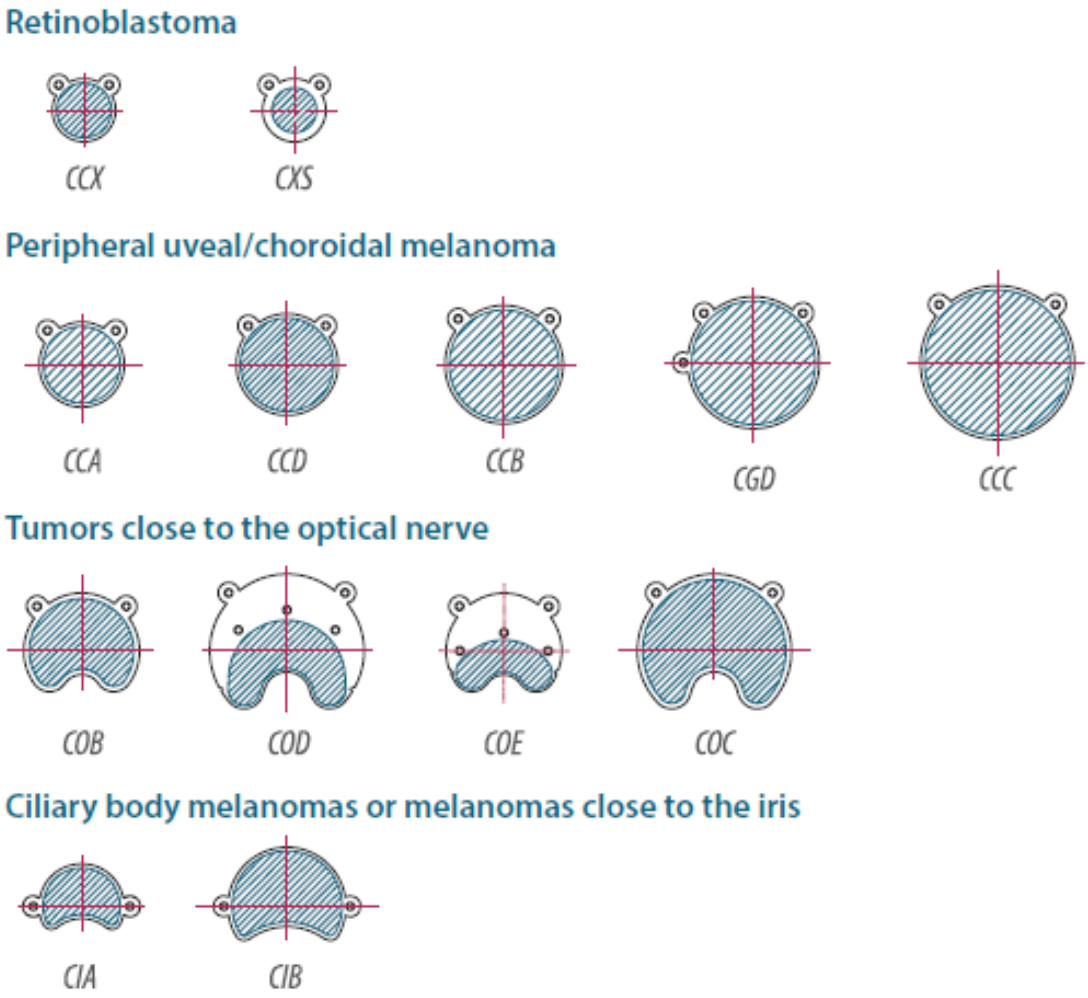

FIGURE 1.3: ^{106}Ru available eye plaque models and therapeutical recommendations. The hatched zone indicates the location of the emitter substance. Courtesy of Eckert & Ziegler BEBIG, GmbH (Berlin, Germany).

therefore, it is only relevant for radiological protection studies (Hermida-López and Brualla, 2017).

1.7 The Monte Carlo method for radiation transport

The Monte Carlo method is a wide set of mathematical algorithms based on numerical integration and the use of stochastic techniques to solve problems whose complexity prevents them to be analytically solved (Rubinstein and Kroese, 2016). The power of the method allows to achieve numerical results using random (actually pseudo-random) numbers and since its conception it has been applied to a wide range of disciplines such as physics, engineering or finance (Kalos and Whitlock, 2009).

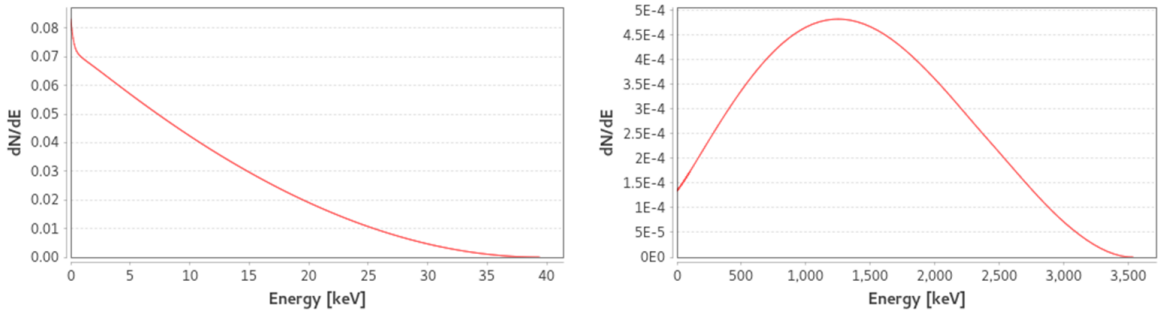

(A) ^{106}Ru beta spectrum.

(B) ^{106}Rh beta spectrum.

FIGURE 1.4: Beta spectra of ^{106}Ru and ^{106}Rh obtained from the International Atomic Energy Agency (IAEA) Live Chart of Nuclides (`https://www-nds.iaea.org/`). Reproduced with permission.

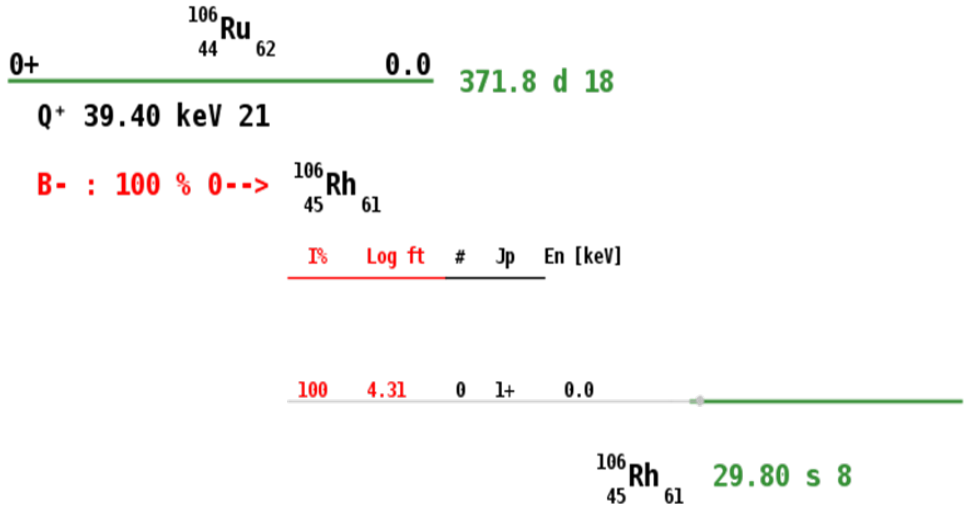

FIGURE 1.5: Decay schemes for ^{106}Ru/^{106}Rh pure β^- emitters in secular equilibrium. ^{106}Ru decays to the ground state of ^{106}Rh that decays to excited states and ground state of ^{106}Pd. Plots taken from the IAEA Live Chart of Nuclides (`https://www-nds.iaea.org/`), based on data from De Frenne and Negret (2008). Reproduced with permission.

The radiation transport term describes the physical process in which ionizing radiation interacts with matter. Initially, the study of radiation transport was limited to the analytical solution of the Boltzmann transport equation for simple geometries and semi-infinite media (Zheng-Ming and Brahme, 1993). The availability of computers and the use of Monte Carlo techniques allowed the numerical solution of the Boltzmann equation in more complex situations (Hayward and Hubbell, 1954).

Nowadays, the Monte Carlo computation of absorbed dose distributions in radiotherapy is widely accepted as the most accurate approach. This is particularly true in the presence of small radiation fields, like the ones involved in eye irradiation therapy. The Monte Carlo

method exactly solves the transport equation and, in principle, its accuracy is only limited by that of the employed interaction cross sections.

The Monte Carlo radiation transport method describes a process in which primary particles with an initial high energy interact with matter. In these interactions, primary particles might transfer part of their energy to the medium while producing secondary particles and changing their flight direction. The whole process occurs inside arbitrarily complex geometries made by materials of varied chemical composition. The simulation process consists of the following steps:

- A primary particle with a well defined initial state (type of particle, position, flight direction and kinetic energy) is positioned inside a geometry.
- The distance at which the next interaction will occur (a Poisson process) is determined by sampling the mean free path length probability density function which is characteristic for each particle, energy and material. The particle is moved to a new position along the straight line defined by the flight direction.
- The type of interaction is randomly selected by taking into account the probabilities given by the available interaction cross sections.
- The interaction is simulated and relevant quantities are tallied. State variables of the particle, including its energy, are updated. If secondary particles are created they are stored to be subsequently simulated.
- The process returns to the second step until the energy of the primary particle falls below a user-defined threshold or until it escapes the simulation geometry. The same process is repeated for all secondary particles and their descendants. Once the process finalizes a history has been simulated.

The simulation of a primary particle and its descendants is called a *history* or a *shower*. By simulating a large number of histories it is possible to determine the average of observables with an uncertainty arbitrarily small. Owing to the stochastic nature of the Monte Carlo method, all tallied quantities have an associated statistical uncertainty.

For the different quantities of interest, the estimated expected values are computed as the arithmetic mean of the tallied values from a number of N independently simulated histories as follows,

$$\overline{Q} = \frac{1}{N} \sum_{i=1}^{N} q_i, \tag{1.1}$$

where q_i is the contribution of the i-th history to the tallied quantity Q. For a large number of N simulated histories, this mean converges to the expected value of $\langle Q \rangle$ which is normally distributed with a standard deviation that can also be estimated by:

$$\sigma_Q = \sqrt{\frac{1}{N} \left[\frac{1}{N} \sum_{i=1}^{N} {q_i}^2 - \overline{Q}^2 \right]}. \tag{1.2}$$

Notice that for a large N the standard statistical uncertainty associated to the tallied expected value $\langle Q \rangle$, decreases approximately as $1/\sqrt{N}$.

For a certain number of primary particles N, the simulation time depends on the number of interactions that occur in the path of the particles. For high energy charged particles such as electrons used in radiotherapy, the number of interactions per unit of path length is high and the simulation becomes exceeding slow. This does not happen with photons since the number of interactions is relatively smaller. To manage with this feature, two different simulation schemes are considered. The *detailed simulation*, useful for particles with few interactions such as photons, in which all interactions are simulated in detail, and the so-called *condensed transport schemes*, useful for charged particles such as electrons, in which the effect of multiple interactions is artificially described in a single step (Fernández-Varea et al., 1993). The so-called *condensed transport schemes* use multiple-scattering theories to determine the probability distributions of the step length (Goudsmit and Saunderson, 1940; Landau, 1944; Lewis, 1950). Berger (1963) classifies the condensed transport algorithms into two types based on how the value of the step length is determined as follows:

- Class I algorithms: This type of algorithm considers a fixed path length. This approach presents problems when the length of the predefined path length is not contained in a single material. That is, when the path length crosses the boundary between two materials.

- Class II algorithms: In this case, the path length is calculated randomly. With this approach, when a particle arrives to an interface between contiguous media, it is stopped and the simulation is resumed with the interaction properties of the new medium. The interactions are defined as *soft* when the angular deviations and the loss of energy are below the user-defined cut-off values. The rest of the interactions are defined as *hard* and they are simulated in detail. Notice that the accuracy of the simulation could depend on the selected step length and, consequently, on the selected cut-off values that distinguish between *soft* and *hard* events.

1.8 The PENELOPE code

There exist several general-purpose Monte Carlo codes used for the simulation of radiation transport in material media, such as EGSnrc (Kawrakow and Rogers, 2003), FLUKA (Ferrari et al., 2005), Geant4 (Agostinelli et al., 2003; Allison et al., 2006), MCNP (X-5 Monte Carlo Team, 2005) and PENELOPE (Baró et al., 1995; Sempau et al., 1997; Salvat and Fernández-Varea, 2009; Salvat, 2019). These codes are intended for the simulation of radiation transport in a wide energy range and in arbitrarily complex geometries formed by materials composed by a wide range of atomic number species. They have been successfully applied in numerous fields including medical physics.

Simulations for this thesis were performed using the general-purpose Monte Carlo radiation transport code PENELOPE-2008 (Salvat and Fernández-Varea, 2009) which simulates the

coupled transport of electrons, photons and positrons in an energy range from 50 eV up to 1 GeV in materials with arbitrary chemical compositions. PENELOPE performs detailed transport for photons while for electrons and positrons the transport is performed using a mixed class II algorithm for the condensed scheme. If desired, detailed simulation of charged particles is also possible. The user-defined transport parameters that control the simulation are the following:

- C1 determines the average angular deflection between consecutive hard events and previous soft collisions.
- C2 limits the maximum average fractional energy loss between consecutive hard events.
- WCC corresponds to the cutoff energy value that separates hard from soft inelastic interactions.
- WCR corresponds to the cutoff energy value for Bremsstrahlung emission.
- DSMAX determines the maximum allowed step length for charged particles.
- EABS(e^-,γ,e^+) are the absorption energies at which the transport of the corresponding particle (electron, photon or positron) is terminated and the particle is assumed to be absorbed and its energy locally deposited.

These parameters determine the speed and accuracy of the simulation. To achieve a detailed transport of all particles in a given material, the values must be set to C1=C2=WCC=0 and WCR with a negative arbitrary value.

To model the geometry PENELOPE uses the package PENGEOM (Sempau, 1996) that allows to define bodies by grouping quadric surfaces.

PENELOPE is a set of subroutines that needs a main steering program. In this thesis the main program penEasy (version 2010-08-07) has been used (Sempau et al., 2011; Almansa et al., 2016). penEasy gives to PENELOPE the source of the particles, the quantities of interest to be tallied, the transport parameters and also the so-called variance-reduction techniques (Bielajew and Rogers, 1988) aimed at increasing the simulation efficiency. A distinctive feature of penEasy is that extends the geometrical capabilities of PENELOPE by means of the penVox package which allows the combined simulation of voxelized and quadric geometries (Sempau et al., 2011).

The PENELOPE code is open source and freely available from the Organisation for Economic Co-operation and Development (OECD) Nuclear Energy Agency (NEA) Data Bank (`http://www.nea.fr`) and, in North America, from the Oak Ridge National Laboratory (`http://rsicc.ornl.gov`). The penEasy code is also open source and freely available at the Institute of Energy Technologies (`http://inte.upc.edu`).

1.9 Thesis outline

The thesis is organized in seven chapters where the present chapter introduces the research framework. It also establishes the general objective to be achieved through the formulation of partial objectives. These partial objectives are developed in the subsequent chapters.

Chapter 2 presents the results of the absorbed dose distributions in water for the CCA and CCB generic plaques computed through Monte Carlo simulations using the PENELOPE code. To perform these simulations, the penEasy program is modified to allow the use of hemispherical emission sources representing the eye plaques and also to allow the simulation of beta decay spectra. For each plaque, depth dose and lateral profiles are computed. Depth doses are compared with experimental data provided by the manufacturer and also with previously published works. Isodose lines are computed. Most of the content of this chapter was published by the author of this thesis and coauthors in the journal *Strahlentherapie und Onkologie* (Brualla et al., 2013).

In chapter 3 actual plaques CCA1364 and CCB1256 are simulated using the emission map of the radioactive substance courtesy of Dr. rer. nat. M. Eichmann (*Fakultät Physik, Technische Universität Dortmund, Germany*) and published in her doctoral dissertation. A further modification is needed on penEasy to compute the absorbed dose in water using the normalized emission maps of the actual eye plaques as probability distributions. A comparison between the generic homogeneous approximation and the actual heterogeneous plaques is presented for the absorbed depth dose, the lateral profiles and the isodose lines. Results are also compared with the experimental data given by the manufacturer and the data published in other works. The contents of this chapter were published by the author of this thesis and coauthors in the journal *Ocular Oncology and Pathology* (Zaragoza et al., 2017).

Chapter 4 presents the computation of the absorbed dose inside an anthropomorphic phantom of a computerized tomography scan of an anonymized adult patient. Taking advantage of the feature of penEasy that allows the use of quadric geometries inserted in voxelized geometries, the quadric geometry of the eye plaques is embedded into the computerized tomography. The anatomical volumes corresponding to eye structures where the absorbed dose is computed are segmented. Simulations of the anterior, posterior and equatorial placement of the plaques are computed for the generic homogeneous CCA and CCB plaques and for the actual heterogeneous CCA1364 and CCB1256 eye plaques. For the CCB1256 eye plaque, three possible rotations are also simulated depending on the location of the hot spot present in this plaque. Results are given in terms of cumulative dose-volume histograms of each selected volume. The content of this chapter corresponding to the homogeneous distribution of the radioactive substance was published in the journal *Strahlentherapie und Onkologie* (Brualla et al., 2013). The code used for segmenting the anatomical structures in the computerized tomography was developed and first employed by the author in an article published in the *International Journal of Radiation Oncology, Biology, Physics* (Brualla et al., 2012a). The results related to the heterogeneous distribution are currently in press in the journal *Ocular Oncology and Pathology* (Zaragoza et al., 2020).

Chapter 5 presents the simulation of uveal melanoma treatments for tumors in anterior, posterior and equatorial locations. Volumes corresponding to modeled tumors are defined in the same geometry employed in the previous chapter. Simulations are performed for tumors in anterior, posterior and equatorial locations of both, the generic homogeneous CCA and CCB plaques and the actual heterogeneous CCA1364 and CCB1256 plaques. For equatorial tumors, only centric treatments, those in which the symmetry axes of the plaque and the tumor are aligned, are simulated. For posterior tumors only eccentric treatments are simulated while for anterior tumors eccentric treatments are simulated, too. For the anterior and posterior tumors, rotations of the CCA1364 and CCB1256 plaques around its symmetry axis are considered taking into account the distribution of their emitter substance. For each tumor, treatments are compared using cumulative dose-volume histograms. Most of the content of this chapter was published by the author of this thesis and coauthors in the journal *Ocular Oncology and Pathology* (Brualla et al., 2014; Zaragoza et al., 2018).

Chapter 6 presents a discussion where the scope and limitations of the results obtained are analyzed.

Finally, chapter 7 briefly summarizes the conclusions of the doctoral dissertation, and the major findings regarding the objectives outlined in chapter 1.

Chapter 2

Monte Carlo computation of absorbed dose distributions produced by homogeneous CCA and CCB eye plaques in a water phantom

2.1 Introduction

Measurements of absorbed dose distributions produced by beta-ray eye plaques can be done using thermoluminescence dosimeters (Soares et al., 2001; Kovačević et al., 2005; Krause et al., 2019), alanine pellets (Soares et al., 2001), plastic (Soares et al., 2001; Kaulich et al., 2004; Eichmann et al., 2012; Flühs et al., 2016) and liquid scintiallators (Kirov et al., 2005), extrapolation ionization chambers (Soares et al., 2001; Davelaar et al., 1992; Hansen et al., 2019), small fixed-volume ionization chambers (Soares et al., 2001), magnetic resonance imaging of BANG polymer gel (Chan et al., 2001), diode detectors (Soares et al., 2001), p-type silicon detector (Lax, 1991), diamond detectors (Soares et al., 2001) and radiochromic films (Taccini et al., 1997; Soares et al., 2001; Kirov et al., 2005; Hermida-López and Brualla, 2018; Trichter et al., 2018). Due to the curvature of the plaques, the small radiation field produced and the high dose gradient, measurements are difficult and prone to large uncertainties.

From a theoretical perspective, the absorbed dose distributions in water produced by eye plaques were initially calculated using a point-source numerical method (Loevinger, 1950; Vynckier and Wambersie, 1982; Hokkanen et al., 1997). The method mixes a finite size source of small dimensions with experimental results to obtain a point source equation, which by numerical integration over the plaque surface determines the dose distribution. A modification of the point-source method, called patch-source model (Astrahan, 2003) was developed to determine with better accuracy the dose distribution in water.

The Monte Carlo method yields more accurate dose distributions with respect to those computed with analytical methods (Reynaert et al., 2007), such as those mentioned above, particularly in the presence of small fields (Chetty et al., 2007; Fernández-Varea et al., 2007; Das et al., 2007). In a first attempt to use the Monte Carlo method for the computation of dose

distributions from ruthenium eye plaques, Davelaar et al. (1992) programmed a combined point-source and Monte Carlo algorithm to model the CCA and CCB plaques. The dose results obtained were on average 15% lower than the manufacturer's experimental data.

The first simulation using only a general-purpose Monte Carlo code for computing dose distributions in water obtained from eye plaques was done by Sánchez-Reyes et al. (1998). Unfortunately, some inconsistencies in the geometric description of the eye plaques were detected (Brualla et al., 2012a) compromising part of the results obtained.

Monte Carlo computations of beta-ray dose distributions in water from ophthalmic eye plaques using various codes were presented by Cross et al. (2001). The researchers studied a non-clinical planar plaque and a CCB eye plaque. Simulated results for the CCB eye plaque showed non-negligible differences among the Monte Carlo codes employed. Of all codes only the results from ACCEPT 3.0 were in good agreement with experimental data. The authors concluded that differences among the Monte Carlo codes might be accountable to differences on the physic transport parameters.

The Monte Carlo code MCNPX was used to perform a comparison between a proton therapy and a CCB ^{106}Ru eye plaque (Mourtada et al., 2005). Simulation results were in agreement with those obtained by Cross et al. (2001) using MCNP4B and Taccini et al. (1997) using GEANT3 but differences observed by Cross et al. (2001) between MCNP4B and ACCEPT 3.0 are similar to those found between MCNPX and ACCEPT 3.0 and radiochromic film data (Soares et al., 2001). A more exhaustive study was conducted by Hermida-López (2013), who used the PENELOPE code to model 12 eye plaques from the manufacturer BEBIG (Eckert & Ziegler). All these studies the emitter distribution of the radioactive substance was considered homogeneous and the dose was deposited in water phantoms (Hermida-López, 2013).

The work presented in this chapter consists of the accurate determination of the dose distributions produced by two generic eye plaques, models CCA and CCB, in a water phantom using a modified version of the penEasy code. Simulation results are compared with previously published data. This chapter follows closely the work presented in Brualla et al. (2013) which was published one year before the work of Hermida-López.

2.2 Methods

2.2.1 Sampling a probability distribution over a spherical cap

The way in which the main steering program penEasy can simulate a source with the shape of a spherical cap, such as that of a ruthenium eye plaque, is by inserting the mathematically defined spherical cap in a parallelepiped. penEasy then samples initial positions of particles inside the parallelepiped and only those which fall inside the volume of the cap are subsequently simulated. This approach is inefficient since a particles falling outside the cap imply a waste of random numbers.

To improve the simulation efficiency, a routine to sample the probability distribution over a spherical cap was programmed in penEasy. This modification ensures that the particle sampling process is carried out completely at the source and that all random numbers sampled are used.

Let us derive the probability distribution over a spherical cap. To do so, let us consider a spherical cap of unit radius. The surface

$$S = \int_0^{\theta_0} \int_0^{2\pi} \sin\theta \, \mathrm{d}\theta \, \mathrm{d}\phi, \tag{2.1}$$

represents the inner surface of the plaque models simulated herein in which θ_0 varies according to the specific plaque model. This value is 32° for the CCA eye plaque model and 40° for the CCB plaque model. The probability distribution function obtained for this spherical truncated surface is

$$p(\theta, \phi) = \left[\frac{\sin\theta}{1 - \cos\theta_0} \mathrm{d}\theta \right] \left[\frac{1}{2\pi} \mathrm{d}\phi \right], \tag{2.2}$$

where θ and ϕ are independent normally distributed random variables. The position of a particle from an isotropic source is generated by applying the inverse-transform method to the probability distribution function,

$$\theta = \arccos\left(1 - \xi_1 [1 - \cos\theta_0]\right), \qquad \phi = 2\pi\xi_2, \tag{2.3}$$

where ξ_1 and ξ_2 are uniformly distributed random numbers between 0 and 1.

It is useful to replace the variable of the polar angle θ by the variable

$$\mu = \left(\frac{1 - \cos\theta}{1 - \cos\theta_0} \right), \tag{2.4}$$

which varies from 0 (θ= 0) to 1 ($\theta = \theta_0$). Taking into consideration that the probability distribution function is isotropic, both variables are related as follows,

$$p_\mu(\mu) = p_\theta(\theta) \left(\frac{\mathrm{d}\mu}{\mathrm{d}\theta} \right)^{-1}. \tag{2.5}$$

Finally, the probability distribution function is expressed as follows

$$p(\mu, \phi) = [\mathrm{d}\mu] \left[\frac{1}{2\pi} \mathrm{d}\phi \right], \tag{2.6}$$

where a set of random points (μ, ϕ) uniformly distributed on the rectangle (0,1) x (0,2π) correspond to the coordinates (θ,ϕ) of a particle sampled on the inner cap surface of unit radius.

2.2.2 Geometric modeling of the CCA and CCB eye plaques

The modeled plaques correspond to a generic CCA and CCB eye plaques. These plaques are shaped as spherical caps. Table 2.1 shows the geometrical characteristic parameters of these plaques. Both have the same inner radius of 12.0 mm but the outer diameter of the caps across the rim is different, being 15.3 mm for the CCA model and 20.2 mm for the CCB model. The thickness of both plaque models is 1.0 mm.

Figure 2.1 shows the generic structure of ^{106}Ru eye plaques. It is made by three pure silver layers. The most external layer is 0.7 mm of thickness and corresponds to the shielding of the plaque. The second layer, or active layer, is 0.2 mm of thickness and it is on its inner surface where the radioactive substance has been electrolytically deposited. This second layer does not cover the whole surface of the plaque, as it only extends up to 0.7 mm from the cap rim. The thickness of the radioactive substance (Astrahan, 2003) is neglected in the simulations since it amounts to 0.1 μm. The third layer, or window layer, is 0.1 mm of thickness.

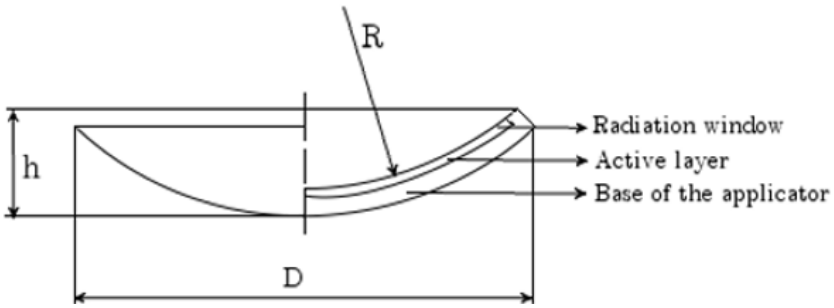

FIGURE 2.1: Cross section of a generic eye plaque showing its inner structure: base, active and window layer. The diameter D, the radius R and the height h are also observed.

TABLE 2.1: Geometrical features of the CCA and CCB eye plaque models. All features are obtained from the ICRU 72 Report (ICRU, 2004).

Model	diameter D (mm)	height h (mm)	active diameter D_a(mm)	radius of curvature R (mm)
CCA	15.3	3.3	13.0	12.0
CCB	20.2	5.4	17.8	12.0

2.2.3 Beta decay spectra code

The PENELOPE code cannot directly simulate beta radiation spectra from a radionuclide. For this reason a modification is needed. The modification is carried out in the penEasy code by programming the decay of ^{106}Rh to ^{106}Pd using the five decay paths with highest yields, namely, 3.450 MeV (78.6%), 3.050 MeV (8.1%), 2.410 MeV (10.0%), 2.000 MeV (1.77%) and

1.539 MeV (0.46%). The endpoint energy for each primary particle previously sampled is chosen at random taking into consideration the probabilities given by the yields. The initial energies of the electrons are then sampled randomly from the corresponding beta decay spectrum. This last part is the one that has been introduced into penEasy using an adapted version of the EFFY code (García-Toraño and Grau, 1985). The code uses the Fermi theory to describe the beta decay.

2.2.4 Simulation geometry

The geometry of the simulation consists of the eye plaque considered and the water phantom that surrounds it. Both elements are modeled using the geometric package PENGEOM contained in PENELOPE. The package allows to define different bodies grouping quadric surfaces. The plaques were modeled in PENGEOM according to the dimensions given by the manufacturer (see section 2.2.2). The modeled plaques are located at a distance to the center of the water phantom equal to the radius of curvature of the plaques, that is, the focus of the plaques coincides with the geometrical center of the water phantom. The water phantom is defined as a sphere of 3.0 cm of radius. The material files used to characterize the bodies of the simulated geometry are obtained from the PENELOPE material library. The three bodies of the plaques are defined using silver with a mass density of 10.5 g cm^{-3}. For the phantom, the material is water with a mass density of 1.00 g cm^{-3}. Although the mean excitation energy for liquid water recommended by ICRU Report 90 is 78 eV (ICRU, 2016), the value used in the PENELOPE code version 2008 for all simulations performed in this thesis is 75 eV, which corresponds to the previous value recommended by ICRU Report 37 (ICRU, 1984).

2.2.5 Simulation parameters

The simulation transport parameters used in all the simulations performed are shown in table 2.2.

TABLE 2.2: Values of the PENELOPE simulation transport parameters for each material and type of particle transported.

Material	EABS (e^-) (keV)	EABS (γ) (keV)	EABS (e^+) (keV)	C1	C2	WCC (keV)	WCR (keV)	DSMAX (cm)
Water	100	10	100	0.1	0.1	100	10	1.0×10^{30}
Silver	100	10	100	0.005	0.005	100	10	1.0×10^{30}

For each run 10^8 primary histories are simulated and no variance-reduction techniques are applied in the simulations performed. That amount of initial particles assures that the standard statistical uncertainty is lower than 0.5% for the simulation of both plaques. The absorbed dose is tallied in a grid of $60\times60\times30$ bins of $0.5\times0.5\times0.5$ mm^3 using a system of reference in Cartesian coordinates and centered at the focus of the plaques, that is the center

of the water phantom. The grid ranges from -15.0 mm to 15.0 mm on the x and y axes that correspond to the direction perpendicular to the symmetry axis of the plaques, whose grid ranges from 0.0 mm to 15.0 mm.

For reporting depth dose distributions along the symmetry axis of the plaques the origin of the profile is located at the inner surface of the plaques. Lateral profiles are determined at specific depths of 1.25 mm, 2.25 mm, 3.75 mm, 5.25 mm, 6.75 mm and 8.25 mm. The lateral profiles range from -12.0 mm to 12.0 mm at depths greater than 3.75 mm for the CCA plaque, and at depths greater than 6.75 mm for the CCB plaque. For shallower depths, the lateral profiles are inside the plaque height h (see section 2.2.2) and a *partial-volume effect* is observed. This effect occurs when a bin is partly filled with water and silver and is not taken into account for reporting the lateral profiles.

Doses tallied in PENELOPE are expressed in eV g^{-1} per primary history while the units of the experimental data are given in mGy min^{-1}. It is necessary to express the dose in the same units to compare the simulation results with the manufacturer data. The factor $5.7678353532\times10^{-4}$ transforms eV g^{-1} into mGy h^{-1} MBq^{-1}. When the irradiation time is expressed in mGy min^{-1} MBq^{-1} the conversion factor is 9.613058922×10^{-6}. Notice that the simulated dose is expressed in terms of primary particles, therefore it is necessary to know the activity of the plaques to give the dose in mGy min^{-1}. The nominal activities given by the manufacturer are 13.7 MBq and 25.9 MBq for the generic CCA and CCB plaques (Eckert & Ziegler BEBIG, 2011).

2.3 Results

Simulated depth dose profiles are compared to experimental data for both plaques. Simulated lateral profiles and isodose lines are plotted without comparison to experimental results since they were not available.

2.3.1 CCA plaque

For the CCA plaque the depth dose experimental data used to compare with the simulation are courtesy of Prof. G. Taccini (*Department of Medical Physics, S. Martino Hospital, Genoa, Italy*) (Taccini et al., 1997) and those provided by the manufacturer in the certificate of the CCA1364 plaque. Plot (A) of figure 2.2 shows the comparison among the three data sets in terms of relative dose normalized at a depth of 2.0 mm, which is the usual normalization depth for ruthenium plaques. It is observed that the data from the manufacturer matches the simulation results along the whole curve while the comparison with Taccini shows a lower degree of agreement for depths greater than 3.0 mm. The percentage local differences with the simulated data are 11% at 3 mm, 11% at 4.0 mm, 20% at 5.0 mm and 29% at 6.0 mm of depth. Plot (B) of figure 2.2 shows the comparison between the simulated and manufacturer data in terms of absolute dose rate. To obtain the absolute dose rate per unit of activity the aforementioned conversion factor is used. The data from Taccini does not appear in this plot since

the activity of his plaque was not provided. Vertical lines indicate depths at which the lateral profiles are computed.

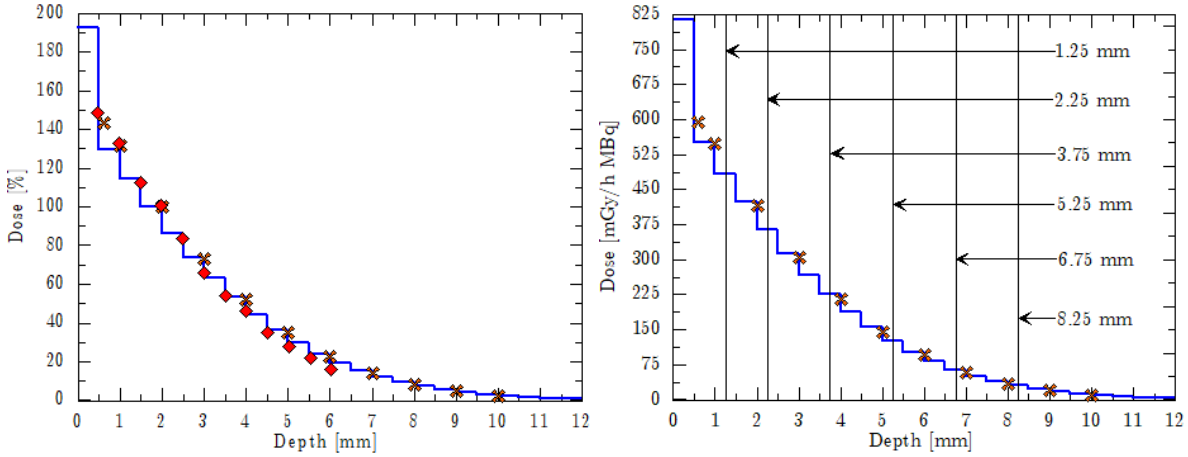

(A) Relative depth dose distribution. (B) Depth dose rate per unit of activity.

FIGURE 2.2: Relative depth dose and depth dose rate per unit of activity distributions along the symmetry axis. Simulation results correspond to a generic CCA plaque and are plotted with blue histograms. Standard statistical uncertainty bars are smaller than the symbol size used for experimental data, and in all cases smaller than 0.5%. Experimental data for the specific CCA1364 plaque are plotted with orange crosses. Experimental data for a specific CCA plaque (number unknown) from Taccini are plotted with red diamonds.

Figure 2.3 (A) shows lateral profiles tallied along distances perpendicular to the symmetry axis at different depths for a generic CCA plaque. Lateral profiles at a depth larger than the height h of the plaque (see table 2.1) are plotted along a length wider than the diameter of the plaque. Lateral profiles at a depth smaller than the height of the plaque are only plotted within the boundaries of the spherical cap to avoid partial volume effects.

Figure 2.4 (A) shows the isodose lines in mGy h^{-1} MBq^{-1} for the generic CCA plaque. The lines plotted correspond to 120%, 100%, 80%, 60%, 40% and 20% of the value of the reference dose measured by the manufacturer at a depth of 2.0 mm.

2.3.2 CCB plaque

For the CCB plaque, the depth dose experimental data used to compare with the simulation are courtesy of Prof. Theodor W. Kaulich (*Department of Medical Physics, University of Tübingen, Germany*) (Kaulich et al., 2004) and those provided by the manufacturer on the certificate of the CCB1256 plaque. Plot (A) of figure 2.5 shows the comparison among the three data sets in terms of relative dose normalized at 2.0 mm. It is observed that the data provided by the manufacturer and the values obtained by Kaulich match the simulation results at all depths. Plot (B) shows the comparison between the simulated and manufacturer data in terms of absolute dose. To obtain the absolute doses the aforementioned conversion factor and activity are used. The data from Kaulich does not appear in this plot since the activity of his plaque

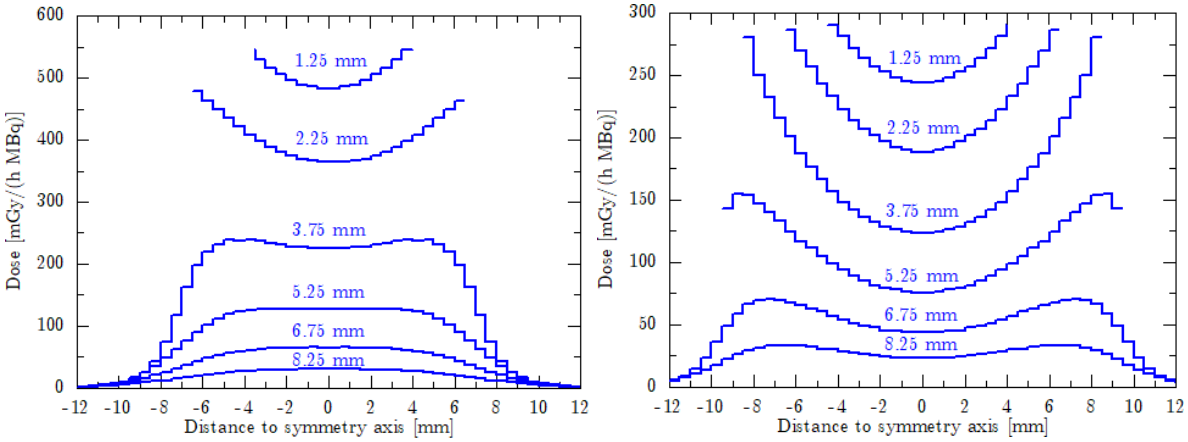

(A) CCA eye plaque. (B) CCB eye plaque.

FIGURE 2.3: Lateral profiles perpendicular to the symmetry axis for a generic CCA and CCB plaques. Simulation results are plotted with blue histograms.

was not provided. In this case, the agreement at shallow depths is lower. The simulated doses are 14% lower at 1.0 mm of depth, 10% at 2.0 mm, 8% at 3.0 mm and 5% at 4.0 mm with respect to the local values of the experimental data given by the manufacturer. Vertical lines show the depth at which lateral profiles are computed.

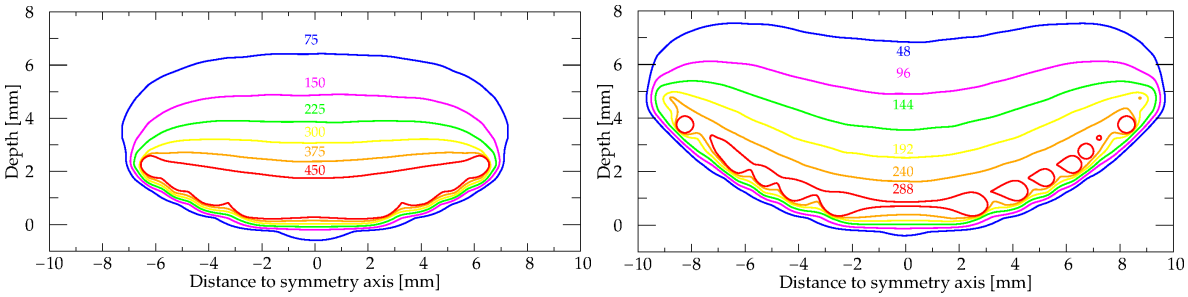

(A) CCA eye plaque. (B) CCB eye plaque.

FIGURE 2.4: Isodose lines in mGy h^{-1} MBq^{-1} for a generic CCA and CCB plaque models.

Figure 2.4 (B) shows the simulated isodose lines for the generic CCB plaque. The lines plotted correspond to 120%, 100%, 80%, 60%, 40% and 20% of the value of the reference dose measured by the manufacturer at 2.0 mm of depth in mGy h^{-1} MBq^{-1}. For this plaque it is observed that the isodose line corresponding to the 120% of the reference dose is contained inside the plaque volume. This is a consequence of the discrepancy between the experimental and simulated data at shallow depths.

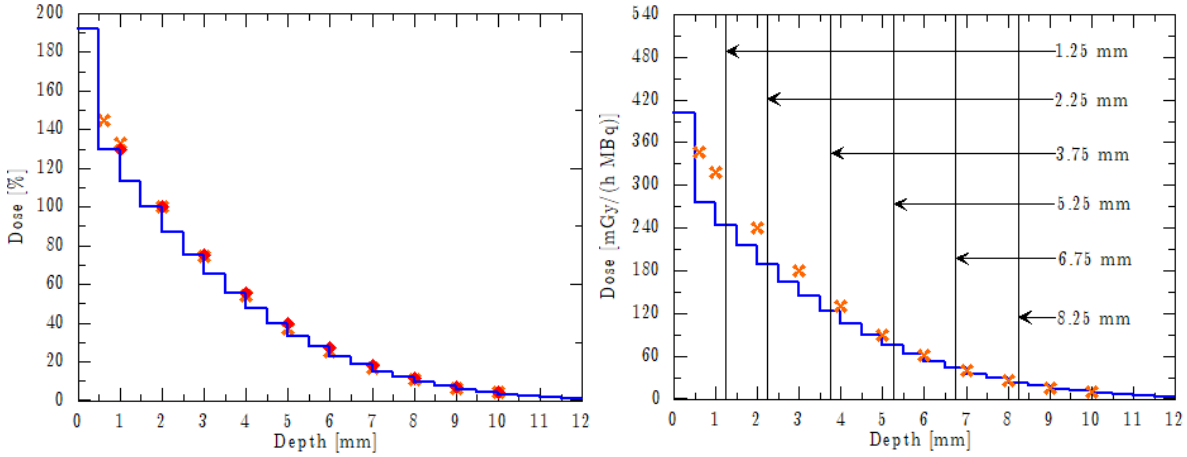

(A) Relative depth dose distribution.

(B) Depth dose rate per unit of activity.

FIGURE 2.5: Relative depth dose and depth dose rate per unit of activity along the symmetry axis. Simulation results correspond to a generic CCB plaque and are plotted with blue histograms. Standard statistical uncertainty bars are smaller than the symbol size used for experimental data, and in all cases smaller than 0.5%. Experimental data for the specific CCB1256 plaque are plotted with orange crosses. Experimental data for a specific CCB plaque (number unknown) from Kaulich are plotted with red diamonds.

2.4 Discussion

For all the eye plaques analyzed, the simulated relative depth doses match the relative experimental results provided in the certificate of the plaques and also reproduce the experimental results obtained in previous works for two specific CCA and CCB eye plaques (numbers unknown). The simulated distributions of the dose rate per unit of activity for the generic CCA and CCB plaques reproduce the corresponding experimental values with good agreement, with the exception of the CCB plaque near the surface where slight differences appear between experimental and simulated data. These differences become evident owing to the absolute dosimetry employed and reflect the discrepancies between the actual heterogeneous emitter substance distribution and the homogeneous approximation. The relative dosimetry hides these discrepancies.

Chapter 3

Monte Carlo computation of absorbed dose distributions produced by the heterogeneous CCA1364 and CCB1256 eye plaques in a water phantom

3.1 Introduction

The simulation of absorbed dose distributions from ruthenium plaques whose emitter substance is considered to be homogeneously deposited has been widely studied (Sánchez-Reyes et al., 1998; Cross et al., 2001; Fuss et al., 2011; Hermida-López, 2013; Brualla et al., 2013). However, it is also well known that the manufacturing process results in an heterogeneous distribution of the emitter substance. Consequently, there are not two identical plaques. The presence of heterogeneities is consistent with the appearance of hot or cold areas over the inner surface of the plaques. The activity of these hot spots can exceed the average by about 25% (e.g., in the case of the CCB1256 plaque presented in this thesis). These hot and cold spots have a clear effect on the dose distribution, which is neglected when the simulation considers the radioactive substance as homogeneously distributed. To the best of our knowledge the only treatment planning system for ^{106}Ru eye plaques that takes into account, to some extent, the inhomogeneities of the plaques is Plaque Simulator (version 6.4.3 or later) (Astrahan, 2003) considering the sparse measurements provided by the manufacturer in the certificate of the plaques. This program uses analytical models to perform the simulation of radiation transport.

This chapter presents the simulations of two actual plaques, named CCA1364 and CCB1256, inside a water phantom using the Monte Carlo code PENELOPE while considering the actual heterogeneous distribution of each plaque. Results are compared with experimental data and the corresponding homogeneous approximations. The contents of this chapter were published by the author of this thesis and coauthors in the *Ocular Oncology and Pathology* journal (Zaragoza et al., 2017).

3.2 Materials and methods

The plaques considered in this chapter are the specific CCA1364 and CCB1256 from the Essen University Hospital. The geometric parameters of these plaques are the same that were defined in section 2.2.2.

3.2.1 Normalized experimental distributions of the CCA1364 and CCB1256 eye plaques

The distribution of the emitter substance for the CCA1364 and CCB1256 plaques were measured using a specific device developed at TU Dortmund (Eichmann et al., 2009). The device measures the dose rate profile over the inner surface of the plaques at a constant small distance covering the whole surface. To achieve this, the device uses a guiding system linked to a scintillation detector. The whole process assures a high density of measured surface points and a gapless coverage of the surface of the plaque, in contraposition with the sparse measurements provided in the certificate of the plaques and used by Plaque Simulator.

The experimental emitter distributions of the plaques used in this thesis are courtesy of Dr. rer. nat. M. Eichmann (*Fakultät Physik, Technische Universität Dortmund, Germany*). The raw emitter distributions from the plaques are transformed into normalized probability distributions taking as reference the maximum value of the dose emission rate for both plaques.

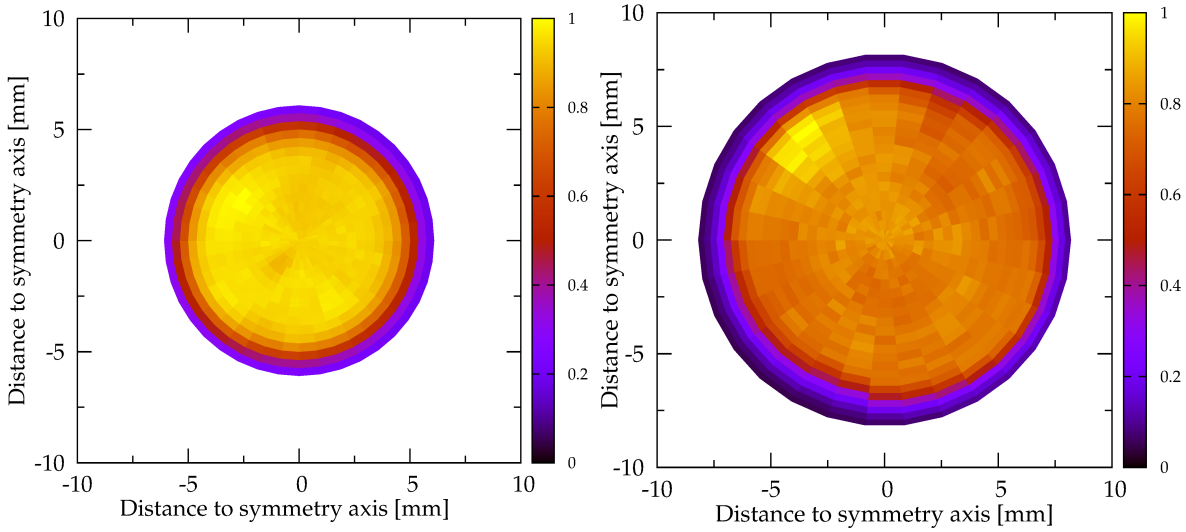

(A) CCA1364 eye plaque.

(B) CCB1256 eye plaque.

FIGURE 3.1: Normalized experimental surface distribution of the emitter substance for both eye plaques.

Plot (A) in figure 3.1 shows the normalized experimental emitter map for the CCA1364 plaque. The largest heterogeneity for this plaque is about 18% with respect to the average value. The area covered by hot spots in this plaque is rather small, thus yielding a quite homogeneous distribution. Notice that the emitter map is off-centered with respect to its symmetry

axis. This off-center is maximum along the diameter that forms an angle of 18° with respect to the positive horizontal axis. The normalized emitter map for this plaque contains 16×30 polar bins of 2.5°×12.0° corresponding to the polar and azimuthal angles, respectively. Polar angle ranges from 0.0° to 37.5°, while azimuthal angle ranges from 0° to 360°. The normalized emitter map corresponding to the CCA1364 plaque contains a total of 480 measured points which means a factor 14.5 greater than the 33 measured values provided on the certificate of the plaque.

Plot (B) in figure 3.1 shows the normalized emitter map for the CCB1256 plaque. It is observed the presence of a well-defined hot spot whose heterogeneity amounts to 25% with respect to the average value. The bin with highest rate of the hot spot is located at an azimuthal angle of 132° measured with respect to the positive horizontal axis. The normalized emitter map for this plaque contains 23×30 polar bins of size equal to 2.5°×12.0°. For this plaque model the polar angle ranges from 0.0° to 55.0°. For this plaque, the normalized emitter map contains a total of 690 measured points which means a factor 21 greater in contradistinction with the sparse map provided in the certificate of the plaque.

Because penEasy (version 2010-08-07) is not prepared to simulate a spectrum emitted from a heterogeneous source distributed on a spherical cap a modification in the code is needed. The algorithm implementing this source is the following:

- For each primary electron, an initial position is sampled at random over the inner layer of the spherical cap according to the probability distribution explained in section 2.2.1.
- An emission probability is sampled using a normalized, uniformly distributed random number. The primary particle is accepted only if the uniformly distributed sampled random number is equal to or lower than the normalized experimental distribution yielded for the region where the particle has been previously located; otherwise, the particle is rejected and the algorithm returns to the first step.
- The initial energy of the primary electron is sampled from the corresponding beta decay code explained in section 2.2.3.
- The initial isotropic flight direction is sampled at random.

The probability emission map cover the entire inner surface of the plaques. However, the emitter substance, as it was explained previously, does not reach the rim of the plaque. This is evident from figures 3.1 where a blue ring circles the active area of each plaque. When sampling the initial position of a primary electron the entire surface of the plaque must be considered. In contradistinction, notice that the simulation of the homogeneous plaque only considers as possible initial positions of primary particles those over the active surface.

3.2.2 Simulation geometry

For the eye plaques as well as for the water phantom the considered geometries are the same as the ones employed in the previous chapter (see section 2.2.4). The material files are also the same.

Notice that the hot spot of the CCB1256 plaque breaks the axial symmetry present in the homogeneous case. Rotations around the main symmetry axis of the plaque will yield different lateral distributions tallied along the x axis (horizontal positive axis perpendicular to the main symmetry axis). To observe the effect of the hot spot in the lateral profile the plaque is rotated 48° counterclockwise .

For the case of the CCA1364 it was observed that rotations around the symmetry axis produced no statistically significant differences in the lateral profile.

3.2.3 Simulation parameters

The number of histories simulated are 10^8. The standard statistical uncertainty achieved is lower than 0.5%. The transport parameters are also the same used previously (see table 2.2). The absorbed dose distribution is tallied in the same grid of $60\times60\times30$ bins of $0.5\times0.5\times0.5$ mm^3 centered at the focus of the plaques, that is coincident with the center of the water phantom. The grid ranges from -15.0 mm to 15.0 mm on the axes perpendicular to the symmetry axis which ranges from 0.0 mm to 15.0 mm. Doses tallied are transformed into mGy h^{-1} MBq^{-1} using the aforementioned factor (see section 2.2.5).

3.3 Results

Simulated depth doses from the actual CCA1364 and CCB1256 plaques are compared with their corresponding homogeneous simulated depth doses and also with the experimental data provided by the manufacturer in the certificates of the plaques. Although there is no experimental data for lateral profiles and isodose lines, a comparison between the homogeneous and heterogeneous simulations is also presented.

3.3.1 Comparison between the ideal homogeneous CCA and the actual heterogeneous CCA1364 eye plaques

Figure 3.2 shows the comparison between the ideal homogeneous CCA plaque (CCA plaque from now on) and the actual heterogeneous CCA1364 plaque (CCA1364 from now on) in terms of absolute dose rate per unit of activity. The comparison of the depth dose among the experimental data and the simulations of the CCA and the CCA1364 is shown in figure 3.2 (A). The simulated depth dose obtained from CCA1364 plaque reproduces better the experimental data than the simulated dose from the CCA plaque. At the reference depth of 2.0 mm the dose for the CCA1364 eye plaque is 7.9% higher than the dose of the CCA plaque. Vertical lines on the plot indicate the depths at which lateral profiles are computed. Comparison between

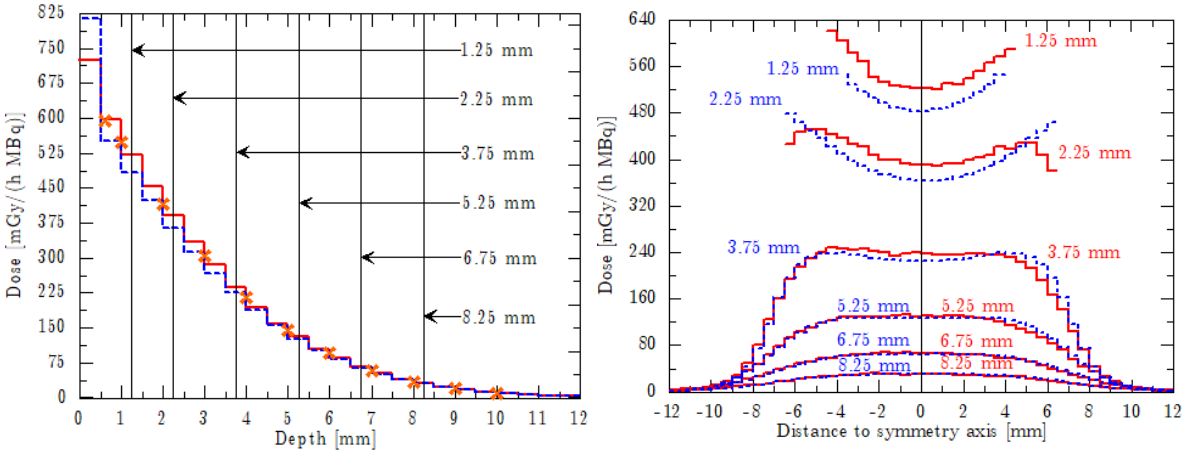

(A) Depth dose.

(B) Lateral profile.

FIGURE 3.2: Depth dose and lateral profiles comparison for the CCA eye plaque model. The simulated ideal homogeneous distribution corresponding to the CCA plaque is plotted with dashed blue histograms, the simulation of the actual heterogeneous distribution corresponding to the CCA1364 plaque is plotted using red histograms and the manufacturer experimental data is plotted with orange crosses. The standard statistical uncertainty of the simulated data is smaller than the thickness of the lines.

simulated lateral profiles are shown in plot 3.2 (B). Lateral profiles at a depth larger than the height h of the plaque (see table 2.1) are plotted along a length wider than the diameter of the plaque. Lateral profiles at a depth smaller than the height of the plaque are only plotted within the boundaries of the spherical cap to avoid partial volume effects. Notice in the lateral profile that the slight asymmetry mentioned before is revealed (see section 3.2.1). It is also observed the shorter lateral coverage of the heterogeneous plaque with respect to the homogeneous assumption at the relevant shallow depth of 2.25mm. The disagreement between the CCA and the CCA1364 distributions is greater near the symmetry axis. Regarding each depth, the differences along the symmetry axis are 8% observed on the lateral profile computed at 1.25 mm, 7% at 2.25 mm, 6% at 3.75 mm, 3% at 5.25 mm, 4% at 6.75 mm, and 1% at 8.25 mm.

3.3.2 Comparison between the ideal homogeneous CCB and the actual heterogeneous CCB1256 eye plaques

Figure 3.3 shows the comparison between the ideal homogeneous CCB plaque (CCB from now on) and the actual heterogeneous CCB1256 plaque (CCB1256 from now on) also in terms of absolute dose rate per unit of activity. The comparison of the depth dose among the experimental data and the simulations of the CCB and CCB1256 is shown in figure 3.3 (A). The simulated depth dose obtained for the CCB1256 plaque matches the experimental data. Due to the greater heterogeneity observed in figure 3.1 (B), there are greater discrepancies on the simulations of the depth doses along the symmetry axis between the CCB1256 and the CCB plaques. At the reference depth of 2.0 mm the dose for the CCB1256 amounts 22% with respect

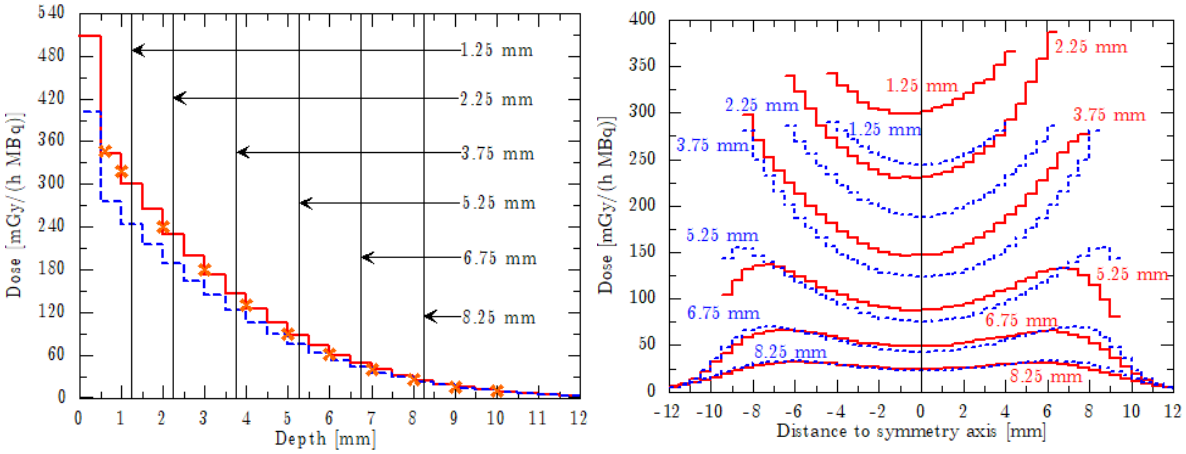

FIGURE 3.3: Depth dose and lateral profiles comparison for the CCB plaque model. The simulated ideal distribution corresponding to the CCB plaque is plotted in dashed blue line histograms, the actual simulated distribution corresponding to the CCB1256 plaque is plotted in red histograms and the manufacturer experimental data is plotted in orange crosses. The standard statistical uncertainty of the simulated data is smaller than the thickness of the lines.

to the CCB plaque. Vertical lines on the plot also show the depths at which lateral profiles are computed. Comparison between simulated lateral profiles are shown in figure 3.3 (B). Lateral profiles at a depth larger than the height h of the plaque (see table 2.1) are plotted along a length wider than the diameter of the plaque. Lateral profiles at a depth smaller than the height of the plaque are only plotted within the boundaries of the spherical cap to avoid partial volume effects. The disagreement between the CCB and the CCB1256 distributions is greater near the symmetry axis. Regarding each depth, the differences along the symmetry axis are 24% observed on the lateral profile computed at 1.25 mm, 23% at 2.25 mm, 20% at 3.75 mm, 18% at 5.25 mm, 14% at 6.75 mm, and 8% at 8.25 mm.

3.3.3 Isodose

Figure 3.4 shows the comparison between the ideal and the actual simulated isodose curves for each plaque model. Plot 3.4 (A) of this figure shows the comparison between the CCA and the CCA1364 eye plaques with isodose lines corresponding to 120%, 100%, 80%, 60%, 40% and 20% of the reference dose measured by the manufacturer at 2.0 mm of depth. The differences between isodose lines are smaller at a greater distance from the plaque surface and become very similar for a value of 225 mGy h^{-1} MBq^{-1}, which corresponds to 60% of the reference dose. The difference in depth between the ideal and the actual isodose lines corresponding to 450 mGy h^{-1} MBq^{-1} (120%) and 375 mGy h^{-1} MBq^{-1} (100%) is 0.2 mm, while for 300 mGy h^{-1} MBq^{-1} (100%) and 225 mGy h^{-1} MBq^{-1} (60%) is 0.1 mm. Notice that the asymmetry of the emitter map is also observed in the isodose lines. Plot 3.4 (B) of this figure shows the comparison between the CCB and the CCB1256 eye plaques with isodose lines corresponding to 120%, 100%, 80%, 60%, 40% and 20% of the reference dose measured by the

manufacturer at 2.0 mm of depth. The differences between simulated isodose lines also decrease with distance to the plaque surface. The isodose line from both the ideal and the actual plaque are compatible within the statistical uncertainty for a value of 48 mGy h^{-1} MBq^{-1}, that is, at 20% of the reference dose. The isodose line of 288 mGy h^{-1} MBq^{-1}, which corresponds to 120% of the reference dose, is plotted exclusively for the CCB1256 due to for the homogeneous assumption this line is inside the eye plaque. At the same time, this isodose line coincides with the isodose line of 240 mGy h^{-1} MBq^{-1} for the CCB that is the isodose line corresponding to the 100% of reference dose. The difference in depth between the ideal homogeneous CCB and the heterogeneous CCB1256 isodose lines corresponding to 240 mGy h^{-1} MBq^{-1} (100%) is 1.8 mm, for the 192 mGy h^{-1} MBq^{-1} (80%) is 0.6 mm, for the 144 mGy h^{-1} MBq^{-1} (60%) is also 0.6 mm, for the 96 mGy h^{-1} MBq^{-1} (40%) is 0.3 mm, and for the 48 mGy h^{-1} MBq^{-1} (20%) is 0.2 mm.

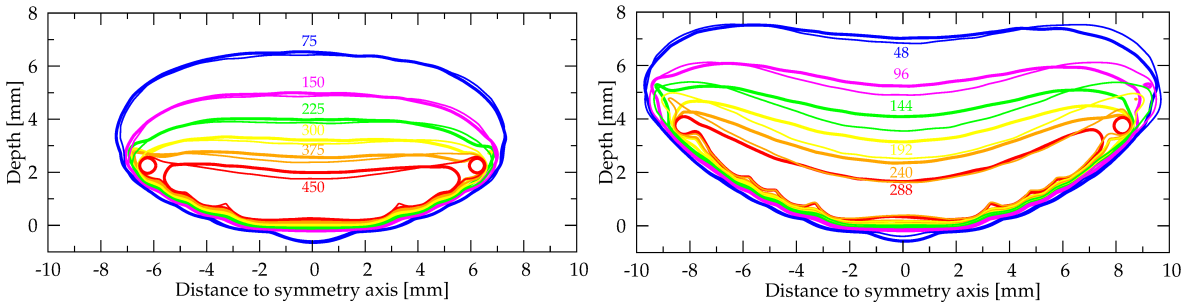

(A) CCA1364 eye plaque.

(B) CCB1256 eye plaque.

FIGURE 3.4: Isodose lines for generic CCA and CCB eye plaques compared to the corresponding CCA1364 and CCB1256 plaques, respectively. Thin lines correspond to the generic plaques while thick lines correspond to the actual plaques. Percentage values of the isodose lines are computed according to the reference dose measured given by the manufacturer at a depth of 2.0 mm. Isodose line units are given in mGy h^{-1} MBq^{-1}.

3.4 Discussion

Simulations using the actual emitter maps reproduce the experimental data provided by the manufacturer better than the simulations which consider ideal homogeneous emitter maps.

For both plaque models, the differences observed in the depth dose, the lateral profiles and the isodose lines between the ideal homogeneous assumption and the actual heterogeneous distribution of the radioactive substance are inversely proportional to the distance to the plaque. These differences become relevant for distances lower than 4.0 mm for the CCA1364 plaque and lower than 6.0 mm for the CCB1256 plaque. The spatial extent of the discrepancies coincides with the range of treatment of uveal tumors for each of these plaques, therefore, it is evident that the homogeneous approximation produces results that bias the

dosimetry in the clinically relevant region. Consequently, for the plaques studied in this thesis, simulations that consider homogeneous distributions of the radioactive substance imply an overdosage to both the tumor and the adjacent tissues.

Chapter 4

Monte Carlo estimation of absorbed dose distributions produced from the CCA1364 and the CCB1256 eye plaques computed in an anthropomorphic phantom

4.1 Introduction

Although ^{106}Ru eye plaques have been used for decades (Brady and Hernández, 1992; Lommatzsch and Vollmar, 1966; Lommatzsch, 1977, 1986; Schueler et al., 2006; Mossböck et al., 2007), the determination of the dose distributions produced by eye plaques is still a challenge and further improvements are needed (Flühs et al., 1997; ICRU, 2004; Schueler et al., 2006; Thomson et al., 2019). Regarding the dose distribution provided by a given plaque, the manufacturer only provides the depth dose along the symmetry axis. Additionally, an scarce activity map of 33 points are provided in the certificate. Of these points, only 25 are determined on the surface of the plaques studied in this dissertation. This information is insufficient for an accurate determination of the absorbed dose distribution taking into consideration actual heterogeneities of a given plaque.

Models used in dosimetry calculations of ^{106}Ru eye plaques approximate the anatomy of the eye to an homogeneous water sphere (Sánchez-Reyes et al., 1998; Brualla et al., 2009; Fuss et al., 2011; Hermida-López, 2013; Stöckel et al., 2018). Even the available treatment planning system for these plaques considers the eye as a homogeneous water sphere using an idealized segmentation of the eyeball (Astrahan, 2003).

In 2012 Brualla et al. (2012b) used for the first time a voxelized eye phantom based on computed tomography images from a patient for the Monte Carlo simulation of an eye irradiation. This study considered the external electron beam irradiation of a conjunctival lymphoma. The segmented voxelized eye phantom produced for this study was subsequently used by this group for all publications related to ruthenium plaques.

Plaque simulator, the commonly used treatment planning system for ruthenium plaques, had usually considered the emitter substance to be homogeneously distributed over the inner surface of the plaques. From version 6.4.3 the program allows to take into account the scarce measurement map found in the plaque certificate although the algorithm uses analytical methods for the radiation transport.

In this chapter, dose distributions produced by the two ^{106}Ru eye plaques CCA1364 and CCB1256 are simulated in the voxelized anthropomorphic phantom first published in Brualla et al. (2012b). For both plaques, two configurations are considered depending on the distribution of the radioactive substance; ideal CCA and CCB eye plaques where the radioactive substance is homogeneously distributed and the actual CCA1365 and CCB1256 eye plaques where the radioactive substance is heterogeneously distributed. For the simulations different placements of the plaques are considered as well. Results for all the defined structures in the eyeball are plotted using cumulative dose-volume histograms, which plot the percentage of the volume of the segmented anatomical structure that receives a dose equal to or greater than the value in the abscissa. Comparisons are also made between these two plaque configurations and different placements to determine the differences between the absorbed dose especially at the structures at risk. The content of this chapter corresponding to homogeneous distribution of the radioactive substance was published in the *Strahlentherapie und Onkologie* journal (Brualla et al., 2013). Additionally, the data corresponding to actual distributions of the CCA1364 and CCB1256 are also presented in this chapter and currently accepted for publication in the *Ocular Oncology and Pathology* journal (Zaragoza et al., 2020).

4.2 Materials and methods

4.2.1 Voxelized geometry

The main steering program penEasy, using the geometry-handling subroutine penVox, allows to simulate quadric geometries superimposed on voxelized geometries simultaneously. This feature is employed for the simulation of the eye plaque, represented with quadric surfaces, on top of the voxelized anthropomorphic phantom of the eye.

Although only one phantom is used throughout this work, general conclusions can be derived, owing to the fact that the size of an emmetropic eye ball does not differ from one individual to another (Atchison et al., 2004).

The original computerized tomography scan of an anonymized patient had $512\times512\times59$ voxels of size $0.015625\times0.015625\times0.1$ cm^3. This original DICOM file was converted into ASCII format file grouping voxels. The resulting conversion yielded an ASCII file that has $256\times256\times59$ voxels of size $0.03125\times0.03125\times0.1$ cm^3. This last voxelized ASCII file is the one used as a phantom in PENELOPE simulations. Hounsfield units are converted into mass density values using the calibration curve of the computerized tomography scanner (Reynaert et al., 2007). The calibration curve used (continuous line) is shown in figure 4.1. Three materials are considered: water, air and bone. Figure 4.2 shows the transformation from Hounsfield

numbers into material density for the axial plane where the eye globe shows its maximum diameter, which corresponds to the slice 21 of the computerized tomography scan.

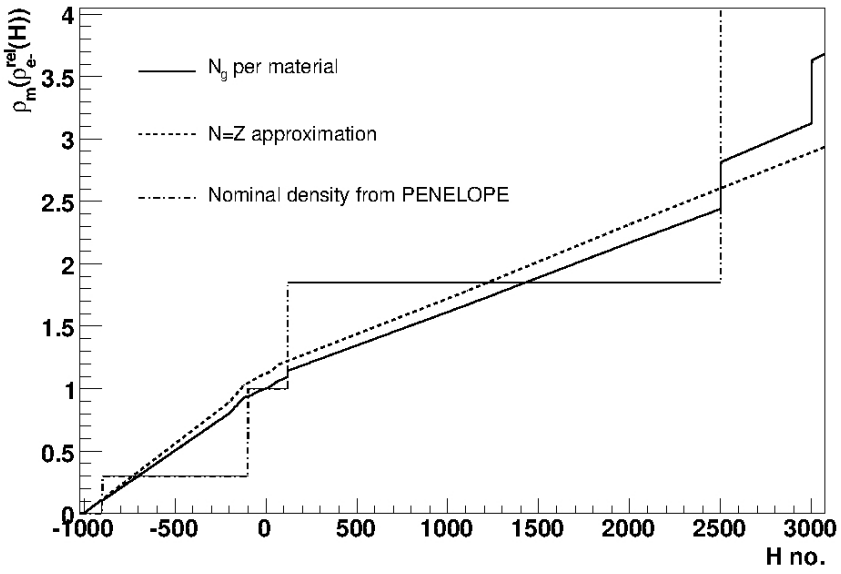

FIGURE 4.1: Calibration curve (continous line) used to transform Hounsfield numbers from the CT into material-density.

Table 4.1 shows the intervals for the Hounsfield units to material conversion.

TABLE 4.1: Conversion intervals of Hounsfield units into material.

Material	Hounsfield units interval	Material number
Air	$[-1024, -724)$	2
Water	$[-724, 216)$	1
Compact bone	$[216, 3000]$	3

4.2.2 Segmentation of anatomical structures in the eye

The human eye is a complex organ formed by different anatomical structures (Valentin and Streffer, 2002). Figure 4.3 shows the segmentation of the eye used in this thesis. To segment the anatomical structures of the eye two methods are used. For segmenting the sclera, the cornea, the anterior globe and the posterior globe, volumes are defined by grouping quadric surfaces (spheres and planes) and then selecting the voxels included within the volumes. For segmenting the eye lens, the papilla, the optic disk, the optic nerve and the lachrymal gland the voxels belonging to these volumes were manually identified and its coordinates (i,j,k) given to the segmentation program.

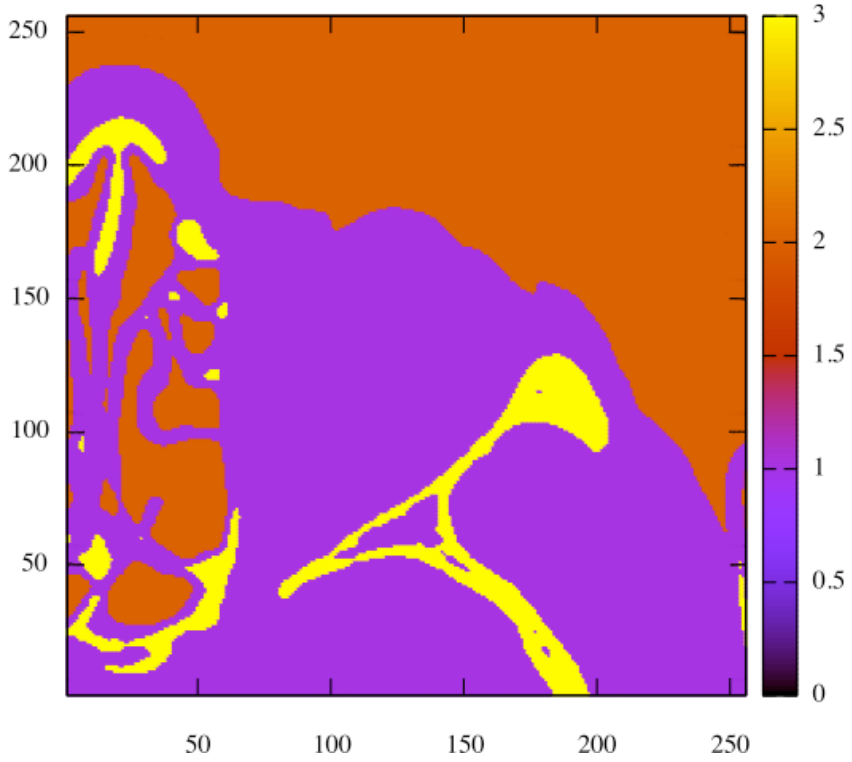

FIGURE 4.2: Material map obtained from the Hounsfield unit interval table 4.1. Values on the horizontal and vertical indicate voxel index. Three materials are considered: water (purple), air (orange) and bone (yellow).

The eyeball is defined as a sphere of 1.215 cm of radius centered at $3.825 \times 3.452 \times 2.100$ cm^3 in a Cartesian coordinate system whose origin is the lower left posterior vertex of the tomography scan. The equatorial plane of the eyeball is determined by a plane 15° above the horizontal axis of the computerized tomography that intersects the center of the eyeball. The sclera and the cornea are parts of the volume contained in two concentric spheres of outer radius the eyeball and inner radius of 1.045 cm. The cornea is the volume of a cap of outer diameter parallel to the equatorial plane of the eyeball of 1.100 cm across the rim of the external sphere. The rest of the volume contained between the spheres corresponds to the sclera. The equatorial plane also defines two internal volumes called anterior globe and posterior globe.

Although spheres and planes are used as boundary surfaces in the segmentation process for the sclera, the cornea, the anterior globe and the posterior globe, these structures are also defined in the voxelized tomography. This means that a voxel divided by a boundary surface needs to be assigned either the corresponding structure or to the outside. The selected criterion to decide if a voxel belongs or not to a segmented structure is if its center is inside it. An immediate consequence of this definition is that the thickness of the sclera and the cornea are not constant. Both range from approximately 1.2 mm to 2.1 mm depending on the number of voxels contained between the two boundary spherical surfaces used for defining them. The chosen value for the thickness is in agreement with the default value of 1.5 mm employed in

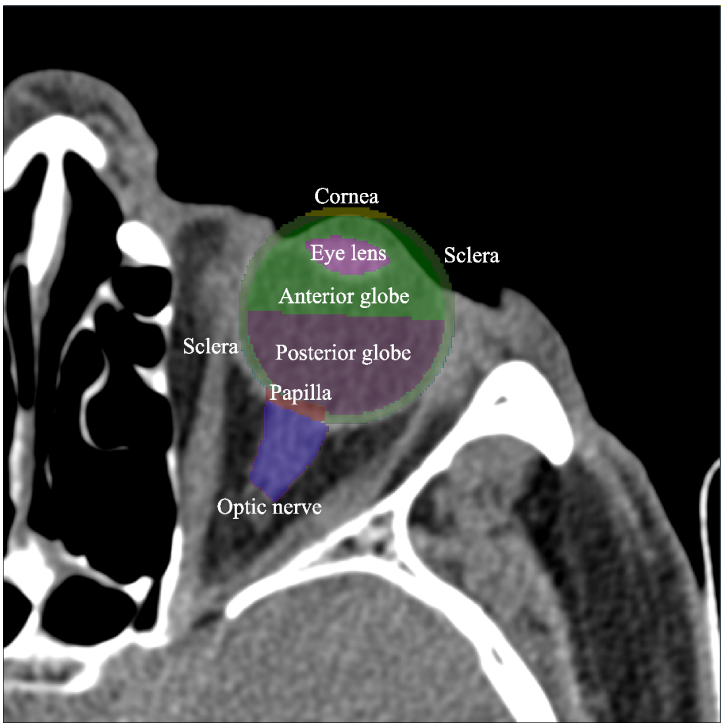

FIGURE 4.3: Plot of the axial plane where the eye shows its larger diameter. Notice that the lachrymal gland does not appear since it is located on other slices of the tomography.

the code EYEPLAN (Goitein and Miller, 1983) and gives a safety margin of 0.5 mm.

4.2.3 Placement of the plaques

Eye plaques are placed with its symmetry axis coplanar to the axial plane of the computerized tomography scan where the eyeball shows its largest diameter, which corresponds to the slice 21 of the tomography scan.

For the simulation of the CCA and CCA1364 plaques three different locations with respect to the equatorial plane of the eyeball previously defined are considered. Figure 4.4 shows these locations, which are named anterior, equatorial and posterior. Plot (A) shows the anterior location that is set 15° above the equatorial plane of the eye, that is 30° above the horizontal axis of the computerized tomography scan. Plot (C) and plot (D) show the equatorial location for the CCA and CCB plaques, respectively. The symmetry axes of the plaques coincide with the equatorial plane of the eye, that is 15° above the horizontal axis of the tomography scan. On plot (B) it is shown the posterior location of the CCA and CCA1364 plaques. It is set 30° below the equatorial plane of the eyeball, that is 15° below the horizontal axis of the tomography scan. For the simulations of the CCB and CCB1256 eye plaques only the equatorial location is considered.

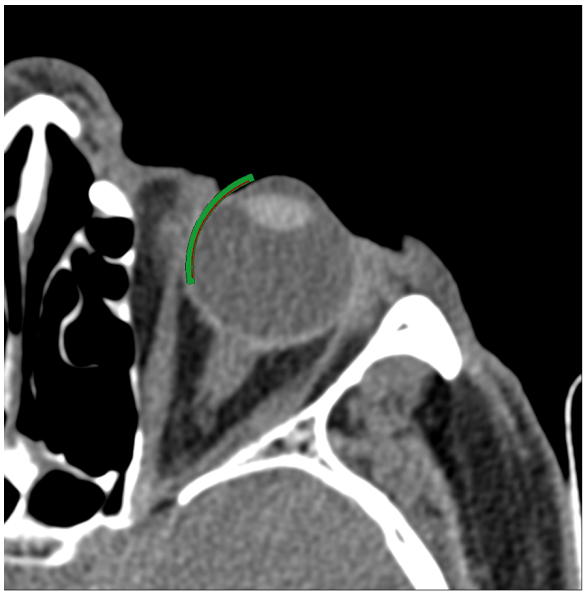

(A) Anterior location for a CCA plaque.

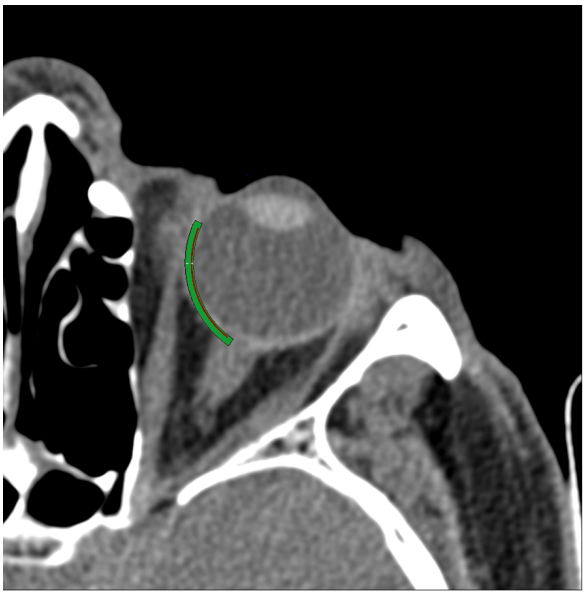

(B) Posterior location for a CCA plaque.

(C) Equatorial location for a CCA plaque.

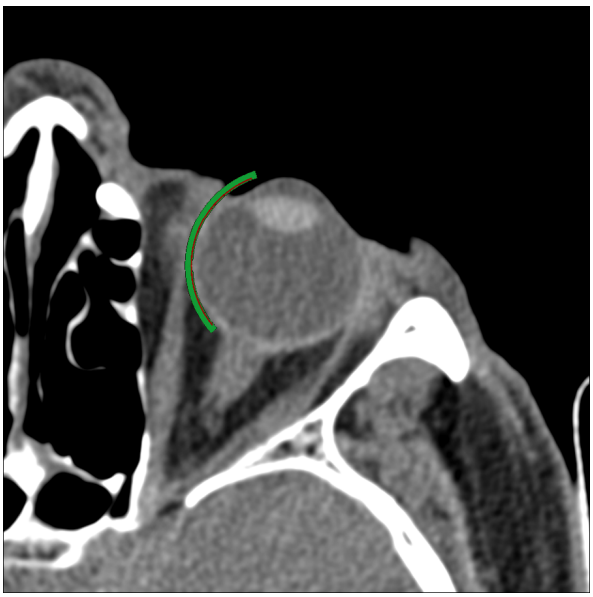

(D) Equatorial location for a CCB plaque.

FIGURE 4.4: Axial images of the computerized tomography (Slice 21) where the plaques location is embedded.

4.2.4 Orientation of the plaques

The influence of the heterogeneities on the emission map of the plaques (see section 3.2.1) is also studied. Rotations about the symmetry axis of the plaques allow to take advantage of these heterogeneities. The CCB1256 has a well-defined hot spot (see figure 3.1 (B)). Although the CCB1256 is placed only equatorially the effect of the relative position of the hot spot with respect to the segmented structures is determined. Three rotations are considered

taking into account the position of the hot spot with respect to the segmented structure under consideration. In the *original* rotation, the hot spot is located 42° degrees below the axial plane corresponding to the slice 21 of the tomography scan. In the *proximal* rotation the hot spot is oriented close to the segmented structure under consideration, while for the *distal* rotation the contrary holds. For both, the *proximal* and *distal* orientations, the polar bin of the hot spot with the largest activity is placed in the axial plane.

4.2.5 Transport parameters

The simulation transport parameters for all materials used in the simulations performed are shown in table 4.2.

TABLE 4.2: Values of PENELOPE simulation transport parameters used for each material.

Material	EABS (e^-) (keV)	EABS (γ) (keV)	EABS (e^+) (keV)	C1	C2	WCC (keV)	WCR (keV)	DSMAX (cm)
Water	10	1	10	0.02	0.02	10	1	0.1
Air	10	1	10	0.02	0.02	10	1	0.1
Bone	10	1	10	0.02	0.02	10	1	0.1
Silver (Applicator)	10	1	10	0.02	0.02	10	1	0.008
Silver (Emitter)	10	1	10	0.02	0.02	10	1	1.0×10^{30}

As in previous chapters, a number of 10^8 histories have been simulated assuring that the average standard statistical uncertainty of all voxels scoring more than 50% of the maximum dose is lower than 0.5% for all simulations. The simulated absorbed dose is tallied in a grid of $256\times256\times59$ corresponding to the voxels of the computerized tomography. PENELOPE yields the tallied absorbed dose in eV g^{-1} per primary particle. These units are converted into mGy h^{-1} MBq^{-1} using the aforementioned factor (see section 2.2.5) and also into mGy min^{-1} using the activities of the plaques. For the generic plaques the nominal activity for each model is used, while for the actual plaques the activities used are those reported in their certificates. Table 4.3 shows the nominal and reported activities.

4.3 Results and discussion

Comparisons of the absorbed dose in the segmented volumes are made using cumulative dose-volume histograms of, on the one hand, the absorbed dose rate per unit of activity and, on the other hand, the absorbed dose rate. Notice that the scale factor between these dose-volume histograms is proportional to the activity of each plaque which provides differences that must be taken into account. For the actual CCB1256 plaque, the existence of a located hot

TABLE 4.3: Nominal and reported activities of the generic and actual eye plaques, respectively.

Plaque	Activity (MBq)
CCA	13.7
CCA1364	11.6
CCB	25.9
CCB1256	27.3

spot allows also comparisons of the absorbed dose depending on the location of the hot spot with respect to the segmented volume analyzed.

4.3.1 Sclera

The sclera is the only segmented anatomical structure that is irradiated for all plaques and placements. Dose-volume histograms for equatorial placements are plotted on figure 4.5 while anterior and posterior placements appear in figure 4.6. Plaques and placements are compared via the maximum absorbed dose per unit of activity and the maximum absorbed dose rate.

Plot (A) in figure 4.5 shows the absorbed dose rate per unit of activity for plaques placed equatorially. The maximum dose rate per unit of activity is reached by the CCA1364 plaque. For the CCB1256 the absorbed dose rate per unit of activity is 43% lower. With respect to the CCA1364, the absorbed dose per unit of activity for the CCA and CCB homogeneous plaques are 40% and 64% lower, too. On plot (B), where the absorbed dose rate is plotted, the maximum is achieved by the CCB1256 which is 35% higher than the dose rate delivered by the CCA1364. Notice that for the homogeneous CCA and CCB plaques, the absorbed dose rates are lower than their respective actual plaque. That is, for the CCA it is 29% lower than the CCA1364 and, for the CCB it is 40% lower than the CCB1256.

For anterior and posterior placements, the maximum absorbed dose rate per unit of activity is reached with the CCA1364 eye plaque. Plot (A) in figure 4.6 shows that when the plaque is placed anteriorly, the absorbed dose rate per unit of activity is 6% higher than the same plaque in a posterior placement. It is also observed that the homogeneous distribution of the radioactive substance results in a lower absorbed dose for both placements. These absorbed dose rates are 37% and 44% lower than those obtained with the actual CCA1364 in the anterior and posterior placements, respectively. Plot (B) shows that the maximum absorbed dose rate is also reached by the CCA1364 plaque. For the anterior placement, the absorbed dose rate for the CCA is 25% lower than the CCA1364 plaque while for the posterior placement it is 33% lower, too.

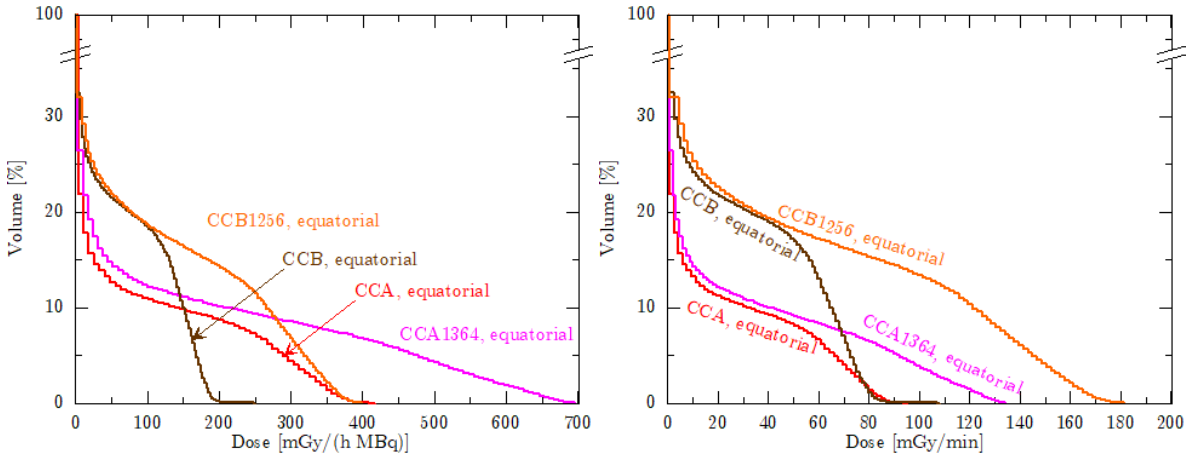

(A) Dose rate per unit of activity. (B) Dose rate.

FIGURE 4.5: Dose-volume histograms for the sclera according to different plaques in an equatorial placement. The standard statistical uncertainty of the simulated data is smaller than the thickness of the lines.

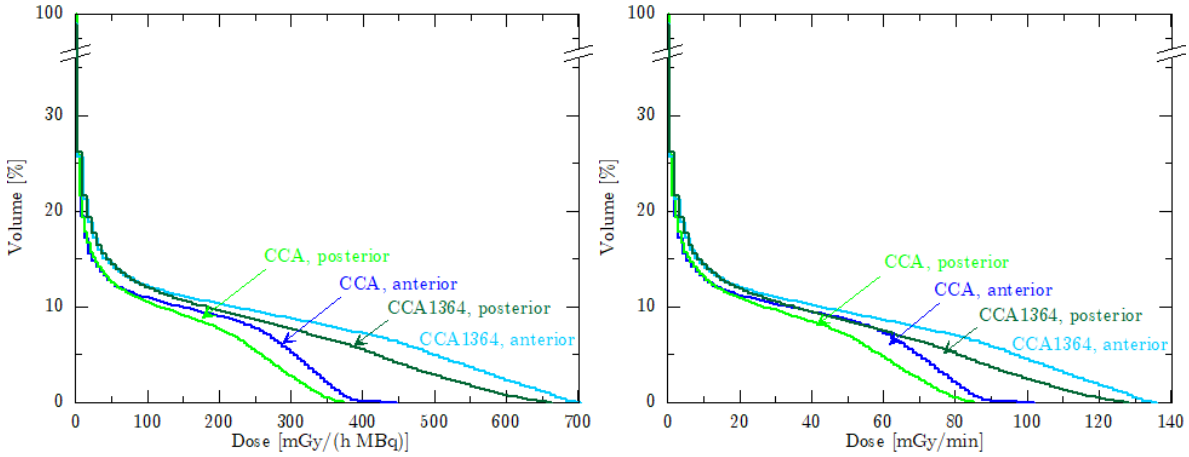

(A) Dose rate per unit of activity. (B) Dose rate.

FIGURE 4.6: Dose-volume histograms for the sclera using the CCA and CCA1364 plaques in the anterior and posterior placement. The standard statistical uncertainty of the simulated data is smaller than the thickness of the lines.

For all plaques, regardless of their emitter surface map, generic or actual, and also for the placements, all the cumulative dose-volume histograms for the sclera present a quasi-spherical symmetry. Therefore, the dose-volume histograms are nearly independent of the plaques position and also their emitting map. Consequently, dose-volume histograms for the sclera provide a confirmation of the correctness of the simulation performed.

4.3.2 Cornea

Figure 4.7 shows the absorbed dose in the cornea using plaques in an anterior and equatorial placement. The CCB1256 plaque is studied only *originally* rotated. Notice in this case that the posterior placement is not considered.

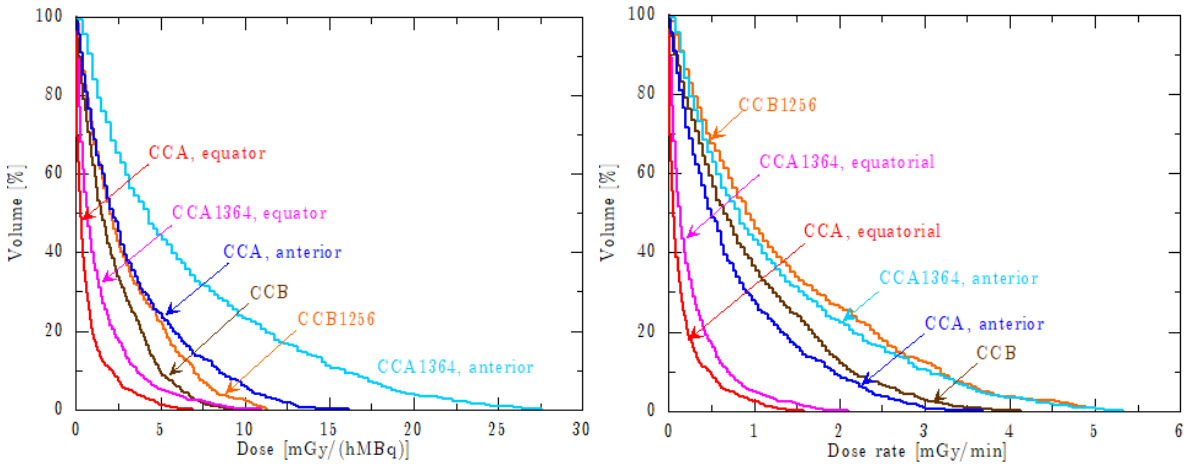

(A) Dose rate per unit of activity.

(B) Dose rate.

FIGURE 4.7: Dose-volume histograms for the cornea according to the different plaques and placements considered. The standard statistical uncertainty of the simulated data is smaller than the thickness of the lines.

Plot (A) in figure 4.7 shows that the maximum absorbed dose rate per unit of activity in the cornea corresponds to the CCA1364 plaque using an anterior placement which is 71% higher than the CCA using the same placement. In an equatorial placement, when using the CCB and CCB1256 the absorbed dose per unit of activity is 41% and 30% lower than the CCA with an anterior placement, respectively. The CCA equatorially placed yields the minimum absorbed dose rate per unit of activity in the cornea that is 75% lower than the same plaque with an anterior placement. For the equatorial placement of the CCA plaque, the absorbed dose per unit of activity is 37% lower than the CCA1364 equatorially placed. Notice that the absorbed dose per unit of activity for the CCA1364 with the equatorial placement and the CCB1256 *originally* rotated are almost the same. The difference between them amounts to 4% higher for the CCB1256.

Plot (B) shows that the maximum absorbed dose rate in the cornea corresponds to the CCA1364 with the anterior placement and the CCB1256 eye plaques. The difference between them is lower than 3%. The absorbed dose using the CCB plaque is 20% less than using the CCB1256. With the CCA plaque in an anterior placement the absorbed dose rate is 31% less than with the CCA1364 in the same placement. The lowest absorbed dose rate of 1.58 mGy min^{-1} is yielded for the CCA with the equatorial placement. For the CCA1364 in the same placement the absorbed dose rate is 33% higher.

Figure 4.8 shows the comparison of the absorbed dose at the cornea for the CCB and the CCB1256 plaque depending on the location of the hot spot. The *proximal* rotation is set when the hot spot is placed at the axial plane closer to the cornea while the *distal* placement is set when it is placed on the same plane but opposite to the cornea. For the CCB1256, that is the plaque in *original* rotation, the hot spot is located 138° away from the *proximal* orientation.

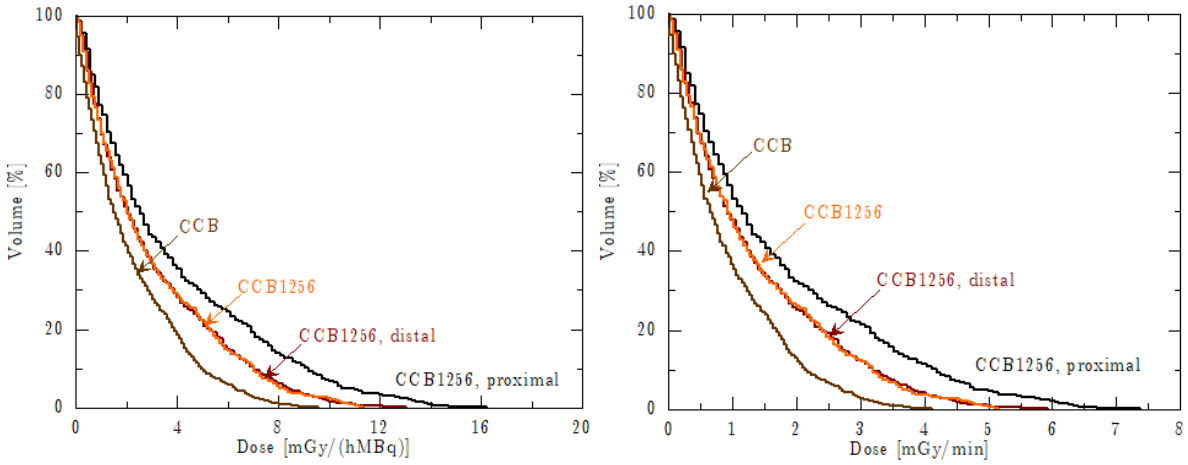

(A) Dose rate per unit of activity.

(B) Dose rate.

FIGURE 4.8: Dose-volume histograms for the cornea according to the CCB and CCB1256 plaques taking into account the hot spot location. The standard statistical uncertainty of the simulated data is smaller than the thickness of the lines.

Plot (A) in figure 4.8 shows that the maximum dose rate per unit of activity corresponds to the CCB1256 with the *proximal* rotation. For the CCB and the CCB1256 *originally* rotated, the absorbed dose per unit of activity is 44% and 30% lower, respectively. For the CCB1256 with the *distal* rotation the absorbed dose per unit of activity is 20% lower. Notice that the effect of the hot spot becomes evident when it is closer to the cornea, when it is placed at the *distal* location its presence behaves on average as the actual CCB1256 *originally* rotated. Plot (B) shows the dose rate for the CCB and the CCB1256 plaque with respect to the placement of the hot spot.

4.3.3 Eye lens

Figure 4.9 shows the absorbed dose in the eye lens for plaques in an anterior and equatorial placement. As it occurs with the cornea, the posterior location is not considered and the CCB1256 is studied only *originally* rotated.

Plot (A) in figure 4.9 shows that the maximum absorbed dose rate per unit of activity in the lens corresponds to the CCA1364 plaque with an anterior placement. The absorbed dose is 48% higher than the CCA in the same placement. When using the CCB and the CCB1256 plaques, the absorbed dose is 38% and 30% lower than the CCA in an anterior placement,

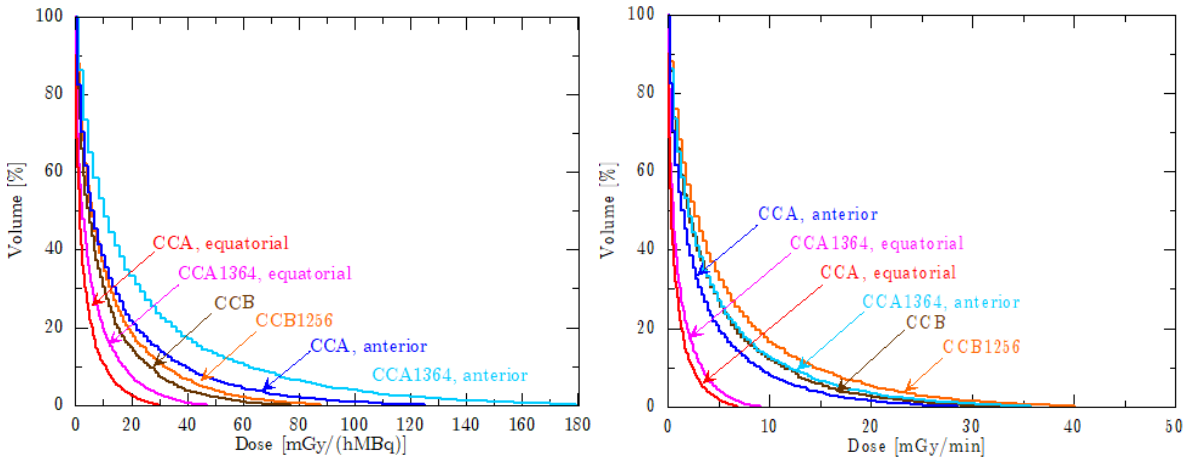

(A) Dose rate per unit of activity.

(B) Dose rate.

FIGURE 4.9: Dose-volume histograms for the eye lens according to the different plaques and placements considered. The standard statistical uncertainty of the simulated data is smaller than the thickness of the lines.

respectively. Notice that minimum absorbed dose rate per unit of activity corresponds to the CCA1364 in an equatorial placement.

Plot (B) shows that the maximum absorbed dose rate in the lens is given by the CCB1256 plaque *originally* rotated. Plots of the CCA1364 in an anterior placement and the CCB are similar. For the CCA in an anterior placement the absorbed dose is 29% lower than the CCB1256. The absorbed dose for the CCB is 17% less than the CCB1256. As expected, the equatorial placement for the CCA and the CCA1364 results in doses lower than that obtained with the CCB1256.

Figure 4.10 shows the comparison of the absorbed dose in the cornea for the CCB and the CCB1256 plaques depending on the location of the hot spot. The *proximal* rotation is set when the hot spot is placed at the axial plane closer to the lens while the *distal* rotation is set when it is placed at the axial plane but opposite to the lens. As it occurs with the cornea, the CCB1256, that is the plaque in *original* rotation, has the hot spot located 138° away from the *proximal* orientation.

Plot (A) in figure 4.10 shows that the maximum absorbed dose rate per unit of activity corresponds to the CCA1256 in the *proximal* rotation. With respect to the CCB1256 with a *distal* rotation and the CCB, the absorbed dose per unit of activity is 17% and 37% higher, respectively. As it happens with the cornea the effect of the hot spot is only observable when it is closer to the lens, when it is placed with the *distal* rotation its presence is not detected and the plaque behaves on average as the CCB1256 *originally* rotated. Plot (B) shows the absorbed dose rate for the CCB and the CCB1256 plaque with respect to the placement of the hot spot.

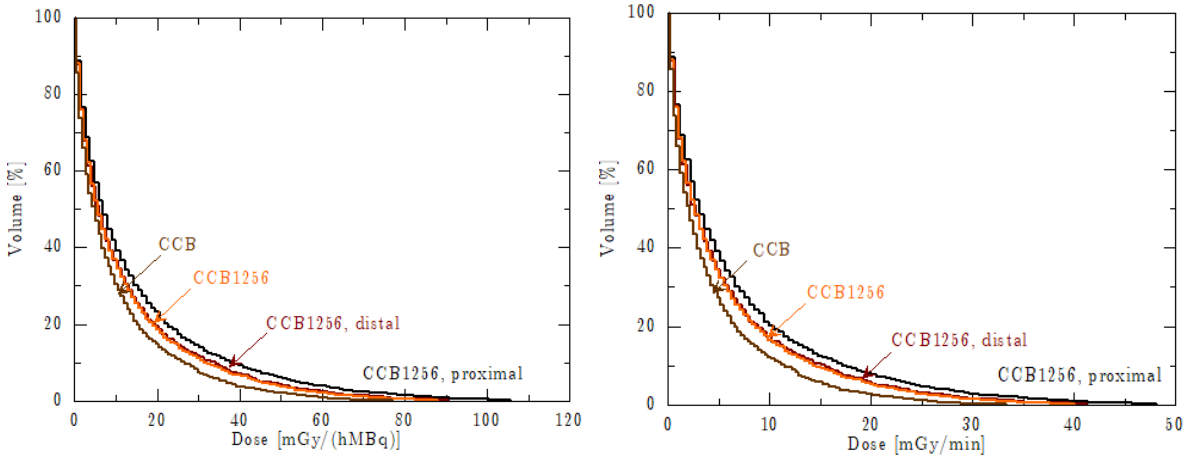

(A) CCA1364 eye plaque.

(B) CCB1256 eye plaque.

FIGURE 4.10: Comparison of the dose-volume histograms of the absorbed dose in the eye lens between the generic CCB plaque and CCB1256 plaque depending on the hot spot location. The standard statistical uncertainty of the simulated data is smaller than the thickness of the lines.

4.3.4 Papilla

Figure 4.11 shows the absorbed dose rate per unit of activity in the papilla only by the plaques in equatorial placement. The posterior placement of the plaques implies a 2.4 mm coverage of the papilla, thus, producing the highest absorbed dose rate. Posterior placements are compared in figure 4.12. Notice that for this segmented structure the anterior placement is not considered.

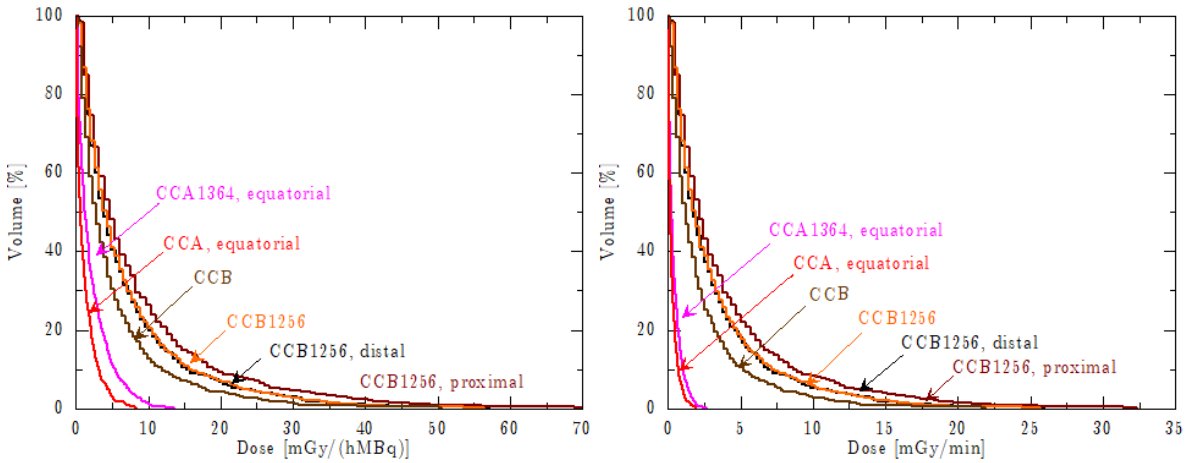

(A) Dose rate per unit of activity.

(B) Dose rate.

FIGURE 4.11: Dose-volume histograms for the papilla according to the different plaques and placements considered. The standard statistical uncertainty of the simulated data is smaller than the thickness of the lines.

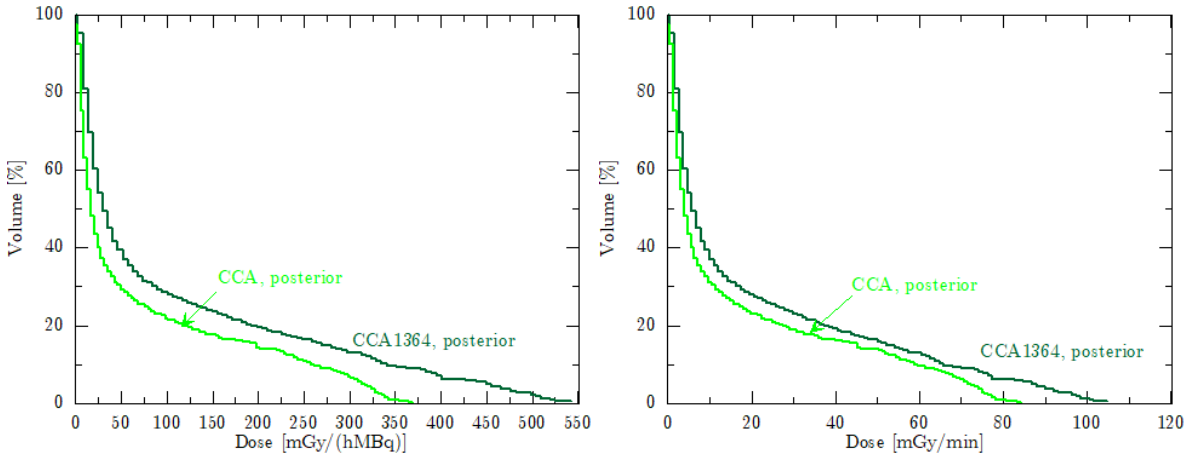

(A) Dose rate per unit of activity. (B) Dose rate.

FIGURE 4.12: Comparison of the dose-volume histograms of the absorbed dose in the papilla between the CCA and the CCA1364 plaques placed in a posterior location. The standard statistical uncertainty of the simulated data is smaller than the thickness of the lines.

Plot (A) in figure 4.11 shows that the maximum absorbed dose rate per unit of activity in the papilla corresponds to the actual CCB1256 plaque in the *proximal* placement, that is with the hot spot closer to the papilla. The absorbed dose per unit of activity is 41% higher than the CCB plaque. For the CCB1256 *originally* rotated, that is, with the hot spot located 42° away from the *proximal* rotation, the absorbed dose is 21% lower. For the CCB1256 with a *distal* rotation, the absorbed dose per unit of activity is 20% lower, too. As it happens with the cornea and the lens, the effect of the hot spot becomes evident with the plaque in the *proximal* rotation. It is also observed that the minimum absorbed dose rate per unit of activity is given by the CCA1364 and the CCA plaques. Plot (B) shows the absorbed dose rate in the papilla. As expected, the equatorial placement for the CCA1364 and CCA plaques results in absorbed doses lower than all other plaques and placements.

Figure 4.12 shows the comparison between the CCA and CCA1364 plaques in a posterior placement. Plot (A) shows that the maximum absorbed dose rate per unit of activity corresponds to the CCA1364 and it is 47% higher than the CCA plaque. Plot (B) shows that this difference is reduced to 25% in the absorbed dose rate.

4.3.5 Optic nerve

As it occurs with the papilla, the anterior placement for the optic nerve is not considered. Figure 4.13 only shows the comparison for plaques in an equatorial placement. The effect of the 2.4 mm of coverage for the posterior location is shown in figure 4.14.

Plot (A) in figure 4.13 shows that the maximum absorbed dose rate per unit of activity in the optic nerve corresponds to the CCB1256 plaque with a *proximal* rotation. The absorbed dose is 84% higher than for the CCB plaque. For the CCB1256 *originally* rotated, which has

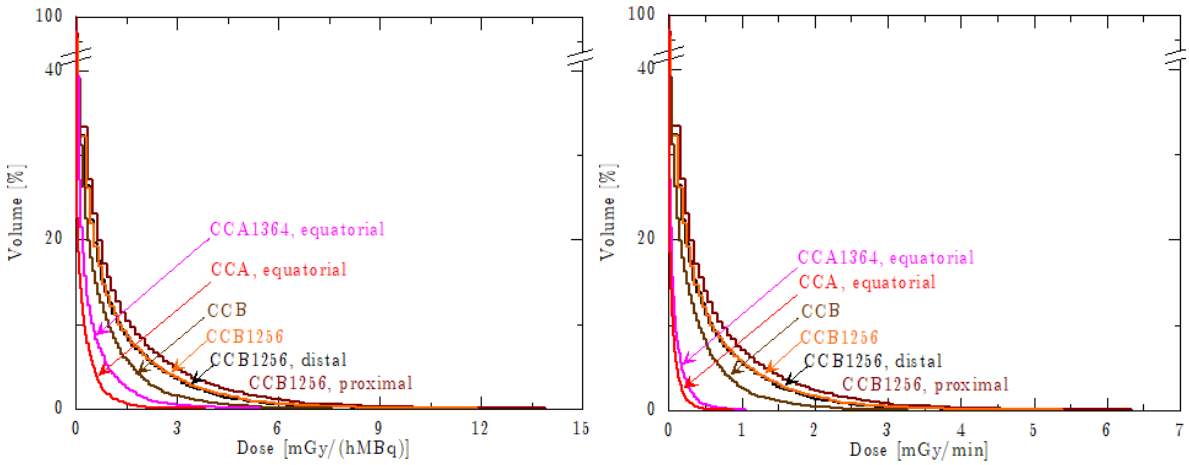

(A) Dose rate per unit of activity.

(B) Dose rate.

FIGURE 4.13: Dose-volume histograms for the optic nerve according to the different plaques and placements considered. The standard statistical uncertainty of the simulated data is smaller than the thickness of the lines.

the hot spot 42° away from the *proximal* orientation, the absorbed dose is 15% lower. For the CCB1256 with a *distal* rotation the absorbed dose is 18% lower, too. As it happens with the previous segmented structures the effect of the hot spot is only measurable with the *proximal* rotation of the plaque. It is also observed that for the CCA1364 and CCA plaques the minimum absorbed dose rate per unit of activity is given. Plot (B) shows the absorbed dose rate in the papilla. As expected, an equatorial placement of the CCA and CCA1364 results in an absorbed dose lower than that obtained with other placements.

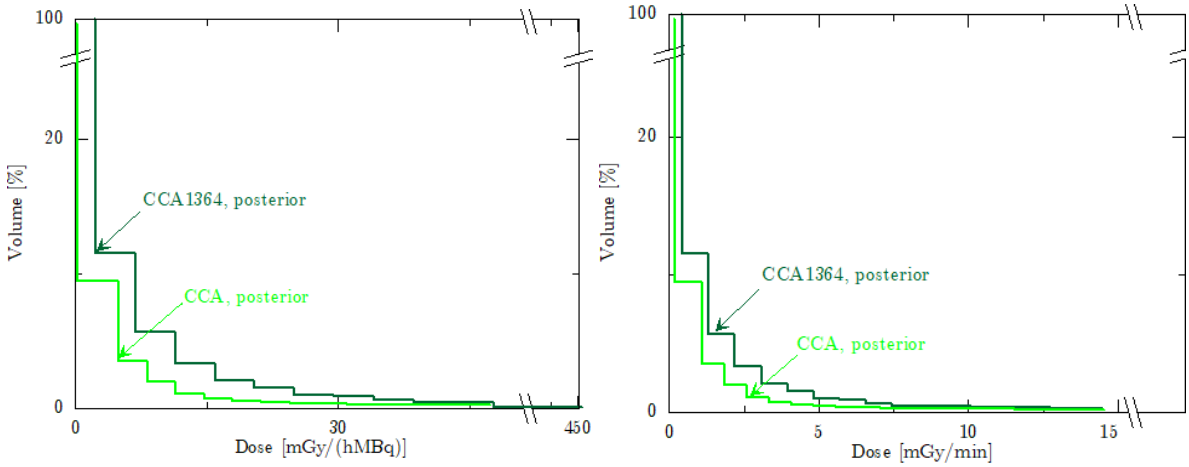

(A) Dose rate per unit of activity.

(B) Dose rate.

FIGURE 4.14: Comparison of the dose-volume histograms of the absorbed dose in the optic nerve between the CCA and the CCA1364 plaques with a posterior placement. The standard statistical uncertainty of the simulated data is smaller than the thickness of the lines.

Figure 4.14 shows the comparison between the CCA and CCA1364 in a posterior placement. It is observed that only a few voxels of the segmented structure receive a high dose as a consequence of its coverage. For the CCA plaque, only 2% of the voxels receive more than 10 mGy h^{-1} MBq^{-1} while for the CCA1364 the volume increases to 5% of the voxels.

4.3.6 Lachrymal gland

The lachrymal gland is the smallest anatomic structure segmented in the modeled eye. In addition, this is the furthest organ from all plaques and placements and consequently the gland receives the minimum absorbed dose for all simulations performed as shown in figure 4.15.

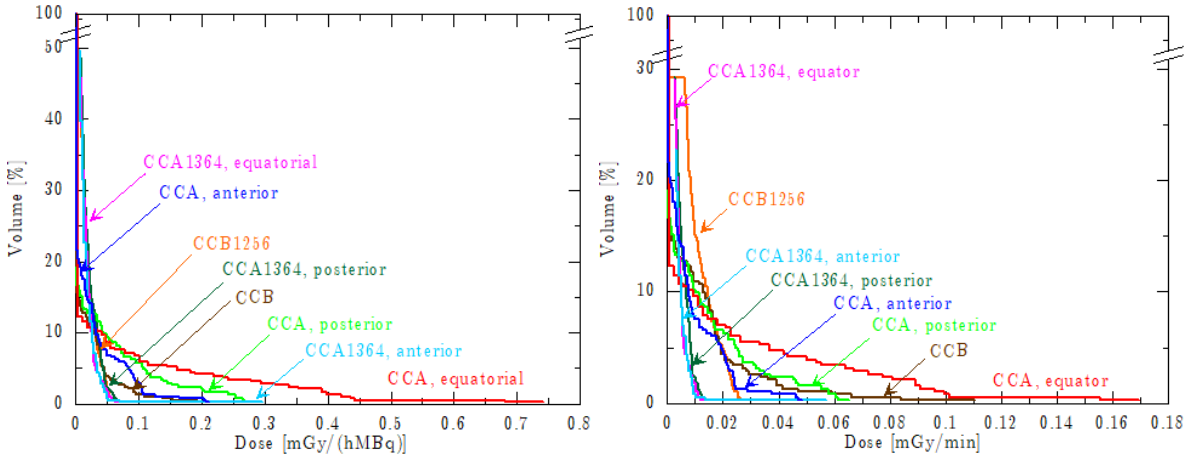

(A) Dose rate per unit of activity.

(B) Dose rate.

FIGURE 4.15: Comparison of the dose-volume histograms of the absorbed dose in the lachrymal gland for all plaques and placements. The standard statistical uncertainty of the simulated data is smaller than the thickness of the lines.

Plot (A) in figure 4.15 shows that the dose rate per unit of activity delivered to the gland ranges from 0.05 mGy h^{-1} MBq^{-1}, which corresponds to the CCB1256 plaque in an equatorial location, to 0.74 mGy h^{-1} MBq^{-1} that corresponds to the CCA plaque in the same location. Plot (B) in figure 4.15 shows that the dose rate ranges from 0.02 mGy min^{-1}, which corresponds to the CCA1364 in an equatorial placement, to 0.17 mGy min^{-1} which corresponds to the CCA plaque in the same location.

Chapter 5

Monte Carlo simulation of uveal melanoma treatments using the measured CCA1364 and CCB1256 eye plaques

5.1 Introduction

Radiotherapy and, in particular, brachytherapy are techniques used in the treatment of intraocular malignancies like uveal melanomas and retinoblastomas. Heterogeneities on the emission maps of the plaques result in differences on the dose delivered to the segmented structures of the eye as it has been shown in the previous chapter. The aim of this chapter is to determine the influence of these heterogeneities on the treatment of uveal melanomas. The treatment of idealized uveal tumors is simulated using a realistic description of two ^{106}Ru plaques, namely, CCA1364 and CCB1256 (see section 2.2.2), embedded in a computerized tomography scan of the eye (see figure 4.4). For all the tumors modeled, results are compared with those obtained from the CCA and CCB plaques. Comparisons are done using cumulative dose-volume histograms. Most of the content of this chapter was published by the author of this thesis and coauthors in the *Ocular Oncology and Pathology* journal (Brualla et al., 2014; Zaragoza et al., 2018).

5.2 Materials and methods

5.2.1 Voxelized geometry and eye segmentation

The voxelized geometry and the segmentation of the structures of the eye used in this chapter are the same as those used in section 4.2.1 and section 4.2.2, respectively.

5.2.2 Tumor modeling

Idealized tumors are modeled as independent target volume structures within the eye, allowing to tally the dose absorbed in them. In general, the prescription criteria for choosing a given ^{106}Ru plaque model is based on:

- The basal diameter of the tumor, which determines the plaque size.
- The apical height of the tumor, which determines the irradiation time.

Tumors are modeled with a constant basal diameter of 10.0 mm while varying the apical height. Tumors are mathematically segmented in the computerized tomography scan with a paraboloid truncated by a sphere representing the inner scleral surface. Notice that the height of the tumor does not include the thickness of the sclera. As with all mathematically segmented structures defined, the boundary surface divides voxels so that the tumor height lies within $\pm$ 0.5 mm of the defined value. The voxel criterion to determine if a voxel belongs or not to the target volume is the same used in section 4.2.2.

Tumors are positioned with their main symmetry axis coplanar to the axial plane of the computerized tomography where the diameter of the eye is maximum, which corresponds to the slice 21 in the computerized tomography. Three tumor positions are selected as follows:

- Equatorial; the symmetry axis of the tumors is along the eyeball equator. For this location, tumors of apical height of 3.0 mm, 5.0 mm, 6.5 mm, 7.0 mm and 7.5 mm are modeled.
- Anterior or pre-equatorial; the symmetry axis of the tumor is set 15° above the equator, which means 30° over the horizontal axis. For this location only a 3.0 mm apical height tumor is modeled.
- Posterior or post-equatorial; the symmetry axis of the tumor is set 45° below the equator, that is, 30° below the horizontal axis. For this location, only a 3.0 mm apical height tumor is modeled.

5.2.3 Placement of the plaques

To simulate the treatments of the considered tumor volumes the plaques are placed according to the tumor locations. Depending on the relative position between the symmetry axis of the tumors and the symmetry axis of the plaques a centered or eccentric placement is defined. A plaque is placed centrically when the symmetry axes of both, the tumor and the plaque, are coincident, whereas it is placed eccentrically if the contrary holds. Equatorial tumors are treated centrically with the CCA, CCA1364, CCB and CCB1256 plaques. Figure 5.1 shows an example of the treatment of tumors equatorially located. Plot (A) shows a CCA plaque model placed centrically with respect to the tumor of 3.0 mm of apical height while plot (B) shows a CCB plaque model also placed centrically but irradiating a tumor of 6.5 mm of apical height.

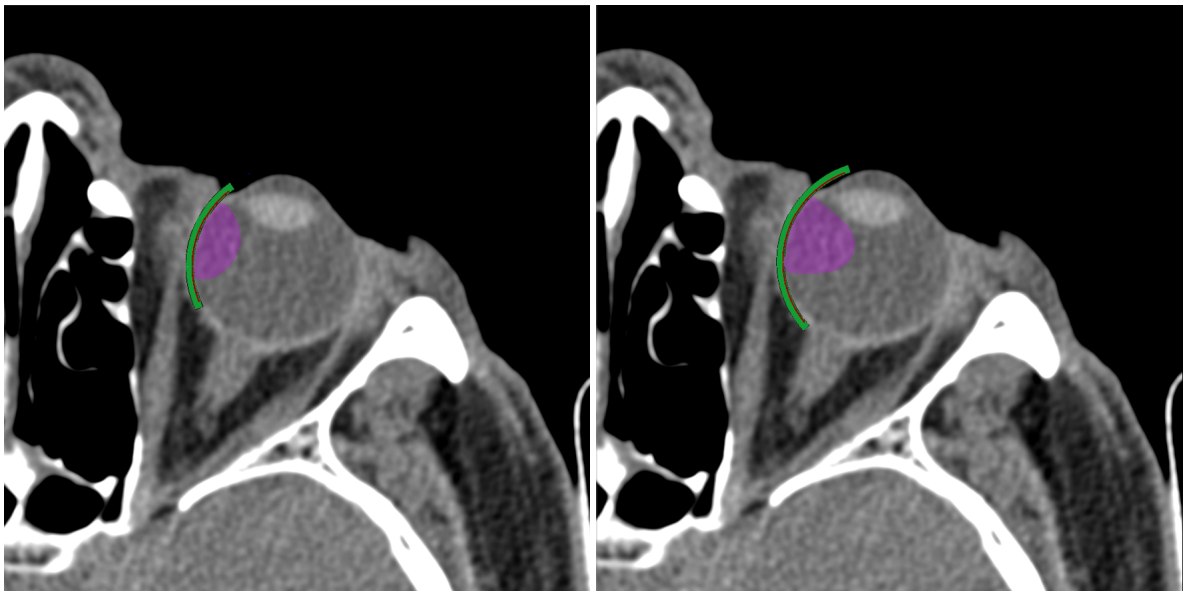

(A) Equatorial tumor of 3.0 mm of apical height treated with a CCA plaque placed centrically.

(B) Equatorial tumor of 6.5 mm of apical height treated with a CCB plaque placed centrically.

FIGURE 5.1: Axial images of the computerized tomography with modeled tumors in an equatorial location irradiated with ^{106}Ru plaques placed centrically with respect to the tumors.

Treatments for anterior tumors are simulated with the CCA plaque placed centrically, the CCA1364 placed both centrically and eccentrically and the CCB1256 placed eccentrically. For the CCA1364, when the eccentric placement is set, the border of the plaque is made tangent to the basal edge of the tumor at a point. Notice that for this placement the commonly used safety margin of 2 mm between the plaque and the basal edge of the tumor is not respected. In this case, the symmetry axis of the plaque is set 2° above the equator, which means 17° above the horizontal axis. Figure 5.2 shows the placement of CCA plaque models with respect to an anterior tumor. Plot (A) shows the CCA plaque with its axis of symmetry aligned with the axis of the tumor while in plot (B) the axes of symmetry are not aligned, which corresponds to an eccentric placement. The CCB and CCB1256 are placed eccentrically respect to the anterior tumor because they are placed equatorially. With this configuration these plaques cover the whole anterior tumor and the edge of the plaque overlaps the basal edge of the tumor by at most 2.8 mm.

For tumors located in a posterior placement all treatments are simulated with the plaques placed eccentrically. As it occurs with the anterior location, the treatment of the CCB and CCB1256 plaques is only simulated in an equatorial placement. In this case, the CCB and CCB1256 do not fully cover the whole posterior tumor. Their edge falls short of the basal edge of the tumor by at most 2.6 mm. For the CCA1364 plaque model two eccentric placements are considered. Plot (A) on figure 5.3 shows a first eccentric placement for the CCA and CCA1364 where the border of the plaque was made tangent to the basal edge of the tumor

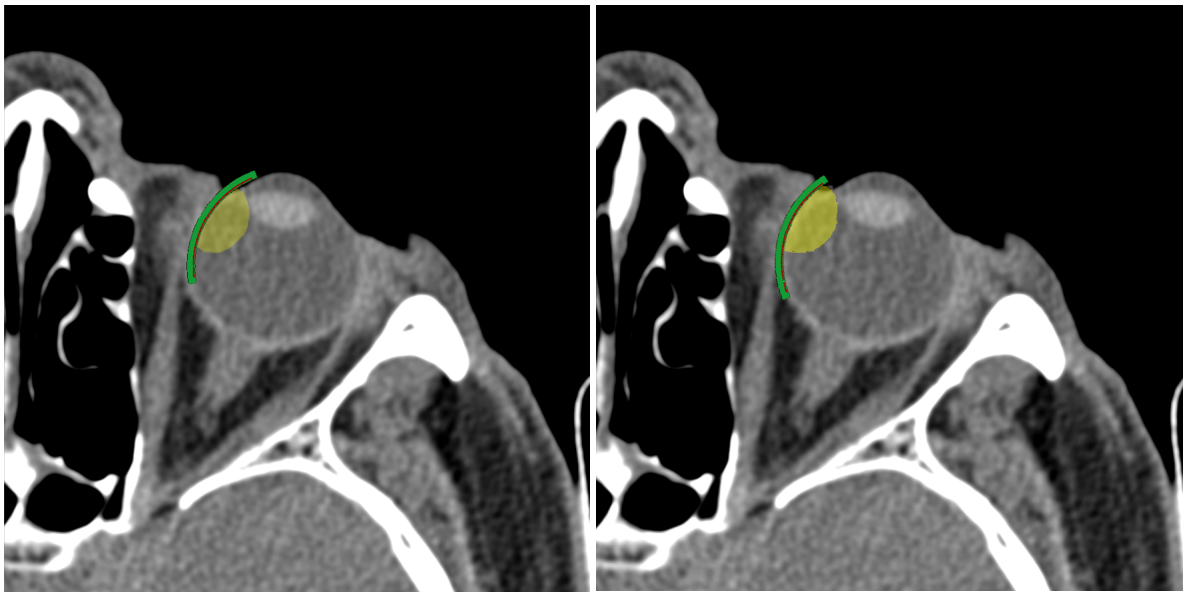

(A) Anterior tumor treated with a centered CCA plaque model.

(B) Anterior tumor treated with a CCA plaque model placed eccentrically.

FIGURE 5.2: Axial images of the computerized tomography with a modeled tumor in an anterior location treated with a CCA ^{106}Ru plaque.

at a point. Notice that this placement is anatomically difficult to attain owing to the presence of the optic nerve (see figure 5.3 (A)). In this case, the symmetry axis of the plaque is set 17° below the horizontal axis, which means 32° below the equator. Plot (B) on figure 5.3 shows a second eccentric placement that respects the presence of the optic nerve and it is considered anatomically feasible. The treatment corresponding to this placement is simulated only for the CCA1364 and corresponds to the *original* location for the CCA plaque (see section 4.2.3). Notice that for this treatment the plaque does not cover the whole basal surface of the tumor, it falls short of covering the basal surface of the tumor by a maximum distance of 0.3 mm. In this case, the symmetry axis of the plaque is set 15° below the horizontal axis, which means 30° below the equatorial plane.

5.2.4 Orientation of the plaques

Rotations around the symmetry axis of the plaques allow to take advantage of the heterogeneities in the treatment of the tumors. Three rotations, *original*, *proximal* and *distal*, are simulated with respect to the tumor location.

For the CCB1256 irradiating anterior or posterior tumors, these rotations take the location of the hot spot as reference (see figure 3.1 (B)). As it occurs in the previous chapter 4, the *original* rotation locates the hot spot 42° below the axial plane where the eye globe shows its maximum diameter, which corresponds to the slice 21 in the computerized tomography. The *proximal* rotation is set when the hot spot is closer to the tumor while the *distal* occurs in the

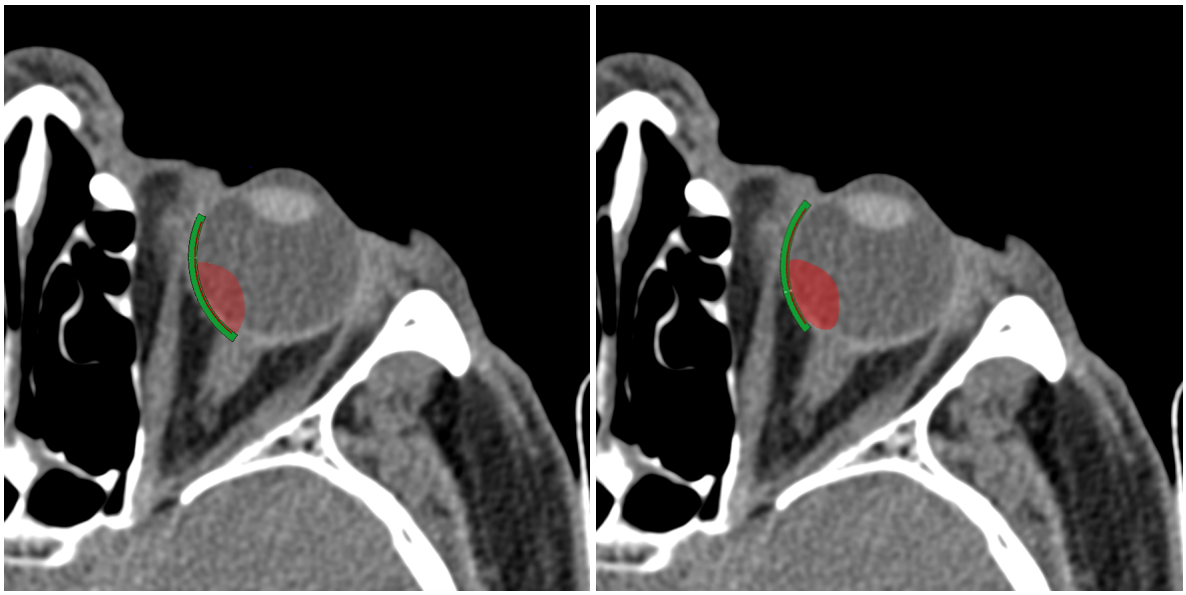

(A) Posterior tumor treated with a CCA plaque tangent to the basal edge of the tumor.

(B) Posterior tumor treated with a CCA plaque placed in an anatomically feasible location.

FIGURE 5.3: Axial images of the computerized tomography with a modeled tumor in a posterior location treated with a CCA ^{106}Ru plaque placed eccentrically.

opposite case. As occurs in chapter 4, the polar bin of the hot spot with the largest activity is placed in the axial plane.

For the CCA1364 placed eccentrically, that is when it is used for irradiating anterior or posterior tumors, the direction along the maximum asymmetry on the off-centered distribution of the emitter, which is 18° with respect to the positive horizontal axis, is taken as reference (see section 3.2.1). The *proximal* rotation is set when the asymmetry covers better the anterior or posterior basal line of the tumors while the *distal* rotation occurs in the opposite case. For equatorial tumors these rotations are not considered.

5.2.5 Prescription method

The prescription method determines the irradiation time that a specific point on a segmented volume needs to absorb a given dose. Therefore, determining the point where the dose should be computed is essential to allow comparisons between the treatments (Stöckel et al., 2018). The points considered to determine the irradiation time are at the sclera and the tumor apex. At the apex, the absorbed dose is obtained from the voxel belonging to the tumor volume further from the plaque along its symmetry axis. For the sclera, the absorbed dose was initially obtained from the closest voxel to the plaque along the symmetry axis of it. Considering that the scleral thickness is not constant (see section 4.2.2) and that the dose delivered to it depends on the heterogeneities of the plaque (see section 3.1), irradiation times can significantly vary depending on the placement of a given plaque. For this reason, to determine the

irradiation time at the sclera the chosen value corresponds to the absorbed dose simulated at a depth of 2.0 mm along the symmetry axis for the heterogeneous plaques. At this distance variations on the irradiation time are smaller and do not affect the outcome of the prescription procedure described below. The irradiation time obtained with this method is used for the corresponding homogeneous plaques. Notice that when the placement of the plaques is eccentric, these points are not located on the same axis of symmetry. The process to determine the dose prescription is the following:

- To determine the time needed to reach 700 Gy at the sclera using the activities of the plaques. The time determined for the CCA1364 plaque is 133 h and 94 h for the CCB1256 plaque.
- For this time, check if the dose delivered at the apex of the tumor is greater than 100 Gy. Then the treatment is performed.
- If not, the initial time is extended until the dose delivered to the apex reaches 100 Gy.
- For this new time, if the dose at the sclera exceeds 1500 Gy the brachytherapy treatment with this plaque is discarded.

The value of 100 Gy for the absorbed dose at the apex is a compromise between the commonly prescribed doses at many hospitals, which range between 80 Gy and 100 Gy, and that prescribed at the Universitätsklinikum Essen that corresponds to 130 Gy.

5.2.6 Geometry of the simulation

Apart from the geometries exposed on section 2.2.4 two more geometries corresponding to the CCA1364 plaque are needed to simulate the treatments. One of them places the plaque eccentrically with respect to the anterior tumor while the other places the plaque also eccentrically but in a feasible location for tumors in a posterior location (see section 5.2.3).

5.2.7 Transport parameters

There are no changes with respect to the previous chapter. The transport parameters used in section 4.2.5 and the values of the activities given by table 4.3 are the same.

5.3 Results and discussion

Comparisons of the absorbed dose in the tumor volumes and the structures-at-risk considered are made using cumulative dose-volume histograms of the absolute absorbed dose.

5.3.1 Anterior tumor

The anterior tumor treatment is simulated centrically when using the CCA and CCA1364 eye plaques and eccentrically when using the CCA1364 (see figure 5.2 (B)), and the CCB1256 plaques. Isodose lines for an anterior tumor irradiated centrically using the CCA1364 plaque is shown on figure 5.4 (A) while figure 5.4 (B) shows isodose lines for the same tumor but eccentrically irradiated.

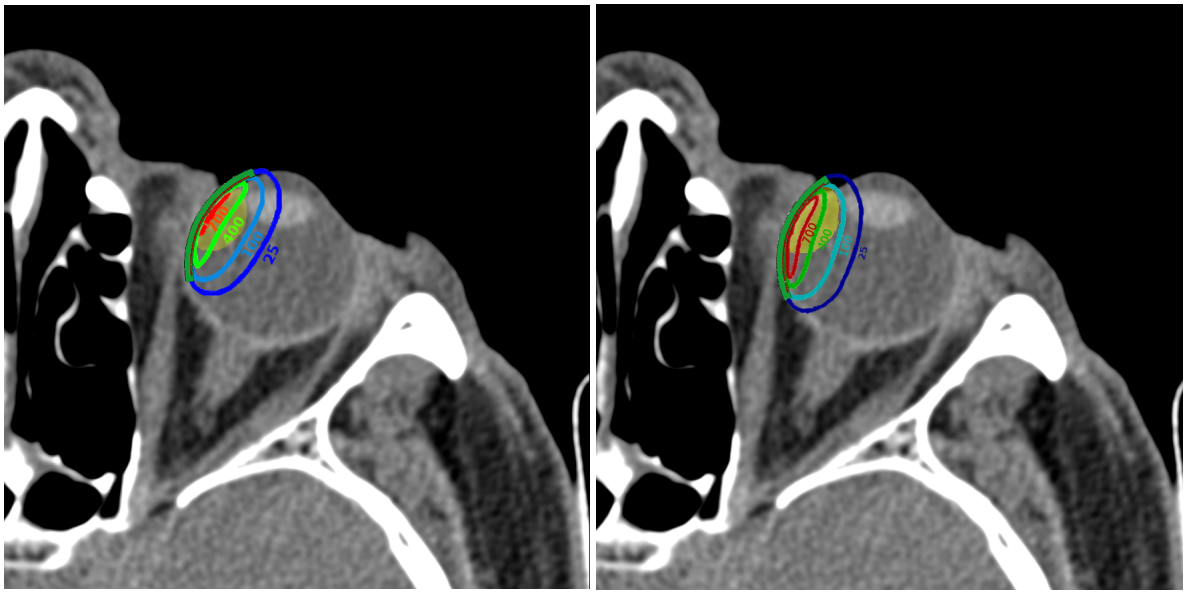

(A) Tumor irradiated centrically with the CCA1364 plaque.

(B) Tumor irradiated eccentrically with the CCA1364 plaque with a *proximal* rotation.

FIGURE 5.4: Isodose lines corresponding to axial images of the computerized tomography with a tumor of 3.0 mm of apical height in an anterior location irradiated with the CCA1364 plaque placed centrically and eccentrically considering an irradiation time of 133 h. The tumor volume is shown in yellowish color wash. Numbers next to the isodose lines show the dose in Gy. The average standard statistical uncertainty for the simulations is lower than 0.5%.

Table 5.1 shows the absolute absorbed dose at the tumor apex and the maximum dose absorbed in the lens volume according to the plaque model, CCA, CCA1364 or CCB1256, the relative placement between the axis of symmetry of the plaque respect to the axis of symmetry of the tumor, centered or eccentric, and rotations around the axis of symmetry of the plaques, *proximal* or *distal*. For a centered treatment, the maximum absorbed dose in the tumor is yielded when using the CCA1364 plaque. For this plaque and placement the maximum dose in the lens volume is also achieved. The absorbed dose at the apex is 28% lower while the maximum dose in the lens is reduced by 22% when using the CCA. For the CCB1256 with a *proximal* rotation, the absorbed dose at the apex is only 1 Gy higher than using the centered CCA1364 while reducing 7% the maximum dose in the lens. When using the CCB1256 with a *distal* rotation, the absorbed dose at the apex is 3.6 Gy lower than using the CCA1264 while reducing 20% the absorbed dose in the lens. When simulating with the CCA1364 with a

proximal rotation, the absorbed dose at the apex is 23% lower than the one reached with the CCA1364 while it reduces 69% the maximum dose at the lens volume. When the CCA1364 plaque is simulated with a *distal* rotation the dose absorbed at the apex and the maximum dose at the lens are the lowest. The dose at the apex is reduced 39% while the maximum dose in the lens is reduced 73%.

TABLE 5.1: Dose delivered at the tumor apex and maximum absorbed dose in the lens volume.

Model	Rotation	Placement	Apex (Gy)	Lens (Gy)
CCA		centered	174	228
CCA1364	*original*	centered	243	292
CCA1364	*proximal*	eccentric	188	91
CCA1364	*distal*	eccentric	147	77
CCB1256	*proximal*	eccentric	244	271
CCB1256	*distal*	eccentric	239	232

Figure 5.5 (A) shows the dose-volume histograms for the anterior tumor volume corresponding to all simulated treatments. Notice in this figure that the chosen criterion to determine the irradiation time causes that the histograms do not intersect the abscissas axis at the 700 Gy point but in its proximity. The lens is the closest segmented structure at risk so determining the absorbed dose on it is also taken into account to determine the suitability of the treatment. Figure 5.4 (B) shows the dose-volume histograms for the lens volume corresponding to the same simulated treatments.

For anterior tumors of 3.0 mm of apical height simulations show that the treatment performed with the CCA1364 plaque placed eccentrically, that is, without respecting the 2 mm safety margin, is the most suitable treatment among those considered. For all the rotations, *proximal* and *distal*, the required absorbed dose at the apex is yielded while minimizing the dose to the lens. An important result is that for the CCB1256 plaque, which is always in an eccentric placement for anterior tumors, a smaller absorbed dose to the lens than the centered CCA1364 plaque is achieved. With respect to the CCA plaque, simulations using an homogeneous distribution of the radioactive substance results in an overdose of all the segmented volumes.

5.3.2 Equatorial tumors

Equatorial tumors are always treated with centered plaques (see section 5.2.3) since this placement is always possible and the safety margin of 2 mm of the basal line of the tumor is always guaranteed. Figure 5.6 (A) shows isodose lines for an equatorial tumor of 3.0 mm of apical

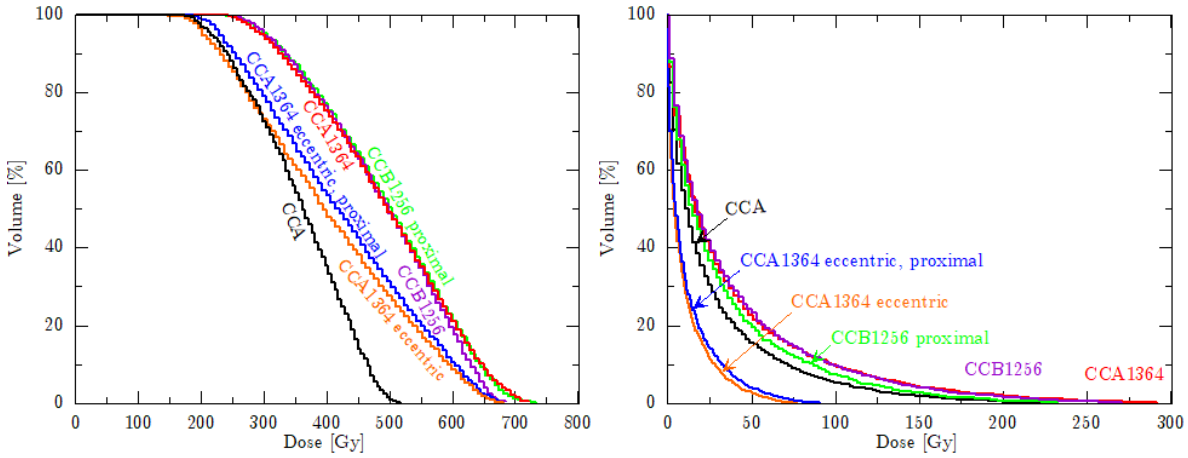

(A) Dose-volume histograms corresponding to a generic anterior tumor of 3.0 mm.

(B) Dose-volume histograms corresponding to the eye lens.

FIGURE 5.5: Comparison of the dose delivered to an anterior tumor. Black line corresponds to the CCA plaque placed centrically, red line corresponds to the CCA1364 placed also centrically, blue line corresponds to the CCA1364 placed eccentrically but in a *proximal* rotation, orange line corresponds to the CCA1364 placed eccentrically but in the *distal* rotation, purple line corresponds to the CCB1256 placed eccentrically and green line corresponds to the CCB1256 placed eccentrically but with the hot spot closer to the tumor. All plots are in histograms. The standard statistical uncertainty of the simulated data is smaller than the thickness of the lines.

height treated with the CCA1364 plaque. Figure 5.6 (B) shows isodose lines for an equatorial tumor of 6.5 mm of apical height, which is the highest tumor simulated, treated with the CCB1256 plaque.

Table 5.2 shows the dose delivered to the tumor apex and the sclera for all simulated equatorial tumors. For the smallest tumor of 3.0 mm of apical height all plaques yield the required minimum dose of 100 Gy at the tumor apex. It is observed that the maximum absorbed dose is yielded with the CCB1256 plaque. With the CCA1364 the absorbed dose is 7% lower while with the homogeneous CCA and CCB the absorbed dose is 34% and 54% lower, respectively. With respect to medium tumors of 5.0 mm of apical height, it is observed on table 5.2 that only the treatment delivered with CCB1256 yields the minimum dose at the apex for the prescription dose of 700 Gy at the sclera. When using the CCA, CCA1364 and CCB plaques, the irradiation time has to be extended to achieve the 100 Gy at the apex. Figure 5.7 shows dose-volume histograms for low and medium tumors of 3.0 mm and 5.0 mm of apical height centrically treated, respectively.

Figure 5.8 (A) shows the dose-volume histograms corresponding to the largest equatorial tumors of 6.5 mm, 7.0 mm and 7.5 mm of apical height when the prescription time is computed assuming 100 Gy at the apex. Due to their location, the absorbed dose in the lens and the optic disk are also calculated to allow comparison between treatments. Dose-volume histograms corresponding to the lens and the optic disk are plotted in figure 5.8 (B).

Table 5.2 shows that tumors of 6.5 mm can be treated with the CCA1364 and the CCB1256

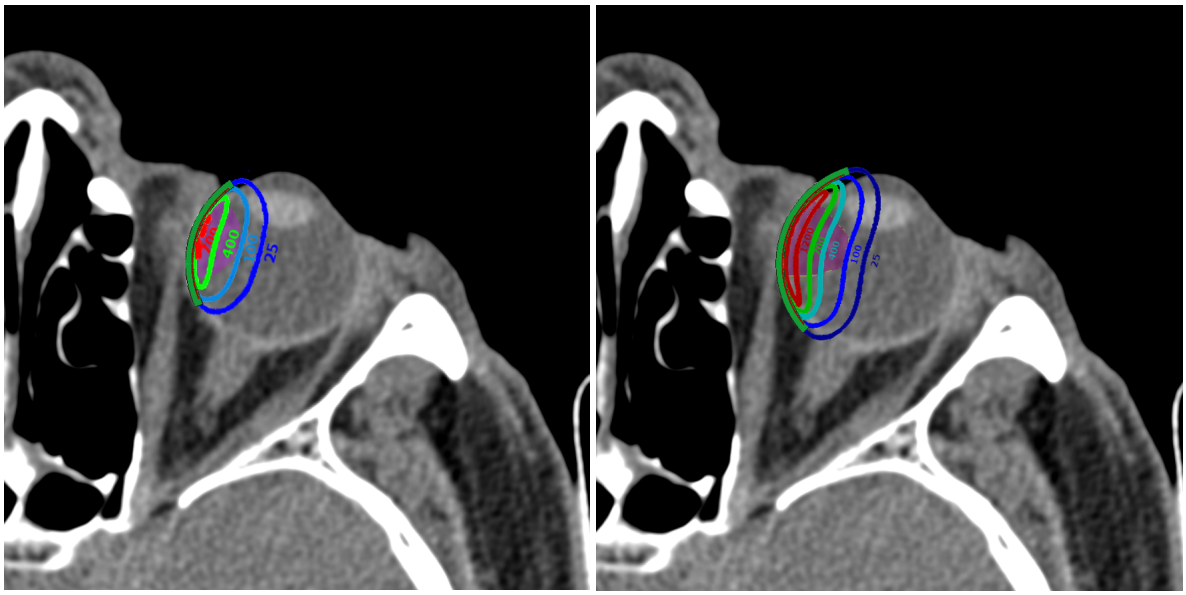

(A) Tumor of 3.0 mm of apical height equatorially located treated with the CCA1364 plaque.

(B) Tumor of 6.5 mm of apical height equatorially located irradiated with the CCB1256.

FIGURE 5.6: Isodose lines corresponding to axial images of the computerized tomography of a tumors equatorially located. Plot (A) considers an irradiation time of 133 h that correspond to 700 Gy at the sclera. Plot (B) considers an irradiation time of 167 h that correspond to 100 Gy at the apex for the tumor of 6.5 mm of height. Tumor volume is shown in purplish color wash. Numbers next to the isodose lines show the dose in Gy. The average standard statistical uncertainty for the simulations is lower than 0.5%.

TABLE 5.2: Dose delivered at the tumor apex and the sclera according to the tumor height and plaque model depending on the irradiation time.

Tumor height (mm)	Irradiation time (h)	Model	Apex (Gy)	Sclera (Gy)
3.0	133	CCA	157	496
		CCA1364	222	700
	94	CCB	110	347
		CCB1256	237	685
5.0	133	CCA	57	496
		CCA1364	88	700
	94	CCB	51	347
		CCB1256	114	685
6.5	281	CCA1364	100	1480
	167	CCB1256	100	1182
7.0	236	CCB1256	100	1673
7.5	272	CCB1256	100	1921

plaques since the absorbed dose at the sclera does not exceed the maximum value of 1500 Gy (see section 5.2.5). For the CCA1364 the prescription time is 68% higher than the time needed for the CCB1256 but the absorbed dose at the lens and the optic disk is reduced 62% and 83%, respectively. The tumor of 7.0 mm exceeds 12% the reference value of 1500 Gy at the sclera while the tumor of 7.5 mm of height exceeds 28% this value (see section 5.2.5). For the optic disk and the lens, tumors of 7.0 mm and 7.5 mm absorb 42% and 63% more dose than the dose absorbed by the 6.0 mm tumor treated with the CCB1256, respectively.

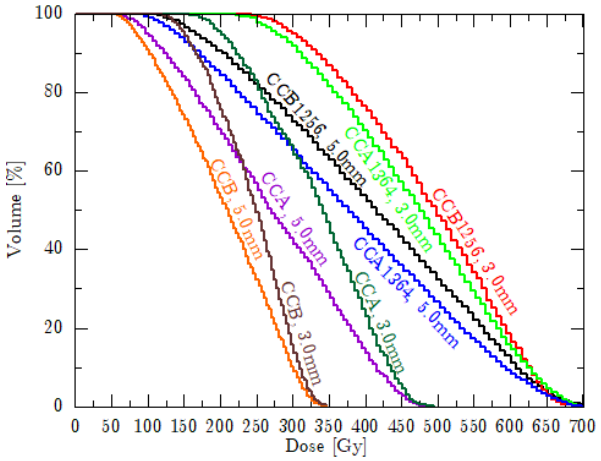

FIGURE 5.7: Dose-volume histograms corresponding to a low and medium equatorial tumors of 3.0 mm and 5.0 mm of apical height respectively. Tumor of 3.0 mm is treated by the CCA (forest green line), the CCA1364 (green line), the CCB (dark brown line) and the CCB1256 (red line). Tumor of 5.0 mm is treated by the CCA (purple line), the CCA1364 (blue line), the CCB (orange line) and the CCB1256 (black line). The standard statistical uncertainty of the simulated data is smaller than the thickness of the lines.

Treatment simulations show that equatorial tumors up to 6.5 mm can be treated with both, the CCA1364 and the CCB1256 plaques. Although the prescription time for tumors of 6.5 mm treated by CCA1364 is larger than obtained with CCB1256, the absorbed dose in the eye lens and the optic disk is lower when the CCA1364 plaque is used. As it happens with the anterior tumor, treatments simulated with the generic homogeneous CCA and CCB plaques result in an increase of the prescription time producing an overdose on the segmented volumes.

5.3.3 Posterior tumor

Treatments for tumors in a posterior location are always simulated eccentrically when using the CCA and CCA1364 plaque models owing to the location of the tumor next to the optic disk and the optic nerve. Figure 5.9 (A) shows isodose lines for the posterior tumor irradiated eccentrically by the CCA1364 plaque. Figure 5.9 (B) shows isodose lines for the posterior tumor also irradiated eccentrically by the CCB1256 plaque in an equatorial placement. Notice in figure 5.9 (B) that, although the absorbed dose in the apex is 100 Gy, which is recommended in

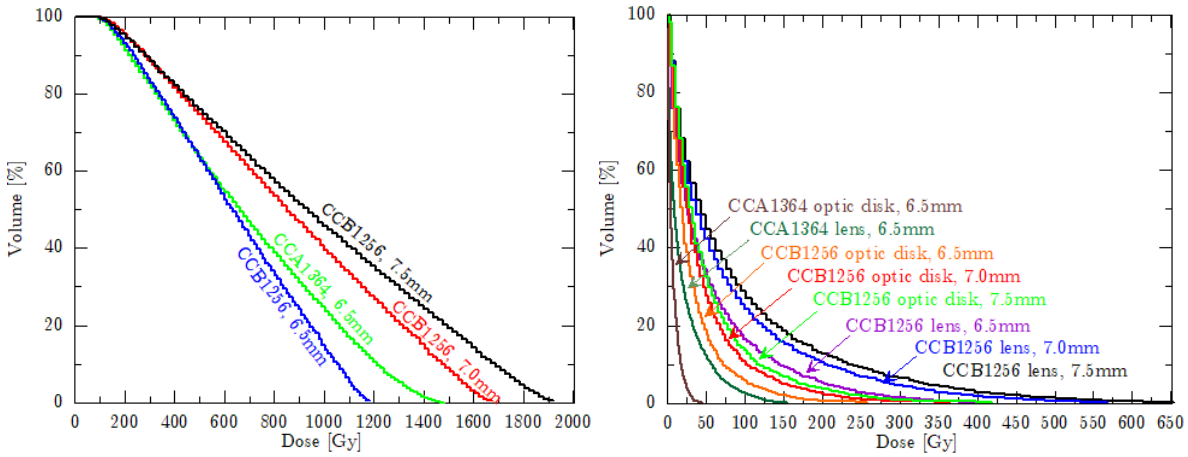

(A) Dose-volume histograms corresponding to equatorial tumors higher than 5.0 mm of apical height.

(B) Dose-volume histograms corresponding to optic disk and lens for tumors higher than 5.0 mm of apical height.

FIGURE 5.8: Comparison of the dose delivered to equatorial tumors higher than 5.0 mm of apical height.

the prescription method (see section 5.2.5), there are regions of the tumor volume that absorb a lower dose.

Table 5.3 shows the absorbed dose at the tumor apex and the maximum absorbed dose in the optic disk. For the CCA1364 eye plaque, the placement of the plaques, feasible or unfeasible, and rotations around the symmetry axis, *proximal* or *distal*, are considered. The CCA plaque is only simulated for an unfeasible placement. For these plaques, an irradiation time of 133 h, which was determined for tumors of 3.0 mm of apical height, is considered (see section 5.2.5). For the CCB1256 eye plaque, rotations around its symmetry axis, *proximal* or *distal*, are also considered. For this plaque, an irradiation time of 167 h, which corresponds to the irradiation time needed to treat a tumor of 6.5 mm in an equatorial location without exceeding the maximum absorbed dose in the sclera, is used. The maximum absorbed dose at the apex of 160 Gy is yielded for the CCA1364 with a *proximal* rotation but in an unfeasible placement. For this plaque and placement, the absorbed dose at the optic disk reaches the unacceptable value of 1912 Gy, therefore, the treatment is not feasible. When the CCA1364 in this unacceptable placement is rotated to a *distal* orientation the absorbed dose at the apex decreases 1% while the maximum absorbed dose in the optic disk also decreases 15%. Although the reduction on the absorb doses the values are still unacceptable. When the CCA1364 is feasibly placed and set with the *proximal* rotation, the absorbed dose at the apex is only 14% lower while the maximum dose in the disk decreases 50%. When it is set with a *distal* rotation, the absorbed dose in the apex is reduced 17% and the absorbed dose at the optic disk decreases 55%. For the homogeneous CCA plaque, the absorbed dose in the apex and the optic disk are 27% and 65% lower than the CCA1364 with a *proximal* rotation and unfeasibly placed, respectively. Simulation with the CCB1256 with a *proximal* rotation reduces the absorbed dose in the apex by

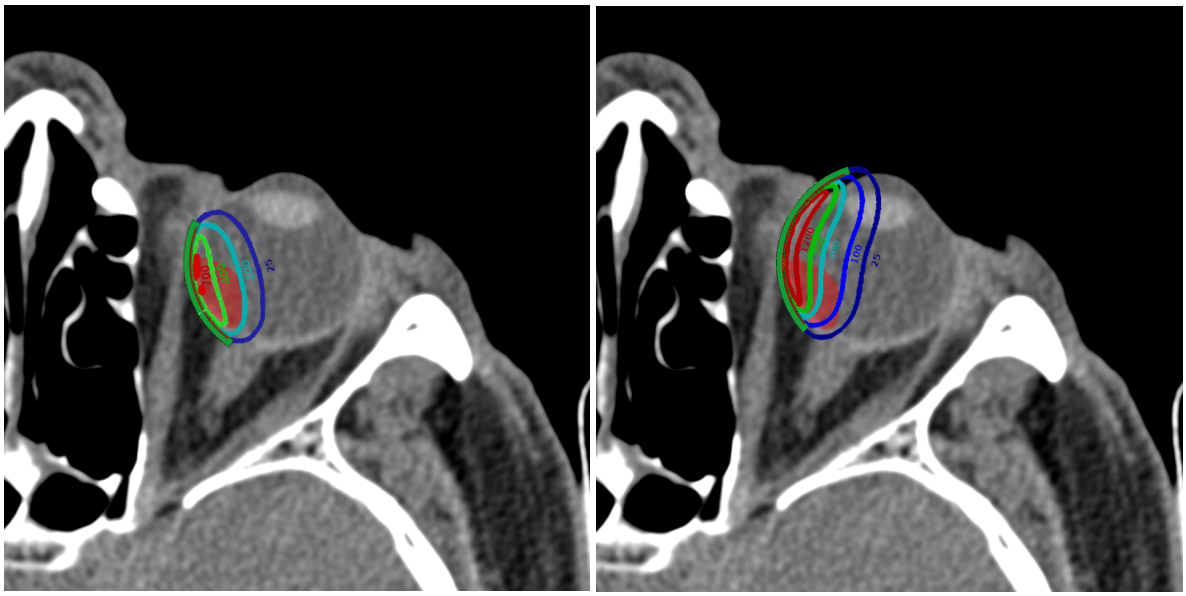

(A) Tumor irradiated eccentrically by the CCA1364 plaque placed tangent to the basal line of the tumor in a *proximal* rotation.

(B) Tumor irradiated eccentrically by the CCB1256 plaque in a *proximal* rotation without respecting the safety margin of 2 mm at the base of the tumor.

FIGURE 5.9: Isodose lines corresponding to axial images of the computerized tomography with a tumor of 3 mm of apical height in an posterior location. Plot (A) considers an irradiation time of 133 h that correspond to 700 Gy at the sclera. Plot (B) considers an irradiation time of 167 h that correspond to 100 Gy at the apex of the tumor of 6.5 mm of height equatorially placed. Tumor volume is shown in reddish color wash. Numbers next to the isodose lines show the dose in Gy. The average standard statistical uncertainty for the simulations is lower than 0.5%.

50% and also reduces the absorbed dose in the optic disk by 83% with respect to the CCA1364 unfeasibly placed. A treatment simulated with the CCB1256 with a *distal* rotation reduces the absorbed dose at the apex by 55% and in the disk by 86% with respect to the CCA1364 unfeasibly placed.

Figure 5.10 (A) shows the dose-volume histograms computed for the tumor volume. As it occurs with the anterior tumor, the histograms do not intersect the abscissa axis at the 700 Gy point due to the criteria for determining the irradiation time. For this tumor, the structure at risk taken into account to determine the suitability of the treatment is the optic disk. Figure 5.10 (B) shows the dose-volume histograms for the optic disk. Although the irradiation time guarantees 100 Gy at the apex of the tumor, dose-volume histograms corresponding to the CCB1256 in *proximal* and *distal* placement show that 100% of the tumor volume absorbs 80 Gy and 72 Gy, respectively.

Simulations of posterior tumors of 3.0 mm of apical height show that all treatments performed by the CCA1364 plaque regardless the placement, feasible or unfeasible, or rotation, *proximal* or *distal*, succeed absorbing more than 100 Gy at the tumor apex. This also happens

TABLE 5.3: Dose delivered at the tumor apex and maximum absorbed dose in the optic disk.

Model	Rotation	Placement	Apex (Gy)	Optic disk (Gy)
CCA		unfeasible	117	671
CCA1364	*proximal*	unfeasible	160	1912
CCA1364	*distal*	unfeasible	158	1634
CCA1364	*proximal*	feasible	137	955
CCA1364	*distal*	feasible	133	858
CCB1256	*proximal*	feasible	80	323
CCB1256	*distal*	feasible	72	260

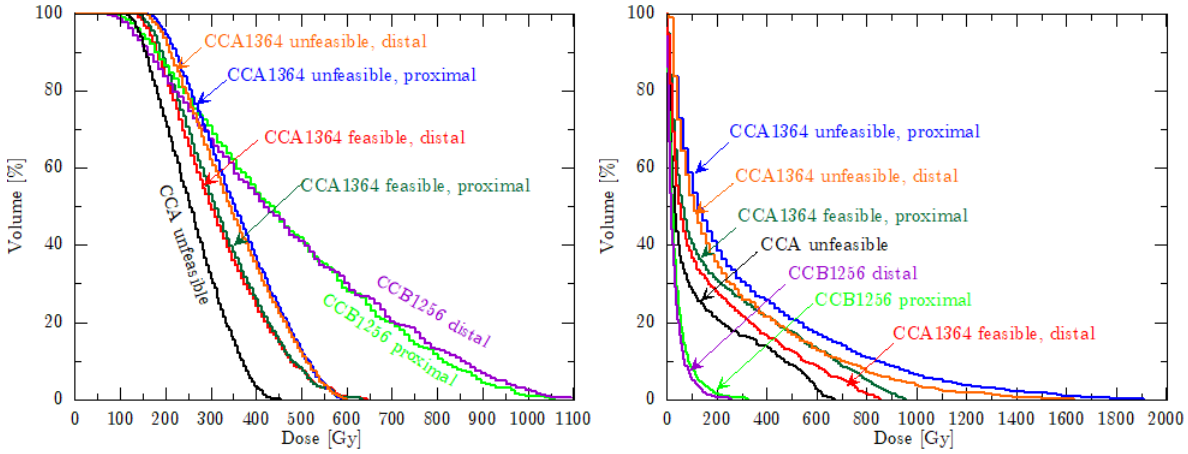

(A) Dose-volume histograms corresponding to a posterior tumor of 3.0 mm of apical height.

(B) Dose-volume histograms corresponding to the optic disk.

FIGURE 5.10: Comparison of the dose absorbed in a posterior tumor. Black line corresponds to the CCA plaque, red line corresponds to the CCA1364 placed in a feasible location and *distal* rotation, green line corresponds to the CCA1364 placed in a feasible location but with *proximal* rotation, orange line corresponds to the CCA1364 placed in an unfeasible and with *distal* rotation, blue line corresponds to the CCA1364 place in an unfeasible location but with *proximal* rotation, purple line corresponds to the CCB1256 with *distal* rotation and green line corresponds to the CCB1256 with *proximal* rotation. All plots are in histograms. The standard statistical uncertainty of the simulated data is smaller than the thickness of the lines.

with the CCB1256 plaque in a *proximal* or *distal* location although the treatment does not guarantee a minimum value of 100 Gy for all the tumor volume. The most suitable simulated treatment is obtained for the CCA1364 feasible placed regardless all rotations since yields the required absorbed dose at the apex while minimizing the maximum dose at the optic disk. Simulations with the CCA plaque also result in an overdose of all segmented volumes as it happens with the same plaque when it is used for anterior and equatorial tumors.

Chapter 6

Discussion

In previous chapters, discussions and conclusions on the specific issues for each chapter were presented. This chapter presents a discussion on the limitations of the research, the possible influence of the results on the clinical practice of uveal melanoma treatment using brachytherapy with $^{106}Ru/^{106}Rh$ eye plaques, and suggestions for future research.

6.1 Limitations

In this thesis Monte Carlo simulations on eye plaques showing homogeneous and heterogeneous emitter maps have been performed in water and anthropomorphic phantoms. The study presented in chapter 2 validates the proposed geometrical model of the eye plaques by comparison with the experimental data provided by the plaque manufacturer, as well as, experimental data published by researchers (Taccini et al., 1997; Kaulich et al., 2005). For the actual CCA1364 and CCB1256, the features on the depth dose along their symmetry axes as well as on their lateral profiles due to the heterogeneous distribution of the emitter substance were studied in chapter 3. For both plaques, isodose lines were computed. The results were also compared with the experimental data. In chapter 4 the absorbed dose in the anatomical structures of the eye were presented taking into consideration the orientation and placement of the plaques. Finally, in chapter 5 treatments for idealized tumors were simulated for the referred plaques.

The main limitation of the work presented herein comes from the reduced number of eye plaque models analyzed (CCA and CCB only). This limitation arose from the fact that high density experimental emitter maps were only available for these two models. Although the general conclusions of the effects that hot spots produced on dose-volume histograms are valid for all plaque sizes, it would have been desirable to study plaques with asymmetric geometries such as those with notches.

6.2 Implications for the clinical practice

The results obtained in this thesis may influence the clinical practice at different levels. Nowadays, treatments rely on the calibration certificate supplied for the plaques which gives information about the relative depth dose along the symmetry axis and an scarce activity map of 33

points measured at 1.0 mm from the surface of the plaque. The results shown in chapter 3, which consider the heterogeneity of the plaques in their whole surface, suggest the necessity of an accurate emitter map provided by the manufacturer for each plaque, for conducting a more accurate treatment planning.

Chapters 4 and 5 study the effect of rotations of the plaque around its symmetry axis. Understandably, the surgeon suturing the plaque has a number of limitations imposed by the anatomy of the eye in relation to the amount of possible rotations that can be considered. Nevertheless, should an accurate emitter map be available to the ophthalmologist it could be possible to consider in some cases at least two orientations.

The feasibility of eccentric treatments is presented in chapter 5. The results obtained therein indicate that under certain circumstances eccentric treatments are not only feasible but also adequate. Thus, the general practice of trying to avoid this type of treatments could be modified provided an accurate knowledge of the emitter map.

It is important to notice the usefulness of dose-volume histograms for the evaluation of treatments as it has been shown throughout this dissertation. This dose metric is not always used by ocular ophthalmologists who try to maintain to a minimum the imaging dose delivered to the patient. However, it might be the case that the advantages of obtaining a computerized scan of the patient outnumber the negative aspects of the imaging irradiation. The availability of a computerized scan increases the accuracy of the computation of the absorbed dose distribution outside the target volume, with emphasis on the structures at risk. European and many national laws currently require the appropriate dose computation delivered to non-target volumes (see for example article 56.1 from Council of the European Union (2013)).

It is clear that a dose computation in which a detailed emitter map of the plaque is employed, together with a Monte Carlo simulation of the radiation transport in a computerized tomography of the patient, in which the actual heterogeneous mass density is considered, will yield a more accurate distribution than that obtained with the currently available tools.

To conclude, the techniques developed in this thesis follow the recommendations of AAPM (The American Association of Physicists in Medicine) contained in the TG-221 report (Task Group 221) that supports the estimation of heterogeneous dose distributions (Thomson et al., 2019). The report endorses the use of CT imaging for the definition of the target volumes, along with the use of dose-volume histograms as a volumetric tool to determine the absorbed dose in all volumes.

6.3 Future research

In the doctoral dissertation of Dr. rer. medic. M. Hermida-López it was suggested that future research in the field of ruthenium plaques should be addressed to encompass the heterogeneities of the plaques and the anatomy of the eye. Moreover, the TG-221 report explicitly states "In addition, few publications explore the role of plaque and/or tissue heterogeneities for ^{106}Ru sources, which limit the reporting of heterogeneity-corrected doses as required by

the TG-129 report for photon sources." The present doctoral dissertation fulfills the suggestions given by the TG-221 report and Hermida-López's work. The current natural next step after this thesis is to produce a Monte Carlo treatment planning system for eye plaques which would incorporate the techniques developed herein. This step is in accordance with the recommendations of the TG-221 report, that highlights the necessity of a treatment planning system with these characteristics.

Proton irradiation is also a possible therapy for certain ocular malignancies. An accurate knowledge of the dose distribution obtained either with ruthenium plaques or with protons would certainly help clinicians to decide between these two therapies.

Chapter 7

Conclusions

The research presented in this thesis improves the knowledge on the absorbed dose distributions produced by $^{106}Ru/^{106}Rh$ eye plaques in water and in an anthropomorphic phantom. The study also improves the knowledge in the treatment of uveal melanomas by applying the absorbed doses in the aforementioned anthropomorphic phantom. The conclusions are related to the objectives stated in chapter 1 and they are presented in the corresponding order:

1. The main steering program penEasy was modified in two ways. The first modification allows to use spherical sources such as the spherical caps that represent the ruthenium eye plaques. A second modification allows PENELOPE to simulate beta decay spectra. Absorbed dose distributions in water were simulated. For the CCA and CCB plaques, a comparison of the absorbed depth doses against experimental data published and those given by the manufacturer in the plaque certificate were done. Simulated results correctly reproduce the experimental data provided by the manufacturer and to a good extent the experimental data published by other researchers. With the experimental data of other researchers arose the fact that generic homogeneous plaques were compared with experimental data from specific models, thus, indicating the necessity of simulating the specific emitter distribution of a given plaque in order to obtain accurate results.

2. A new modification on the penEasy program was added to allow the use of normalized heterogeneous emitter maps of the CCA1364 and CCB1256 eye plaques. Absorbed dose distributions in a water phantom for these actual plaques were simulated. A comparison was made between absorbed depth doses along the symmetry axis and lateral profiles at different depths for the generic and actual eye plaques. A comparison was also made between the absorbed depth doses corresponding to the heterogeneous plaques and the published experimental data and those given by the manufacturer. Absorbed depth doses corresponding to the simulations of actual plaques fit much better the data provided by the manufacturer than the simulations corresponding to the homogeneous plaques. The results confirmed that knowing the emission map of an ophthalmic plaque is needed to perform accurate simulations on absorbed depth doses and lateral profiles of actual eye plaques.

3. The distinctive feature of penEasy of allowing the simulation of quadric surfaces inserted in a voxelized geometry was used to model geometries formed by a computerized axial tomography scan and an ocular plaque, which was defined as a spherical shell using quadrics, embedded into the voxelized geometry. Volumes corresponding to structures of the eye were segmented to determine the absorbed dose in them. Simulations of the CCA and CCA1364 plaques were computed in three placements named anterior, equatorial and posterior. The CCB and CCB1356 plaques were only simulated in the equatorial placement. The CCB1256, which presents a well defined hot spot, was also simulated considering three rotations with respect to the location of the hot spot named *proximal*, *distal* and *original*. For all plaques, results show that lack of knowledge on the activity map of the radioactive substance results in an overdosage of all the volumes analyzed. In addition, for eye plaques with defined hot spots, such as the CCB1256 plaque, differences in the location of the hot spot with respect to the volume analyzed results in a noticeable variations of the absorbed dose in all segmented volumes.

4. The target volumes corresponding to modeled tumors of different apical heights and the same basal diameter were segmented. Tumors of 3.0 mm of apical height were placed in anterior and posterior locations while for tumors of 3.0, 5.0, 6.5, 7.0 and 7.5 mm only the equatorial location was considered. For the CCA and CCA1364 eye plaques, centered and eccentric treatments were simulated for anterior and posterior tumors while for equatorial tumors only a centered treatment was simulated. For CCB and CCB1256 plaques, which were only positioned equatorially, centered treatments for equatorial tumors were simulated. For these plaque models, eccentric treatments for anterior and posterior tumors were simulated, too. For all treatments, the results showed that considering a homogeneous approximation of the emitter distribution of the plaques results in a longer exposure time and an overdosage in all segmented volumes, tumoral and structures at risk. Consequently, knowing the activity map of the emitter substance increases the accuracy on the dose delivered to target volumes. In addition, tumors up to 5.0 mm could be treated using the small CCA plaque while reducing the absorbed dose in the structures at risk. It is also observed that the knowledge of heterogeneities in the emitter map allows a suitable eccentric treatment of tumors while minimizing the absorbed dose in the structures at risk as recommended by the European and national laws (Council of the European Union, 2013).

Chapter 8

Abstract

Uveal melanoma and retinoblastoma are rare malignant tumors that, if not properly treated, can be life-threatening. Brachytherapy with ^{106}Ru eye plaques is an effective treatment in preserving the ocular globe and maintaining visual acuity to some extent. Although these plaques have been used for decades, there is a lack of precise knowledge about the absorbed dose distribution in the tumor volume and the surrounding structures at risk, introducing large variability in the clinical outcome as it is reflected in the retrospective published studies. The aim of this thesis is to improve, using the general-purpose Monte Carlo radiation transport code PENELOPE, the current knowledge on the dose distribution inside the eye produced by two actual ^{106}Ru plaques taking into account the distribution of the radioactive substance in their emitting surface.

As a preliminary step, the absorbed dose in water produced by two generic CCA and CCB eye plaque models, which consider the emitter substance homogeneously distributed, is simulated. Computed depth doses along the symmetry axis of the plaques are compared with experimental data provided by the manufacturer of the plaques and previously published results. Later, using a measured emitter map of the actual CCA1364 and CCB1256 plaques, simulated depth doses are compared with experimental data and also with the homogeneous approximation. Comparison between lateral profiles and isodose lines are also computed for both plaques. Results show that the actual heterogeneous distribution reproduces better the data provided in the certificate of the plaques.

Dose distributions inside an eye are simulated using an anthropomorphic phantom. The main structures of the eye are segmented to determine the absorbed dose in them. The CCA eye plaque is simulated in an anterior, equatorial and posterior placement while the CCB, due to its larger size, is only simulated in an equatorial placement. To analyze the effect of the heterogeneities on the absorbed dose, rotations around the symmetry axis of the plaques are also simulated. Results indicate that not considering the distribution of the emitter substance produces an overdosage in all segmented volumes as occurs with the cornea when is irradiated anteriorly which receives 71% higher dose with respect to the homogeneous assumption.

Finally, tumor volumes are also segmented and the absorbed dose in them analyzed for different plaque placements and rotations. Eccentric placements of the plaques are also considered. Results show that knowledge of the emitter map allows eccentric treatments and confirms an overdosage when considering the homogeneous assumption.

Bibliography

[1] Agostinelli, S., Allison, J., et al. (2003): Geant4 — a simulation toolkit. Nucl. Instrum. Meth. A 506, 250–303.

[2] Allison, J., Amako, K., Apostolakis, J., Araujo, H., Arce Dubois, P., Asai, M., Barrand, G., Capra, R., Chauvie, S., Chytracek, R., Cirrone, G., Cooperman, G., and Cosmo, G. (2006): Geant4 developments and applications. IEEE Trans. Nucl. Sci. 53, 270–278.

[3] Almansa, J., Salvat-Pujol, F., Díaz-Londoño, G., Carnicer, A., Lallena, A. M., and Salvat, F. (2016): PENGEOM - A general-purpose geometry package for Monte Carlo simulation of radiation transport in material systems defined by quadric surfaces. Comput. Phys. Commun. 199, 102–113.

[4] Astrahan, M. A. (2003): A patch source model for treatment planning of ruthenium ophthalmic applicators. Med. Phys. 30, 1219–1228.

[5] Atchison, D. A., Jones, C. E., Schmid, K. L., Pritchard, N., Pope, J. M., Strugnell, W. E., and Riley, R. A. (2004): Eye shape in emmetropia and myopia. Investig. Ophthalmol. Vis. Sci. 45, 3380–3386.

[6] Baró, J., Sempau, J., Fernández-Varea, J. M., and Salvat, F. (1995): PENELOPE: An algorithm for Monte Carlo simulation of the penetration and energy loss of electrons and positrons in matter. Nucl. Instrum. Meth. B 100, 31–46.

[7] Berger, J. M. (1963): Monte Carlo calculation of the penetration and diffusion of fast charged particles. In: Alder, B., Fernbach, S., and Rotemberg, M., eds, Methods in Computational Physics, Vol.1, 133–215. New York, USA: Academic Press.

[8] Bielajew, A. F. and Rogers, D. W. (1988): Variance-reduction techniques. In: Monte Carlo Transport of Electrons and Photons, 407–419. Boston, USA: Springer.

[9] Brady, L. W. and Hernández, J. C. (1992): Brachytherapy of choroidal melanomas. Strahlenther. Onkol. 168, 61–65.

[10] Brewington, B. Y., Shao, Y. F., Davidorf, F. H., and Cebulla, C. M. (2018): Brachytherapy for patients with uveal melanoma: Historical perspectives and future treatment directions. Clinic. Ophthal. 12, 925–934.

[11] Brualla, L., Palanco-Zamora, R., Wittig, A., Sempau, J., and Sauerwein, W. (2009): Comparison between PENELOPE and electron Monte Carlo simulations of electron fields used in the treatment of conjunctival lymphoma. Phys. Med. Biol. 54, 5469–5481.

[12] Brualla, L., Sempau, J., and Sauerwein, W. (2012): Comment on Monte Carlo calculation of the dose distributions of two ^{106}Ru eye applicators [Radiother Oncol 49 (1998) 191-196]. Radiother. Oncol. 104, 267–268.

[13] Brualla, L., Sempau, J., Zaragoza, F. J., Wittig, A., and Sauerwein, W. (2013): Accurate estimation of dose distributions inside an eye irradiated with ^{106}Ru plaques. Strahlenther. Onkol. 189, 68–73.

[14] Brualla, L., Zaragoza, F., and Sauerwein, W. (2014): Monte Carlo Simulation of the Treatment of Eye Tumors with ^{106}Ru Plaques: A Study on Maximum Tumor Height and Eccentric Placement. Ocul. Oncol. Pathol. 1, 1–11.

[15] Brualla, L., Zaragoza, F. J., Sempau, J., Wittig, A., and Sauerwein, W. (2012): Electron irradiation of conjunctival lymphoma–Monte Carlo simulation of the minute dose distribution and technique optimization. Int. J. Radiat. Oncol. Biol. Phys. 83, 1330–1337.

[16] Chan, M. F., Fung, A. Y., Hu, Y.-C., Chui, C.-S., Amols, H., Zaider, M., and Abramson, D. (2001): The measurement of three dimensional dose distribution of a ruthenium-106 ophthalmological applicator using magnetic resonance imaging of BANG polymer gels 1. Clin. Med. Phys. 2, 85–89.

[17] Chetty, I. J., Curran, B., Cygler, J. E., DeMarco, J. J., Ezzell, G., Faddegon, B. A., Kawrakow, I., Keall, P. J., Liu, H., Charlie Ma, C. M., Rogers, D. W. O., Seuntjens, J., Sheikh-Bagheri, D., and Siebers, J. V. (2007): Report of the AAPM Task Group No. 105: Issues associated with clinical implementation of Monte Carlo-based photon and electron external beam treatment planning. Med. Phys. 34, 4818–4853.

[18] Council of the European Union (2013): Council Directive 2013/59/Euratom. Official Journal of the European Union 57, 1–216.

[19] Cross, W. G., Hokkanen, J., Järvinen, H., Mourtada, F., Sipilä, P., Soares, C. G., and Vynckier, S. (2001): Calculation of beta-ray dose distributions from ophthalmic applicators and comparison with measurements in a model eye. Med. Phys. 28, 1385–1396.

[20] Damato, B. (2001): Detection of uveal melanoma by optometrists in the United Kingdom. Ophthal. Physiol. Op. 21, 268–271.

[21] Damato, B., Patel, I., Campbell, I. R., Mayles, H. M., and Errington, R. D. (2005): Local tumor control after ^{106}Ru brachytherapy of choroidal melanoma. Int. J. Radiat. Oncol. Biol. Phys. 63, 385–391.

[22] Damato, B., Patel, I., Campbell, I. R., Mayles, H. M., and Errington, R. D. (2005): Visual acuity after Ruthenium-106 brachytherapy of choroidal melanomas. Int. J. Radiat. Oncol. Biol. Phys. 63, 392–400.

[23] Das, I. J., Ding, G. X., and Ahnesjö, A. (2007): Small fields: Nonequilibrium radiation dosimetry. Med. Phys. 35, 206–215.

[24] Davelaar, J., Schaling, D. F., Hennen, L. A., and Broerse, J. J. (1992): Dosimetry of ruthenium-106 eye applicators. Med. Phys. 19, 691–694.

[25] Davidorf, F. H. (1970): Conservative Management of Malignant Melanoma. Arch. Ophthalmol. 83, 21–26.

[26] De Frenne, D. and Negret, A. (2008): Nuclear Data Sheets for A = 106. Nucl. Data Sheets. 109, 943–1102.

[27] Eckert & Ziegler BEBIG, G., Berlin (2011): User Manual Ru-106 Ophthalmic Applicators, Rev 9, English. Eckert & Ziegler BEBIG, Berlin, Germany.

[28] Eichmann, M., Flühs, D., and Spaan, B. (2009): Development of a high precision dosimetry system for the measurement of surface dose rate distribution for eye applicators. Med. Phys. 36, 4634–4643.

[29] Eichmann, M., Krause, T., Flühs, D., and Spaan, B. (2012): Development of a high-precision xyz-measuring table for the determination of the 3D dose rate distributions of brachytherapy sources. Phys. Med. Biol. 57, N421.

[30] Fernández-Varea, J. M., Carrasco, P., Panettieri, V., and Brualla, L. (2007): Monte Carlo based water/medium stopping-power ratios for various ICRP and ICRU tissues. Phys. Med. Biol. 52, 6475–6483.

[31] Fernández-Varea, J. M., Mayol, R., Baró, J., and Salvat, F. (1993): On the theory and simulation of multiple elastic scattering of electrons. Nucl. Instrum. Meth. B 73, 447–473.

[32] Ferrari, A., Sala, P., Fasso, A., and Ranft, J. (2005): FLUKA: A Multi-Particle Transport Code (Program version 2005). Technical Report October, Stanford Linear Accelerator Center (SLAC).

[33] Flühs, D., Bambynek, M., Heintz, M., Indenkämpen, F., Kolanoski, H., Wegener, D., Sauerwein, W., and Quast, U. (1997): Dosimetry and Design of Radioactive Eye Plaques. In: Radiotherapy of Ocular Diseases, volume 30, 26–38. Karger Publishers.

[34] Flühs, D., Flühs, A., Ebenau, M., and Eichmann, M. (2016): Polyethylene naphthalate scintillator: A novel detector for the dosimetry of radioactive ophthalmic applicators. Ocul. Oncol. Pathol. 2, 5–12.

[35] Fuss, M. C., Muñoz, A., Oller, J. C., Blanco, F., Williart, A., Limão-Vieira, P., Borge, M. J. G., Tengblad, O., Huerga, C., Téllez, M., and García, G. (2011): Energy deposition by a ^{106}Ru/^{106}Rh eye applicator simulated using LEPTS, a low-energy particle track simulation. Appl. Radiat. Isot. 69, 1198–1204.

[36] Galloway, N. R., Amoaku, W. M., Galloway, P. H., and Browning, A. C. (2006): Basic Anatomy and Physiology of the EyeCommon eye diseases and their management. In: Common eye diseases and their management Springer; S.7–15. London. Springer.

[37] García-Toraño, E. and Grau, A. (1985): EFFY, a new program to compute the couting efficiency of beta particles in liquid scintillators. Comput. Phys. Commun. 36, 307–312.

[38] Goitein, M. and Miller, T. (1983): Planning proton therapy of the eye. Med. Phys. 3, 275–283.

[39] Goudsmit, S. and Saunderson, J. L. (1940): Multiple scattering of electrons. II. Phys. Rev. 58, 36–42.

[40] Hansen, J. B., Culberson, W. S., and DeWerd, L. A. (2019): A convex windowless extrapolation chamber to measure surface dose rate from ^{106}Ru/^{106}Rh episcleral plaques. Med. Phys. 46, 2430–2443.

[41] Hawkins, B. S. (2011): Collaborative Ocular Melanoma Study randomized trial of ^{125}I brachytherapy. Clin. Trials 8, 661–673.

[42] Hayward, E. and Hubbell, J. (1954): The albedo of various materials for 1-MeV photons. Phys. Rev. 93, 955–956.

[43] Hermida-López, M. (2013): Calculation of dose distributions for 12 ^{106}Ru/^{106}Rh ophthalmic applicator models with the PENELOPE Monte Carlo code. Med. Phys. 40, 101705–1–13.

[44] Hermida-López, M. and Brualla, L. (2017): Technical Note: Monte Carlo study of ^{106}Ru/^{106}Rh ophthalmic plaques including the ^{106}Rh gamma spectrum. Med. Phys. 44, 2581–2585.

[45] Hermida-López, M. and Brualla, L. (2018): Absorbed dose distributions from ophthalmic ^{106}Ru/^{106}Rh plaques measured in water with radiochromic film. Med. Phys. 45 1699–1707.

[46] Hokkanen, J., Heikkonen, J., and Holmberg, P. (1997): Theoretical calculations of dose distributions for beta-ray eye applicators. Med. Phys. 24, 211–213.

[47] ICRU (1984): Stopping Powers for Electrons and Positrons (ICRU Report 37). Whasington D.C: ICRU.

[48] ICRU (2004): Dosimetry of Beta Rays and Low-Energy Photons for Brachytherapy With Sealed Sources (ICRU Report 72). ICRU 4.

[49] ICRU (2016): Key data for ionizing-radiation dosimetry: measurements standards and applications (ICRU Report 90). ICRU 14.

[50] Jager, M. J., Desjardins, L., Kivelä, T., and Damato, B. (2011): Current concepts in uveal melanoma, volume 49. Karger.

[51] Kalos, M. H. and Whitlock, P. A. (2009): Monte Carlo Methods. 2n edition. Jonh Wiley & Sons.

[52] Kaulich, T. W., Zurheide, J., Haug, T., Budach, W., Nüsslin, F., and Bamberg, M. (2004): On the actual state of industrial quality assurance procedures with regard to ^{106}Ru ophthalmic plaques. Strahlenther. Onkol. 180, 358–364.

[53] Kaulich, T. W., Zurheide, J., Haug, T., Nüsslin, F., and Bamberg, M. (2005): Clinical quality assurance for Ru ophthalmic applicators. Radiother. Oncol. 76, 86–92.

[54] Kawrakow, I. and Rogers, D. W. O. (2003): The EGSnrc Code System : Monte Carlo Simulation of Electron and Photon Transport. Report Pirs-701 (National Research Council of Canada, Ottawa) 2001–2003.

[55] Kirov, A. S., Piao, J. Z., Mathur, N. K., Miller, T. R., Devic, S., Trichter, S., Zaider, M., Soares, C. G., and LoSasso, T. (2005): The three-dimensional scintillation dosimetry method: Test for a ^{106}Ru eye plaque applicator. Phys. Med. Biol. 50, 3063–3081.

[56] Kovačević, N., Vrtar, M., and Vekić, B. (2005): A simple calibration method for ^{106}Ru/^{106}Rh eye applicators. Radiother. Oncol. 74, 293–299.

[57] Krause, F., Möller, M., Risske, F., and Siebert, F.-A. (2019): Dosimetry of ruthenium-106 ophthalmic applicators with thin layer thermoluminescence dosimeters–Clinical quality control. Z. Med. Phys. 49, 1–6.

[58] Landau, L. (1944): On the energy loss of fast particles by ionization. J. Phys. 8, 201–205.

[59] Lax, I. (1991): Dosimetry of ^{106}Ru eye applicators with a p-type silicon detector. Phys. Med. Biol. 36, 963–973.

[60] Lewis, H. W. (1950): Multiple scattering in an infinite medium. Phys. Rev. 78, 526.

[61] Loevinger, R. (1950): Distribution of absorbed energy around a point source of β radiation. Science 112, 530–531.

[62] Lommatzsch, P. K. (1977): Treatment of choroidal melanomas with ^{106}Ru/^{106}Rh beta-ray applicators. Transactions of the ophthalmological societies of the United Kingdom 97, 428–429.

[63] Lommatzsch, P. K. (1986): Results after β-irradiation (^{106}Ru/^{106}Rh) of choroidal melanomas: 20 years' experience. Br. J. Ophthalmol. 70, 844–851.

[64] Lommatzsch, P. K. and Vollmar, R. (1966): Ein neuer Weg zur konservativen Therapie intraokularer Tumoren mit Betastrahlen (^{106}Ru/^{106}Rh) unter Erhaltung der Sehfähigkeit. Klin Monatsbl Augenheilkd 148, 682–699.

[65] Mossböck, G., Rauscher, T., Winkler, P., Kapp, K. S., and Langmann, G. (2007): Impact of dose rate on clinical course in uveal melanoma after brachytherapy with ruthenium-106. Strahlenther. Onkol. 183, 571–575.

[66] Mourtada, F., Koch, N., and Newhauser, W. (2005): ^{106}Ru/^{106}Rh Plaque and proton radiotherapy for ocular melanoma: A comparative dosimetric study. Radiat. Prot. Dosim. 116, 454–460.

[67] Nag, S., Quivey, J. M., Earle, J. D., Followill, D., Fontanesi, J., and Finger, P. T. (2003): The American Brachytherapy Society recommendations for brachytherapy of uveal melanomas. Int. J. Radiat. Oncol. Biol. Phys. 56, 544–555.

[68] Naseripour, M., Jaberi, R., Sedaghat, A., Azma, Z., Nojomi, M., Falavarjani, K. G., and Nazari, H. (2016): Ruthenium-106 brachytherapy for thick uveal melanoma: Reappraisal of apex and base dose radiation and dose rate. J. Contemp. Brachytherapy 8, 66–73.

[69] Nathan, P., Cohen, V., Coupland, S., Curtis, K., Damato, B., Evans, J., Fenwick, S., Kirkpatrick, L., Li, O., Marshall, E., McGuirk, K., Ottensmeier, C., Pearce, N., Salvi, S., Stedman, B., Szlosarek, P., and Turnbull, N. (2015): Uveal Melanoma UK National Guidelines. European Journal of Cancer 51, 2404–2412.

[70] Olch, A. J. (2013): Pediatric Radiotherapy. Planning and treatment. Boca Raton, London, New York: CRC Press.

[71] Pe'er, J. (2012): Ruthenium-106 brachytherapy. In: Current Concepts in Uveal Melanoma, volume 49, 27–40. Karger Publishers.

[72] Reynaert, N., Van der Marck, S. C., Schaart, D. R., Van der Zee, W., Van Vliet-Vroegindeweij, C., Tomsej, M., Jansen, J., Heijmen, B., Coghe, M., and De Wagter, C. (2007): Monte Carlo treatment planning for photon and electron beams. Radiat. Phys. Chem. 76, 643–686.

[73] Rubinstein, R. Y. and Kroese, D. P. (2016): Simulation and the Monte Carlo Method. 2nd edition. New York: Jonh Wiley & Sons.

[74] Salvat, F. (2019): PENELOPE-2018: A code system for Monte Carlo simulation of electron and photon transport. OECD/NEA Data Bank, Issy-les-Moileneaux, France.

[75] Salvat, F. and Fernández-Varea, J., . J. M. Sempau (2009): PENELOPE-2008: A code system for Monte Carlo simulation of electron and photon transport. OECD/NEA Data Bank, Issy-les-Moileneaux, France.

[76] Sánchez-Reyes, A., Tello, J. J., Guix, B., and Salvat, F. (1998): Monte Carlo calculation of the dose distributions of two ^{106}Ru eye applicators. Radiother. Oncol. 49, 191–6.

[77] Schueler, A. O., Flühs, D., Anastassiou, G., Jurklies, C., Neuhäuser, M., Schilling, H., Bornfeld, N., and Sauerwein, W. (2006): Beta-ray brachytherapy with ^{106}Ru plaques for retinoblastoma. Int. J. Radiat. Oncol. Biol. Phys.. 65, 1212–1221.

[78] Sempau, J. (1996): Development and applications of a computer code for Monte Carlo simulation of electron-photon showers. Universitat Politècnica de Catalunya.

[79] Sempau, J., Acosta, E., and Baro, J. (1997): An algorithm for Monte Carlo simulation of coupled electron-photon transport. Nucl. Instrum. Meth. B 132, 377–390.

[80] Sempau, J., Badal, A., and Brualla, L. (2011): A PENELOPE-based system for the automated Monte Carlo simulation of clinacs and voxelized geometries–application to far-from-axis fields. Med. Phys. 38, 5887–5895.

[81] Shields, C. L., Shields, J. A., Cater, J., Othmane, I., Singh, A. D., and Micaily, B. (2001): Plaque radiotherapy for retinoblastoma: Long-term tumor control and treatment complications in 208 tumors. Ophthalmol. 108, 2116–2121.

[82]Simpson, E., Gallie, B., Laperrierre, N., Beiki-Ardakani, A., Kivelä, T., Raivio, V., Heikkonen, J., Desjardins, L., Dendale, R., Mazal, A., Bornfeld, N., Sauerwein, W., Flüehs, D., Brualla, L., Honavar, S., Reddy, V., Suzuki, S., Murakami, N., Saakyan, S., Valskiy, V., Amiryan, A., Seregard, S., All-Eriksson, C., Hjelmqvist, L., Lundell, G., Sinclair, G., Lundell, M., Damato, B., Errington, R., Mayles, P., Mayles, H., Bergstrom, C., Grossniklaus, H., Crocker, I., Butker, E., Wilson, M., Haik, B., Geischen, H., Patra, P., Duker, J., Mignano, J., Rivard, M., Finger, P., Semenova, E., Choi, W., and Kalach, N. (2014): The American Brachytherapy Society consensus guidelines for plaque brachytherapy of uveal melanoma and retinoblastoma. Brachyther. 13, 1–14.

[83] Singh, A. D., Turell, M. E., and Topham, A. K. (2011): Uveal melanoma: Trends in incidence, treatment, and survival. Ophthalmol 118, 1881–1885.

[84] Soares, C. G., Vynckier, S., Järvinen, H., Cross, W. G., Sipilä, P., Flühs, D., Schaeken, B., Mourtada, F. A., Bass, G. A., and Williams, T. T. (2001): Dosimetry of beta-ray ophthalmic applicators: Comparison of different measurement methods. Med. Phys. 28, 1373–1384.

[85] Stallard, H. B., Cserr, F., and Island, R. (1966): Radiotherapy for malignant melanoma fo the choroid. Br. J. Ophthalmol. 50, 147–156.

[86] Stöckel, E., Eichmann, M., Flühs, D., Sommer, H., Biewald, E., Bornfeld, N., Spaan, B., and Sauerwein, W. (2018): Dose Distributions and Treatment Margins in Ocular Brachytherapy with ^{106}Ru Eye Plaques. Ocul. Oncol. Pathol. 4, 122–128.

[87] Taccini, G., Cavagnetto, F., Coscia, G., Garelli, S., and Pilot, A. (1997): The determination of dose characteristics of ruthenium ophthalmic applicators using radiochromic film. Med. Phys. 24, 2034–2037.

[88] Takiar, V., Voong, K. R., Gombos, D. S., Mourtada, F., Rechner, L. A., Lawyer, A. A., Morrison, W. H., Garden, A. S., and Beadle, B. M. (2014): A choice of radionuclide: Comparative outcomes and toxicity of ruthenium-106 and iodine-125 in the definitive treatment of uveal melanoma. Pract. Radiat. Oncol. 5, e169–e176.

[89] Taylor, J. M. (1989): Use of sources for brachytherapy. Fed. Regist. 54, 41819–41821.

[90] Thomson, R. M., Furutani, K. M., Kaulich, T. W., Mourtada, F., Rivard, M. J., Soares, C. G., Vanneste, F. M., and Melhus, C. S. (2019): AAPM recommendations on medical physics practices for ocular plaque brachytherapy: Report of Task Group 221. Med. Phys.

[91] Trichter, S., Soares, C. G., Zaider, M., DeWyngaert, J. K., DeWerd, L. A., and Kleiman, N. J. (2018): 15 years of ^{106}Ru eye plaque dosimetry at Memorial Sloan-Kettering Cancer Center and Weill Cornell Medical Center using radiochromic film in a Solid Water phantom. Biomed. Phys. Eng. Express 4, 45017.

[92] Valentin, J. and Streffer, C. (2002): Basic anatomical and physiological data for use in radiological protection: Reference values - ICRP Publication 89. Annals of the ICRP 32, 1–277.

[93] Verschueren, K. M., Creutzberg, C. L., Schalij-Delfos, N. E., Ketelaars, M., Klijsen, F. L., Haeseker, B. I., Ligtenberg, S. M., Keunen, J. E., and Marijnen, C. A. (2010): Long-term outcomes of eye-conserving treatment with Ruthenium^{106} brachytherapy for choroidal melanoma. Radiother. and Oncol. 95, 332–338.

[94] Virgili, G., Gatta, G., Ciccolallo, L., Capocaccia, R., Biggeri, A., Crocetti, E., Lutz, J. M., and Paci, E. (2007): Incidence of Uveal Melanoma in Europe. Ophthalmol. 114, 2309–2315.

[95] Vynckier, S. and Wambersie, A. (1982): Dosimetry of beta sources in radiotherapy. I. The beta point source dose function. Phys. Med. Biol. 27, 1339–1347.

[96] X-5 Monte Carlo Team, X. (2005): MCNP– A General Monte Carlo N-Particle Transport Code, Version 5, LA-UR-03-1987. Los Alamos Nuclear Laboratory.

[97] Zaragoza, F. J., Eichmann, M., Flühs, D., Sauerwein, W., and Brualla, L. (2017): Monte Carlo Estimation of Absorbed Dose Distributions Obtained from Heterogeneous ^{106}Ru Eye Plaques. Ocul. Oncol. Pathol. 3, 204–209.

[98] Zaragoza, F. J., Eichmann, M., Flühs, D., Timmermann, B., and Brualla, L. (2020): Monte Carlo computation of dose-volume histograms in the structures at risk of an eye irradiated with heterogeneous ^{106}Ru plaques. In press. Ocul. Oncol. Pathol.

[99] Zaragoza, F. J., Eichmann, M., Flühs, D., Wittig, A., Sauerwein, W., and Brualla, L. (2018): Monte Carlo Simulation of the Treatment of Uveal Melanoma Using Measured Heterogeneous ^{106}Ru Plaques. Ocul. Oncol. Pathol. 5, 276–283.

[100] Zheng-Ming, L. and Brahme, A. (1993): An overview of the transport theory of charged particles. Radiat. Phys. Chem. 41, 673–703.

Abbreviations

AAPM The American Association of Physicists in Medicine

ASCII American Standard Code for Information Interchange

ASMW Amt für Standardisierung, Messwesen und Warenprüfung

BANG Bis, Acrylamide, Nitrogen and aqueous Gelatine

CCA Name of an eye plaque model from Eckert & Ziegler BEBIG GmbH

CCB Name of an eye plaque model from Eckert & Ziegler BEBIG GmbH

COMS Collaborative Ocular Melanoma Study

CT Computerized tomography scan

DICOM Digital Imaging and Communications in Medicine

DVH Dose Volume Histogram

EGS Electron Gamma Shower

FLUKA FLUktuierende KAskade

GEANT GEometry ANd Tracking

IAEA International Atomic Energy Agency

ICRU International Commission on Radiation Units and Measurements

MCNP Monte Carlo N-Particle Transport

NEA Nuclear Energy Agency

NIST National Institute of Standards and Technology

OECD Organisation for Economic Co-operation and Development

PENELOPE Penetration and ENErgy LOss of Positrons and Electrons

List of Figures

List of Tables

Acknowledgements

First of all, I would like to express my deep gratitude to my supervisor, Priv.-Doz. Dr. Lorenzo Brualla, for his expertise, support, infinite patience and specially for believing in me all along the way. His support has been essential in providing guidance and feedback for completing this work. ¡Gracias, Lorenzo!

I am thankful also to the following persons:

Priv.-Doz. Dr. Theodor W. Kaulich (Department of Medical Physics, University of Tübingen, Germany), for providing me with the experimental data corresponding to the CCA applicator.

Prof. Gianni Taccini (Department of Medical Physics, S. Martino Hospital, Genoa, Italy), for sending his experimental data corresponding to the CCB applicator.

Dr. rer. nat. Marion Eichmann (Fakultät Physik, Technische Universität Dortmund, Germany), for giving me the experimental emitter distributions of the actual eye plaques used in this thesis.

Dr. Josep Sempau, (Universitat Politécnica de Catalunya, Barcelona, Spain), for his valuable advices on Monte Carlo simulation of radiation transport.

Prof. Dr. med. Wolfgang Sauerwein (Strahlenklinik, Universitätsklinikum Essen) for all his support and advice in medical matters.

Dr. rer. medic. Marcelino Hermida-López (Hospital Universitario Vall d'Hebrón, Barcelona, Spain), for his valuable suggestions and revising the manuscript, as well as for providing me with the dissertation format he programmed in LaTeX.

Dr. Dirk Flühs (Strahlenklinik, Universitätsklinikum Essen) for the many corrections and suggestions during the papers we have written together.

Dr. Miguel Rodríguez, for many useful discussions on the intricacies of Monte Carlo simulation of radiation transport and its applications.

Mr. Josep Pujal system administrator of the Argos cluster at the Universitat Politécnica de Catalunya for his help in running the simulations performed.

I am also grateful to the following institutions for supporting my research: European Commission through the MAESTRO project (IP CE503564), Deutsche Forschungsgemeinschaft projects BR 4043/1-1, BR 4043/3-1, FL 733/1-1 and EI 869/1-3, Spanish Ministerio de Economía y Competitividad (Project no. FIS2012-38480), Spanish Ministerio de Ciencia e Innovación (project no. FPA2009-14091-C02-01), and the HARMONIC project (Health effects of cArdiac fluoRoscopy and MOderN radIotherapy in paediatriCs) which has received funding from the Euratom research and training programme 2014-2018 under grant agreement No 847707.

To my wife Charo and my daughters Katia and Nina, for their unconditional support and encouragement, even when the days were sunny and we spent them at home. *Daddy, when are you going to finish the book?—Oh my God, listen to your daughters!*

To my parents, for always being there.

The curriculum vitae is not included in the online version for data protection reasons.